

LOW-FREQUENCY VARIABILITY OF THE LARGE-SCALE OCEAN CIRCULATION: A DYNAMICAL SYSTEMS APPROACH

Henk A. Dijkstra¹

Michael Ghil²

Department of Atmospheric Science

Department of Atmospheric and Oceanic Sciences and

Colorado State University

Institute of Geophysics and Planetary Physics

Fort Collins, U.S.A.

University of California at Los Angeles, Los Angeles

U.S.A.

Revised for Reviews of Geophysics

H. A. Dijkstra¹, Department of Atmospheric Science, Colorado State University, Fort Collins, CO, 80526, USA. (email: dijkstra@atmos.colostate.edu)

M. Ghil², Department of Atmospheric and Oceanic Sciences and Institute of Geophysics and Planetary Physics, University of California at Los Angeles, 405 Hilgard Ave., Los Angeles, CA 90095-1565, USA. (email: ghil@atmos.ucla.edu)

¹Also at: Institute for Marine and Atmospheric research Utrecht, Department of Physics and Astronomy, Utrecht University, Princetonplein 5, 3584 CC Utrecht, The Netherlands.

²Also at: Département Terre-Atmosphère-Océan and Laboratoire de Météorologie Dynamique de CNRS/IPSL, Ecole Normale Supérieure, Paris, France.

Abstract.

Oceanic variability on interannual, interdecadal and longer time scales plays a key role in climate variability and climate change. Paleoclimatic records suggest major changes in the location and rate of deep-water formation in the Atlantic and Southern Ocean on time scales from millennia to millions of years. Instrumental records of increasing duration and spatial coverage document substantial variability in the path and intensity of ocean surface currents on time scales of months to decades. We review recent theoretical and numerical results that help explain the physical processes governing the large-scale ocean circulation and its intrinsic variability. To do so, we apply systematically the methods of dynamical systems theory. The dynamical systems approach is proving successful for more and more detailed and realistic models, up to and including oceanic and coupled ocean-atmosphere general circulation models. In this approach, one follows the road from simple, highly symmetric model solutions, through a “bifurcation tree,” toward the observed, complex behavior of the system under investigation. The observed variability can be shown to have its roots in simple transitions from a circulation with high symmetry in space and regularity in time to circulations with successively lower symmetry in space and less regularity in time. This road of successive bifurcations leads through multiple equilibria to oscillatory and eventually chaotic solutions. Key features of this approach are illustrated in detail for simplified models of two basic problems of the ocean circulation. First, a barotropic model is used to capture major features of the wind-driven ocean circulation and of the changes in its behavior as wind stress increases. Second, a zonally averaged model is used to show how the thermohaline ocean circulation changes as buoyancy fluxes at the surface increase. For the wind-driven circulation, multiple separation patterns of a ‘Gulf-Stream like’ eastward jet are obtained. These multiple equilibria are followed by sub- and interannual oscillations of the jet and of the entire basin’s circulation. The multiple equilibria of the thermohaline circulation include deep-water formation near the equator, near either pole or both, as well as intermediate possibilities that bear some degree of resemblance with the currently observed Atlantic overturning pattern. Some of these multiple equilibria are subject, in turn, to oscillatory instabilities with time scales of decades, centuries and millennia. Interdecadal and centennial oscillations are the ones of greatest interest in the current debate on global warming and on the relative roles of natural and anthropogenic variability in it. They involve the physics of the truly three-dimensional coupling between the wind-driven and thermohaline circulation. To arrive at this three-dimensional picture, the bifurcation tree is sketched out for increasingly complex models for both the wind-driven and the thermohaline circulation.

Table of Contents

1. Introduction and Motivation ···	5
1.1 Climate variability on multiple time scales ···	5
1.2 Role of the ocean circulation ···	9
1.3 The modeling hierarchy ···	11
1.4 A unifying framework ···	12
2. The Wind-Driven Circulation ···	16
2.1 Observations ···	17
2.2 Classical theory and numerical simulations ···	20
2.3 Successive bifurcations in equivalent-barotropic models ···	22
2.3.1 The origin of multiple steady states ···	24
2.3.2 The origin of temporal variability ···	25
2.4 Low- and ultra-low frequency results ···	27
2.5 External asymmetries ···	29
2.5.1 Forcing asymmetries ···	29
2.5.2 Geometric asymmetries ···	31
2.6 Relevance to the North Atlantic circulation ···	32
3. The Thermohaline Circulation ···	36
3.1 Observations ···	36
3.2 Box models and their multiple equilibria ···	41
3.3 Two-dimensional (2-D) models and their relaxation oscillations ···	47
3.4 Three-dimensional (3-D) models ···	52

3.4.1 Multiple equilibria ...	53
3.4.2 Temporal variability ...	56
3.5 Relevance to the North Atlantic and global THC ...	60
4. Outlook ...	63

1. INTRODUCTION AND MOTIVATION

Until a quarter-of-a-century ago [Broecker and Van Donk, 1970; Hays *et al.*, 1976], the climates of the past had been described mostly in qualitative terms. Since then, many techniques have become available to construct climatic records from geological, biological and physical data [Bradley, 1999]. These proxy records show that climate variations on different time scales have been very common in the past. The enormous amount of instrumental data that has been collected over the last century-and-one-half contributes in turn to a more and more complete picture of the climate system's variability.

The purpose of the present review paper is to describe the role of the ocean circulation in this variability and emphasize that dynamical systems theory can contribute substantially in understanding this role. The intended audience and the way prospective readers can best benefit from this review are highlighted in Box 1. To facilitate diverse routes through the paper, we have included in Table 1 a glossary of the principal symbols and in Table 2 a list acronyms.

Box 1**Table 1****Table 2**

1.1. Climate variability on multiple time scales

An “artist’s rendering” of climate variability on all time scales is provided in Fig. 1a. The first version of this figure was produced by Mitchell [1976] and many versions thereof have circulated since. The figure is meant to summarize our knowledge of the spectral power $S = S(\omega)$, i.e. the amount of variability in a given frequency band, between ω and $\omega + \Delta\omega$; here the frequency ω is the inverse of the period of oscillation and $\Delta\omega$ indicates a small increment. This power spectrum is not computed directly by spectral analysis from a time series of a given climatic quantity, such as (local or global) temperature; indeed, there is no single time series that is 10^7 years long and has a sampling interval of

Fig. 1

hours, as the figure would suggest. Figure 1a includes, instead, information obtained by analyzing the spectral content of many different time series, for example, the spectrum (Fig. 1b) of the 335-year long record of Central England temperatures. This time series is the longest instrumentally measured record of any climatic variable. Given the lack of earlier instrumental records, one can easily imagine (but cannot easily confirm) that the higher-frequency spectral features might have changed, in amplitude, frequency or both, over the course of climatic history.

With all due caution in its interpretation, Fig. 1a reflects three types of variability: (i) sharp lines that correspond to periodically forced variations, at one day and one year; (ii) broader peaks that arise from internal modes of variability; and (iii) a continuous portion of the spectrum that reflects stochastically forced variations, as well as deterministic chaos [Ghil and Robertson, 2000; Ghil, 2002].

Between the two sharp lines at 1 day and 1 year lies the synoptic variability of mid-latitude weather systems, concentrated at 3–7 days, as well as intraseasonal variability, i.e. variability that occurs on the time scale of 1–3 months. The latter is also called low-frequency atmospheric variability, a name that refers to the fact that this variability has lower frequency, or longer periods, than the life cycle of weather systems. Intraseasonal variability comprises phenomena such as the Madden–Julian oscillation of winds and cloudiness in the tropics or the alternation between episodes of zonal and blocked flow in mid-latitudes [Ghil and Childress, 1987; Ghil *et al.*, 1991; Haines, 1994; Molteni, 2002].

Immediately to the left of the seasonal cycle in Fig. 1a lies interannual, i.e. year-to-year, variability. An important component of this variability is the El Niño phenomenon in the Tropical Pacific: once about every four years, the sea-surface temperatures (SSTs)

in the Eastern Tropical Pacific increase by a few degrees over a period of about one year. This SST variation is associated with changes in the trade winds over the tropical Pacific and in sea-level pressures [Bjerknes, 1969; Philander, 1990]; an East–West seesaw in the latter is called the Southern Oscillation. The combined El Niño/Southern Oscillation (ENSO) phenomenon arises through large-scale interaction between the equatorial Pacific and the atmosphere above. Equatorial wave dynamics in the ocean plays a key role in setting ENSO’s time scale [Cane and Zebiak, 1985; Neelin *et al.*, 1994, 1998; Dijkstra and Burgers, 2002].

The greatest excitement among scientists as well as the public is currently being generated by interdecadal variability, i.e. climate variability on the time scale of a few decades, the time scale of an individual human’s life cycle [Martinson *et al.*, 1995]. Figure 1b represents an up-to-date “blow-up” of the interannual-to-interdecadal portion of Fig. 1a. The broad peaks are due to the climate system’s internal processes: each spectral component can be associated, at least tentatively, with a mode of interannual or interdecadal variability [Plaut *et al.*, 1995]. Thus the rightmost peak, with a period of 5.5 years, can be attributed to the remote effect of ENSO’s low-frequency mode, while the 7.7-year peak captures a North Atlantic mode of variability that arises from the Gulf Stream’s interannual cycle of meandering and intensification. The two interdecadal peaks, near 14 and 25 years, are also present in global records, instrumental as well as paleoclimatic [Kushnir, 1994; Mann *et al.*, 1998; Moron *et al.*, 1998; Delworth and Mann, 2000; Ghil *et al.*, 2002a].

Finally, the leftmost part of Fig. 1a represents paleoclimatic variability. The information summarized here comes exclusively from proxy indicators of climate [Imbrie and Imbrie, 1986]. These include coral records [Boisieu *et al.*, 1999] and tree rings for the

historic past [Mann *et al.*, 1998], as well as marine-sediment [Duplessy and Shackleton, 1985] and ice-core [Jouzel *et al.*, 1991] records for the last two million years of Earth history, the Quaternary. Glaciation cycles, an alternation of warmer and colder climatic episodes, dominated the Quaternary era. The cyclicity is manifest in the broad peaks present in Fig. 1a between roughly 1 kyr and 1 Myr. The two peaks at about 20 kyr and 40 kyr reflect variations in Earth's orbit, while the dominant peak at 100 kyr remains to be convincingly explained [Imbrie and Imbrie, 1986; Ghil and Childress, 1987; Gildor and Tziperman, 2001]. The glaciation cycles provide a fertile testing ground for theories of climate variability for two reasons: (i) they represent a wide range of climatic conditions; and (ii) they are much better documented than earlier parts of climatic history.

Within these glaciation cycles, there are higher-frequency oscillations prominent in the North Atlantic paleoclimatic records. These are the Heinrich [1988] events, with a near-periodicity of 6–7 kyr, and the Dansgaard-Oeschger cycles that provide the peak at around 1–2.5 kyr in Fig. 1a. Rapid changes in temperature, of up to one half of the amplitude of a typical glacial–interglacial temperature difference, occurred during Heinrich events and somewhat smaller ones over a Dansgaard-Oeschger cycle. Progressive cooling through several of the latter cycles followed by an abrupt warming defines a Bond cycle [Bond *et al.*, 1995]. In North Atlantic sediment cores, the coldest part of each Bond cycle is marked by a so-called Heinrich layer that is rich in ice-rafted debris. None of these higher-frequency oscillations can be directly connected to orbital or other periodic forcings.

In summary, climate variations range from the large-amplitude climate excursions of the past millennia to smaller-amplitude fluctuations on shorter time scales. Several spectral peaks of variability can be clearly related to forcing mechanisms; others cannot. In fact,

even if the external forcing were constant in time — i.e., if no systematic changes in insolation or atmospheric composition, such as trace gas or aerosol concentration, would occur — the climate system would still display variability on many time scales. This statement is clearly true for the 3–7 days synoptic variability of mid-latitude weather, which arises through baroclinic instability of the zonal winds, and the ENSO variability in the equatorial Pacific, as discussed above. Processes internal to the climate system can thus give rise to spectral peaks that are not related directly to the temporal variability of the forcing. It is the interaction of this highly complex intrinsic variability with the relatively small time-dependent variations in the forcing that is recorded in the proxy records and instrumental data.

1.2. Role of the ocean circulation

We focus in this review on the ocean circulation as a source of internal climate variability. The ocean moderates climate through its large thermal inertia, i.e., its capacity to store and release heat, and its poleward heat transport through ocean currents. The exact importance of the latter relative to atmospheric heat transport, though, is still a matter of active debate [Seager *et al.*, 2001]. The large-scale ocean circulation is driven both by momentum fluxes, as well as by fluxes of heat and freshwater at the ocean–atmosphere interface. The near-surface circulation is dominated by horizontal currents that are mainly driven by the wind-stress forcing, while the much slower motions of the deep ocean are mainly induced by buoyancy differences.

The circulation due to either forcing mechanism is often described and analyzed separately for the sake of simplicity. In fact, the wind-driven and thermohaline circulation together form a complex three-dimensional (3-D) flow of different currents and water

masses through the global ocean. The simplest picture of the global ocean circulation has been termed the ‘ocean conveyor’ [Gordon, 1986; Broecker, 1991]; it corresponds to a two-layer view where the vertical structure of the flow field is separated into a shallow flow, above the permanent thermocline at roughly 1000 m, and a deep flow between this thermocline and the bottom (i.e., between a depth of roughly 1000 m and 4000 m); see Fig. 2. The unit of volume flux in the ocean is $1 \text{ Sv} = 10^6 \text{ m}^3\text{s}^{-1}$ and it equals approximately the total flux of the world’s major rivers. MacDonald and Wunsch [1996] and Ganachaud and Wunsch [2000] have provided an updated version of this schematic representation of the ocean circulation.

Fig. 2

In the North Atlantic, for instance, the major current is the Gulf Stream, an eastward jet that arises through the merging of the two western boundary currents, the northward-flowing Florida Current and the southward flowing Labrador Current. In the North Atlantic’s subpolar seas, about 14 Sv of the upper-ocean water carried northward by the North Atlantic Drift, the northeastward extension of the Gulf Stream, is converted to deepwater by cooling and salinification. This North Atlantic Deep Water (NADW) flows southward, crosses the equator and joins the flows in the Southern Ocean. The outflow from the North Atlantic is compensated by water coming through the Drake Passage (about 10 Sv) and water coming from the Indian Ocean through the Agulhas Current system (about 4 Sv). Part of the latter “Agulhas Leakage” may originate from Pacific water that flows through the Indonesian Archipelago. We refer to earlier reviews [Gordon, 1986; Schmitz, 1995; WOCE, 2001] for more complete information on the circulation in each major ocean basin as well as from one basin to another.

Changes in the ocean circulation can influence climate substantially through their impact on both the meridional and zonal heat transport. This can affect mean global temperature and precipitation, as well as their distribution in space and time. Subtle changes in the North Atlantic surface circulation and their interactions with the overlying atmosphere are thought to be involved in climate variability on interannual and interdecadal time scales, as observed in the instrumental record of the last century [Martinson *et al.*, 1995; Ghil, 2001]. Changes in the circulation may also occur on a global scale, involving a transition to different large-scale patterns. Such changes may have been involved in the large-amplitude climate variations of the past [Broecker *et al.*, 1985].

1.3. The modeling hierarchy

The climate system is highly complex, its main subsystems have very different characteristic times, and the specific phenomena involved in each one of the climate problems alluded to in the preceding subsections are quite diverse. It is inconceivable, therefore, that a single model could successfully incorporate all the subsystems, capture all the phenomena, and solve all the problems. Hence the concept of a hierarchy of climate models, from the simple to the complex, has been developed about a quarter of a century ago [Schneider and Dickinson, 1974; Ghil and Robertson, 2000].

The simplest, spatially zero-dimensional (0-D) ocean models are so-called box models, used to study the stability [Stommel, 1961] and paleo-evolution [Karaca *et al.*, 1999] of the oceans' thermohaline circulation or biogeochemical cycles [Sarmiento and Toggweiler, 1984; Keir, 1988; Paillard *et al.*, 1993]. There are one-dimensional (1-D) models that consider the vertical structure of the upper ocean, whether the oceanic mixed layer only [Kraus and Turner, 1967; Karaca and Müller, 1989] or the entire thermocline structure.

Two-dimensional (2-D) models of the oceans fall into the two broad categories of “horizontal” and “vertical.” Models which resolve two horizontal coordinates emphasize the study of the oceans’ wind-driven circulation [Cessi and Ierley, 1995; Jiang *et al.*, 1995], while those that consider a meridional section concentrate on the overturning, thermohaline circulation [Cessi and Young, 1992; Quon and Ghil, 1992, 1995; Thual and McWilliams, 1992].

As explained in Section 1.2, the oceans’ circulation is essentially 3-D and, therefore, general circulation models (GCMs) of the ocean are indispensable in understanding oceanic variability [McWilliams, 1996]. The Bryan–Cox model [Bryan *et al.*, 1974; Cox, 1987] has played a seminal role for the development and applications of such models; this role resembles the one played by the UCLA model [Arakawa and Lamb, 1977] in atmospheric modeling. A number of simplified versions of the Bryan–Cox ocean GCM have been used in exploratory studies of multiple mean flows [Bryan, 1986; Marotzke *et al.*, 1988] and oscillatory behavior [Weaver *et al.*, 1991, 1993; Chen and Ghil, 1995, 1996] of the oceans.

In confronting modeling results with observations, one has to realize that it is the largest scales that are best and most reliably captured. This is certainly true in the atmosphere, where global observing systems have existed for half-a-century [Daley, 1991], and even more so in the oceans, where global coverage has been provided more recently, by satellites and long hydrographic sections [Ghil and Malanotte-Rizzoli, 1991; Wunsch, 1996; WOCE, 2001]. The variability of the large scales arises from two sources: (i) the competition among the finite-amplitude instabilities; and (ii) the net effects of the smaller scales of motion. In this review, we concentrate mostly on the former. Dynamical systems theory provides a perfect toolkit for this type of study.

1.4. A unifying framework

It is now widely understood that the climate system contains numerous nonlinear processes and feedbacks, and that its behavior is rather irregular, but not totally random. Dynamical systems theory studies the common features of such nonlinear systems. The theory is most fully developed for systems with a finite number of degrees of freedom [Smale, 1995] and the early and best-known applications to atmospheric and ocean dynamics involved — not surprisingly — a small number of degrees of freedom [Stommel, 1961; Lorenz, 1963a, b; Veronis, 1963, 1966]. This fact has led to a wide-spread perception that dynamical systems theory only applies to “low-order systems,” and hence its concepts are not sufficiently well known or appreciated within the community of oceanographers, meteorologists and other geoscientists.

The dynamical systems main results that are most important for the study of climate variability have been summarized by Ghil *et al.* [1991]; they involve essentially bifurcation theory [Guckenheimer and Holmes, 1990] and the ergodic theory of dynamical systems [Eckmann and Ruelle, 1985]. Bifurcation theory studies changes in the qualitative behavior of a dynamical system as one or more of its parameters changes. The results of this theory permit one to follow systematically climatic behavior from the simplest kind of model solutions to the most complex, from single to multiple equilibria and on to periodic, chaotic and fully turbulent solutions. Ergodic theory connects the dynamics of a system with its statistics.

We here sketch the basic concepts of bifurcation theory for a general system of ordinary differential equations (ODEs) which can be written as

$$\frac{d\mathbf{x}}{dt} = \mathbf{f}(\mathbf{x}, \mathbf{p}, t). \quad (1)$$

Here \mathbf{x} is the state vector in the state space \mathcal{R}^n , where n indicates the number of degrees of freedom. The right-hand side \mathbf{f} contains the model dynamics; it depends on \mathbf{x} in a nonlinear fashion, on time t and on the vector \mathbf{p} of p parameters, where typically $p \ll n$. The ODE system (1) defines a dynamical system in continuous time, provided solutions exist and are unique for all times, $-\infty < t < \infty$. The system is called autonomous if \mathbf{f} does not depend explicitly on time. A *trajectory* of the dynamical system, starting at the initial state $\mathbf{x}(t_0) = \mathbf{x}_0$, is a curve $\Gamma = \{\mathbf{x}(t) : -\infty < t < \infty\}$ in the phase space that satisfies (1).

A solution $\mathbf{x}(t) = \bar{\mathbf{x}}$ of an autonomous ODE system is called a *fixed point* if

$$\mathbf{f}(\bar{\mathbf{x}}, \bar{\mathbf{p}}) = 0, \quad (2)$$

and hence a trajectory for which $\mathbf{x}(t) = \bar{\mathbf{x}}$ at any time t will remain there forever. Linear stability analysis of a particular fixed point $(\bar{\mathbf{x}}, \bar{\mathbf{p}})$ considers infinitesimally small perturbations \mathbf{y} , i.e.,

$$\mathbf{x} = \bar{\mathbf{x}} + \mathbf{y}; \quad (3)$$

linearization of (1) around $\bar{\mathbf{x}}$ then gives

$$\frac{d\mathbf{y}}{dt} = \mathbf{J}(\bar{\mathbf{x}}, \bar{\mathbf{p}})\mathbf{y}, \quad (4)$$

where \mathbf{J} is the Jacobian matrix

$$\mathbf{J} = \begin{pmatrix} \frac{\partial f_1}{\partial x_1} & \cdots & \frac{\partial f_1}{\partial x_n} \\ \cdots & \cdots & \cdots \\ \frac{\partial f_n}{\partial x_1} & \cdots & \frac{\partial f_n}{\partial x_n} \end{pmatrix}. \quad (5)$$

The linear, autonomous ODE system (4) has solutions of the form $\mathbf{y}(t) = e^{\sigma t}\hat{\mathbf{y}}$. Substituting such a solution into (4) leads to an eigenvalue problem for the complex growth factor $\sigma = \sigma_r + i\sigma_i$, i.e.

Those fixed points for which eigenvalues with $\sigma_r > 0$ exist are unstable, since the perturbations are exponentially growing. Fixed points for which all eigenvalues have $\sigma_r < 0$ are linearly stable.

Discretization of the systems of partial differential equations (PDEs) that govern oceanic and other geophysical flows [Gill, 1982; Pedlosky, 1987, 1996] leads to a system of ODEs (1), with n large. In many cases, the linearization (3)–(5) yields solutions that are the classical linear waves of geophysical fluid dynamics. These include neutrally stable waves, like Rossby or Kelvin waves, or unstable ones, like those associated with the barotropic or baroclinic instability of ocean currents.

If the number of solutions or their stability properties change as a parameter is varied, a qualitative change occurs in the behavior of the dynamical system: the system is then said to undergo a *bifurcation*. The points at which bifurcations occur are called bifurcation points or critical points. A bifurcation diagram for a particular system (1) is a graph in which the variation of its solutions is displayed in the phase–parameter space. Information on the most elementary bifurcations is presented in Box 2.

Box 2

Bifurcation theory goes beyond classical, linear analysis in studying the nonlinear saturation of and interactions between linear instabilities. When the interaction between several instabilities leads to irregular, apparently random behavior, ergodic theory sheds light on the statistics of this behavior.

In the early 1960s, it was possible to compute the first one or two bifurcations analytically and one or two more by the modest computational means of that time, all this for systems with about ten degrees of freedom or less [Lorenz, 1963a, b; Veronis, 1963, 1966]. In the mid-1970s, it became possible to do so for spatially 1-D energy balance models, ei-

ther discretized by spectral truncation [Held and Suarez, 1974; North, 1975; North *et al.*, 1983] or even by a full treatment of the governing PDEs [Ghil, 1976]. The numerical techniques to do so, so-called continuation techniques, are described elsewhere [Doedel and Tuckermann, 2000; Dijkstra, 2000]. Legras and Ghil [1985] were the first to apply a continuation method to a problem in geophysical fluid dynamics. Their atmospheric model had 25 spherical harmonics. In the last few years, bifurcation sequences have been computed for 2-D [Cessi and Young, 1992; Quon and Ghil, 1992, 1995; Speich *et al.*, 1995; Dijkstra and Molemaker, 1997] and 3-D [Chen and Ghil, 1996; Ghil and Robertson, 2000; Dijkstra *et al.*, 2001] climate models with thousands or even tens of thousands of degrees-of-freedom.

Simplified GCMs — atmospheric, oceanic, and coupled — have thus become amenable to a systematic study of their large-scale variability. For systems that have an even larger number of degrees of freedom, such as full-scale ocean and coupled ocean–atmosphere GCMs, with $n = \mathcal{O}(10^6)$ and higher, bifurcation points can be inferred by performing time-dependent forward integrations for several parameter values and monitor changes in qualitative behavior. This type of “poor man’s continuation” has been applied successfully for models of the wind-driven [Jiang *et al.*, 1995; Chang *et al.*, 2001] and thermohaline [Quon and Ghil, 1992, 1995; Chen and Ghil, 1996] circulation.

2. THE WIND-DRIVEN CIRCULATION

A central problem of oceanography is to understand the physics of the near-surface ocean circulation and its variability on time scales from several months to several years. We focus in this section on the North Atlantic, for two reasons: (i) it is an ocean basin for which relatively many observations are available; and (ii) the circulation in this basin

is highly relevant to climate change over the surrounding, highly populated continental areas.

2.1. Observations

The wind-stress curl induced by the easterly winds in very low and very high latitudes, on the one hand, and the midlatitude westerlies, on the other, induces midlatitude cellular flows, called *gyres*. The North Atlantic is typical of several other ocean basins in exhibiting a dominant anticyclonic cell, called the subtropical gyre, and a smaller cyclonic cell, called the subpolar gyre. Each of these gyres has a narrow, fast-flowing western boundary current and a slower, more diffuse eastern boundary current.

Figure 3 gives a rough view of the near-surface flow in the northwestern part of the North Atlantic basin, based on a multipass image of the sea-surface temperature (SST) field, as obtained from infrared sensing by satellite. Here, orange colors indicate a warm sea surface, with SSTs of typically 25°C in the Gulf of Mexico and the Florida Straits. These warm waters are advected northwards, along the East Coast of the U.S., by the strong Florida Current. After separation from the coast near Cape Hatteras, this current becomes the Gulf Stream; typical temperatures near the separation point are 15°C. The northern boundary of the Gulf Stream is characterized by a strong meridional temperature gradient, which is referred to as the North Wall or Cold Wall.

The mean position of the Gulf Stream in the North Atlantic has fascinated oceanographers since its early description by Benjamin Franklin and Timothy Folger [Richardson, 1980]. From the enormous amount of data obtained since then, using ship observations and satellite data, the time-mean path of the Gulf Stream is now well known [Auer, 1987; Lee and Cornillon, 1995]. The Florida Current (see Fig. 3) flows almost parallel to

Figure 3

the coastline and, after separation, the Gulf Stream flows to the east-northeast, approximately along 40°N . This nearly eastward jet is accompanied by vigorous recirculation regions north and south of it [Hogg *et al.*, 1986; Feliks and Ghil, 1996]. Near Cape Hatteras, the volume transport is estimated to be about 50–65 Sv and it increases to a total of about 145 Sv at 60°W [Johns *et al.*, 1995]. The position of the separation point is fairly stable, changing by less than about 50 km over several years.

The variability of the Gulf Stream has been studied for decades through time-continuous *in situ* measurements, at a few locations, as well as by more detailed one-time-only hydrographic surveys. More recently, these data have been complemented with satellite-derived observations, which provide fairly complete and detailed spatio-temporal coverage [Vazquez *et al.*, 1990; Wang and Koblinsky, 1995]. Rossby waves form an important component of the temporal variability of the midlatitude oceans and their analysis has attracted considerable attention of the last few decades [LeBlond and Mysak, 1978; Gill, 1982; Pedlosky, 1987]. Their signature can now be tracked through satellite altimetry [Fu and Cheney, 1995] in the sea-surface height field [Chelton and Schlax, 1996], in spite of the fact that they might only represent only a fairly small fraction of the total variance (5–15%, cf. Gaspar and Wunsch [1989]). As the Gulf Stream penetrates further east into the open ocean, it spreads out due to meandering. In this region, cut-off eddies are formed and move away from the main jet, generally in a westward or southwestward direction. Their average wavelength is about 100 km and their propagation speed is of the order of 10 km/day. The scale of the eddies is related to an internal length scale of the ocean, the internal Rossby deformation radius [Robinson, 1983; Pedlosky, 1987]; both stratification and rotation effects contribute to define this radius [Feliks and Ghil, 1996]. In the oceans,

motions with this horizontal scale are commonly referred to as *mesoscale*. Generally, the presence of mesoscale eddies causes variability on a subannual, 2–3-month time scale.

The last decade has seen a huge increase in the observational information available on the oceans' basin and global scales [Wunsch, 1996; Ghil *et al.*, 1997; WOCE, 2001]. As a result, attention has focused more and more on the temporal variability of the wind-driven circulation that is associated with these larger spatial scales [Fu and Smith, 1996] and involves lower frequencies [Pedlosky, 1996]. The eddy kinetic energy distribution determined by long-term ship-drift and satellite-tracked drifter data shows a maximum of variability in the western part of the mid-latitude ocean basins, along the western boundary currents and their eastward extension [Wyrтки *et al.*, 1971; Brugge, 1995]. Various observations — though limited in spatial and temporal coverage — suggest the existence of distinct scales of temporal variability from subannual [Lee and Cornillon, 1995], through seasonal [Ichikawa and Beardsley, 1993; Schott and Molinari, 1996] to interannual [Mizuno and White, 1993; Auer, 1987] scales.

The sources of this low-frequency variability and of the associated spatio-temporal patterns have become an object of intense scrutiny. The classical view is that the overall red spectrum of the oceans' variability in time is due to its “flywheel” integration of atmospheric white noise [Hasselmann, 1976; Frankignoul and Hasselmann, 1977] and that any peaks that rise above this broad-band spectrum also result primarily from changes in the external forcing, especially in wind stress or buoyancy fluxes.

The forced variability does not always account, however, for all or even most of the observed variability. For example, Niiler and Richardson [1973] noted a discrepancy between the observed seasonal variability of the Florida Current transport and the transport

calculated as a passive response to seasonally varying winds. Dommenget and Latif [2000] have found that the spectrum of mid-latitude SST variability in several coupled GCMs, each with a fully dynamical ocean model, is significantly different from a red-noise process. Internal ocean dynamics — i.e., intrinsic variability due to nonlinear interactions between two or more physical processes that affect the wind-driven ocean circulation — seems therefore to play an important role on these time scales.

2.2. Classical theory and numerical simulations

The intensification of western boundary currents was first explained using steady, linear, rectangular-basin models [Stommel, 1948; Munk, 1950]. In the open ocean, away from boundaries, the flow in these simple models is dominated by Sverdrup [1947] balance between the wind forcing and the latitudinally varying Coriolis forces, the so-called β -effect; here β is the meridional derivative of the Coriolis parameter (see Gill [1982] or Pedlosky [1987]). The β -effect leads to east–west asymmetry in the flow pattern, with streamlines more closely bunched near the western than near the eastern boundary [Stommel, 1951]. In the boundary layer that forms near the former, lateral as well as bottom friction counteracts the increased shear; the inclusion of the one or the other leads to the Munk and Stommel boundary layer structures, respectively.

The wind-driven flows are susceptible to barotropic and baroclinic instability, which lead to time-dependent behavior. The growth of perturbations and their interaction with the background state, as well as with each other, lead to a modification of the mean state and to the prevalence of the time-dependent mesoscale features that were discussed in Section 2.1. High-resolution ocean GCMs, with realistic continental geometry and bathymetry have been run either globally or for the Atlantic region [Semtner and Chervin, 1992;

Stammer *et al.*, 1994; New *et al.*, 1995; Chao *et al.*, 1996; McWilliams, 1996; Smith *et al.*, 2000]. The results of these numerical simulations show large internal variability on a wide range of space and time scales and the influence of the eddies on the mean flow. The GCM results are, however, not always easier to interpret than the observations, with which they share many physical processes and scales of motion.

For example, model resolution strongly affects the mean flow path of the Gulf Stream, in particular its separation near Cape Hatteras. In models with a horizontal mesh size of 1° or larger [Holland and Bryan, 1994; Gerdes and Köberle, 1995; Chassignet *et al.*, 2000], separation of the Gulf Stream is very diffuse, being spread out between Cape Hatteras and Newfoundland, and no recirculation regions are present: the stream north of Cape Hatteras appears as a rather broad band that continues to follow the coastline. For higher-resolution models with a horizontal mesh size of $1/3^\circ$ – $1/6^\circ$ [Beckmann *et al.*, 1994; Bryan *et al.*, 1995; Chao *et al.*, 1996], the time-mean state shows a sizable anticyclonic gyre northeast of Cape Hatteras but the actual separation still occurs north of the observed position and the simulated ocean heat transport is therefore incorrect. Only at a very high horizontal resolution, of 0.1° or higher, at which eddies are well simulated, does the Gulf Stream tend to separate at the correct position [Smith *et al.*, 2000]. The root-mean square sea-surface height variability simulated at this resolution is also in good agreement with the one reconstructed by blending altimeter data from the TOPEX-POSEIDON and the ERS1/2 satellites [Le Traon *et al.*, 1998].

These GCM simulations clearly show that it is necessary to have a mesh size that is well below the Rossby deformation radius in order to obtain Gulf Stream separation at the correct location. Still, it is far from clear which physical processes control the separation

process. Haidvogel *et al.* [1992] and Dengg *et al.* [1996] have reviewed the problem of Gulf Stream separation. Both external factors — such as bottom topography or the wind-stress field — and internal ones — such as adverse pressure gradients [Schlichting, 1968; Tansley and Marshall, 2001; Ghil *et al.*, 2004] or the outcropping of isopycnals [Gangopadhyay *et al.*, 1992; Chassignet and Bleck, 1993] — play an important role. Several studies using idealized models have tried to isolate only one or two factors as decisive but the relation between these results and those obtained by using more realistic models and observations is hard to establish. The tools of bifurcation and ergodic theory are thus essential to explore systematically the results of the full hierarchy of ocean models.

The fact that the wind-driven circulation of the major ocean basins contains typically a subtropical gyre that greatly exceeds in size and strength the subpolar gyre has led to applying these tools to two types of idealized models. Single-gyre models study the subtropical gyre only, while double-gyre models study a subtropical and a subpolar gyre of equal or nearly equal strength. In a sense, the two types of models bracket the midlatitude ocean basins' real circulation.

2.3. Successive bifurcations in equivalent-barotropic models

Following the pioneering work of Veronis [1963, 1966], a systematic analysis of bifurcations in the wind-driven ocean circulation has been carried out by several authors in the mid-1990s. Cessi and Ierley [1995], in particular, used a quasi-geostrophic (QG) barotropic model, while Jiang *et al.* [1993, 1995], used a reduced-gravity shallow-water model (see Box 3).

Jiang *et al.* [1995] computed transient double-gyre flow for different values of the nondimensional wind-stress forcing strength α_τ , using a horizontal resolution of 20 km. For

Box 3

each value of α_τ , they monitored the position of the confluence point, i.e. the merging point of the two separated western boundary currents, and its variability in time. For small values of α_τ , a unique, nearly symmetric flow is found for which the confluence point is displaced slightly northward of the basins' mid-axis. This solution is necessarily stable to small perturbations, since it is attained by forward integration.

For larger values of α_τ , multiple stable equilibria were found: a second steady-state solution has its confluence point lying south of the mid-basin axis. Spatial patterns of the stable stationary thickness field $h = h(x, y)$ for both types of solutions are shown in Figs. 4b and 4c for $\alpha_\tau = 0.9$. The bifurcation diagram proposed by Jiang *et al.* [1995] is shown in Fig. 4a and the solution structure corresponds to that of an imperfect pitchfork bifurcation (see Box 2 and Fig. 3). In this figure, the heavy solid lines represent actually computed values of the steady-state confluence point, while the heavy dashed lines represent an inferred branch of unstable steady states.

Figs. 4

Both stable equilibria become unstable at larger wind-stress strength, and stable periodic solutions arise from either solution branch. One of these two limit cycles has a period of about 2.8 years and is characterized by an oscillation of the confluence point over a distance of about 100 km. This variation in the meridional position of the eastward jet is accompanied by a periodically varying strength of the recirculation regions. For larger values of α_τ , aperiodic solutions are obtained for which the position of the confluence point makes even larger excursions.

Speich *et al.* [1995] followed up on the Jiang *et al.* [1995] work by studying the bifurcation structure of their 1.5-layer shallow-water model using continuation techniques (see Sec. 1.4 and references there). The exact position of the saddle-node bifurcation point in

Fig. 4a could thus be calculated explicitly. Moreover, the Hopf bifurcations (see Box 2) that destabilize both steady-state branches were determined, and so were the spatial patterns of the linear oscillatory modes that lead to these instabilities. These authors used singular-spectrum analysis (SSA; [Ghil and Vautard, 1991; Ghil *et al.*, 2002a]) to compare the periods of these modes to those obtained for the Gulf Stream and Kuroshio axis in Cooperative Ocean-Atmosphere Data Set (COADS) data.

The results above raise a number of fundamental questions, such as the physical origin of the multiple equilibria, the nature of the oscillatory instabilities, and the transition route to irregular behavior for large wind-stress forcing.

2.3.1. The origin of multiple steady states.

The shallow-water model can be simplified further when the Rossby number ϵ is sufficiently small (see Box 3). Under these conditions, QG theory is an adequate approximation of the flow dynamics [Pedlosky, 1987]. Cessi and Ierley [1995] computed stationary solutions of the single-layer QG equations in a small rectangular basin by using a Newton-Raphson method. Multiple equilibria were found when the value of lateral friction coefficient A_H was decreased, with as many as seven occurring in a small area of the parameter plane investigated.

Dijkstra and Katsman [1997], using continuation techniques, determined the detailed bifurcation structure of the Cessi and Ierley [1995] QG model. At large values of the lateral friction A_H , there is only one steady state, which is the antisymmetric double-gyre pattern. When A_H is decreased, this flow undergoes a perfect pitchfork bifurcation and two stable asymmetric states appear. The existence of the perfect pitchfork bifurcation was already shown by Jiang *et al.* [1993, 1995] in a low-order truncated QG model (see

Box 3). The multiple equilibria arise by spontaneous symmetry breaking: the solutions on the asymmetric branches have the jet displaced either southward or northward, similar to those in Figs. 4, but the two QG solutions that coexist for exactly the same parameter values are now perfect mirror images of each other.

The shallow-water equations are not invariant under reflection symmetry with respect to the basins' mid-axis and hence no perfect pitchfork bifurcation can occur. Small deviations from the equilibrium thermocline depth, even at low forcing or high lateral friction, induce an imperfection which perturbs the pitchfork bifurcation. Dijkstra and Molemaker [1999] worked out explicitly the connection between the bifurcation diagrams of the QG and shallow-water models and showed that the occurrence of multiple equilibria in the shallow-water model does have its origin in the QG model's symmetry breaking, as conjectured by Jiang *et al.* [1995].

Barotropic processes dominate the physical mechanism of the instability. Dijkstra and Katsman [1997] observed this in their two-layer QG model, which included baroclinic processes but exhibited essentially the same primary pitchfork bifurcation as the barotropic QG model of Cessi and Ierley [1995]. Ghil *et al.* [2002b] used a QG model in which the vertical stratification was captured by projection onto the two leading eigenmodes of the vertical structure equation [Flierl, 1978; Feliks and Ghil, 1996]. These authors showed explicitly that the first baroclinic mode exhibits the same horizontal pattern as the barotropic mode at the point of symmetry breaking.

2.3.2. The origin of temporal variability.

Hopf bifurcations destabilize the steady solutions as the forcing increases (see Fig. 4a here) or lateral friction decreases (see Fig. 4 in Jiang *et al.* [1995]). The spatio-temporal

pattern of the most unstable oscillatory mode $\Phi(t)$ can be determined from the solution of the linear stability problem (6). The complex eigenvalue $\sigma = \sigma_r + i\sigma_i$ and associated eigenfunction $\hat{\mathbf{x}} = \hat{\mathbf{x}}_r + i\hat{\mathbf{x}}_i$ provide the mode $\Phi(t)$,

$$\Phi(t) = e^{\sigma_r t} [\hat{\mathbf{x}}_r \cos(\sigma_i t) - \hat{\mathbf{x}}_i \sin(\sigma_i t)], \quad (7)$$

with angular frequency σ_i and growth rate $\sigma_r > 0$, which destabilizes the steady state. The period \mathcal{P} of the oscillatory factor in (7) is given by $\mathcal{P} = 2\pi/\sigma_i$.

For the one- and two-layer QG and shallow-water models, three classes of modes may destabilize the steady states. Jiang et al.'s [1995] 1.5-layer shallow-water model captures only equivalent-barotropic processes. In this model, two of these three classes arise at the Hopf bifurcations shown in Fig. 4a. The upper branch becomes unstable through a so-called (recirculation) *gyre mode* [Speich *et al.*, 1995]. The two centers of action of this mode are located within the vigorous recirculation regions near the confluence point of the two separated boundary currents, and the pattern straddles the time-mean axis of the eastward jet. Simonnet and Dijkstra [2002] have shown that the gyre modes do arise ultimately by a merger between stationary modes. The unstable, purely exponential modes that merge are both related to the symmetry-breaking pitchfork bifurcation. The destabilization mechanism is a shear instability, and is essentially independent of Rossby-wave dynamics.

The lower branch in Fig. 4a becomes unstable through a mode that has a subannual oscillation period; such modes are referred to as (Rossby) *basin modes* [Pedlosky, 1987]. The latter are basically a superposition of free westward propagating Rossby waves, whose sum satisfies the boundary conditions. The gravest barotropic ocean basin mode has a one-cell spatial structure in both horizontal directions; its period is about 20 days, which

is only slightly increased by the presence of friction. These otherwise neutral basin modes are destabilized through the presence of horizontal shear and lead therewith to variability on this very short time scale of a month or less. Similar oscillatory instabilities are found in the equivalent-barotropic version of Dijkstra and Katsman's (1997) QG model and are closely linked to those in the shallow-water model [Dijkstra and Molemaker, 1999]. Chang *et al.* [2001] found that such a basin mode plays an important role in a barotropic QG model at high values of the forcing and in a fairly turbulent regime.

In two-layer [Dijkstra and Katsman, 1997] and two-mode [Ghil *et al.*, 2002b] models, additional baroclinic instabilities occur, whose spatial patterns resemble those that destabilize a zonal eastward jet [Eady, 1949; Pedlosky, 1987]. This third class of oscillatory instabilities has subannual periods and represents classical baroclinic modes, modified to some extent by the geometry of the mean flow.

2.4. Low- and ultra-low-frequency results

The results in the previous section describe the lowest branches of the bifurcation tree, where steady-state behavior with highly symmetric spatial patterns changes into richer spatio-temporal behavior of the flow, once the forcing increases or the friction decreases. The periods associated with these first few bifurcations — from months to years — are typically comparable to or longer than those associated with mesoscale variability. How does this bifurcation structure relate to time-dependent flows obtained by numerical simulations using similar or somewhat more detailed models?

McCalpin and Haidvogel [1996] investigated the time-dependent solutions of an equivalent-barotropic QG model for a basin of realistic size (3600×2800 km), as well as the sensitivity of solutions to the magnitude of the wind stress and its meridional pro-

file. They classified solutions according to their basin-averaged kinetic energy, and found three persistent states in their simulations (Fig. 5a). High-energy states are characterized by near-symmetry with respect to the mid-axis, weak meandering, and large jet penetration into the basin interior (Fig. 5b, left panel). Low-energy states have a strongly meandering jet that extends but a short way into the basin (Fig. 5b, right panel), while intermediate-energy states resemble the time-averaged flow and have a spatial pattern somewhere between high- and low-energy states (not shown). The persistence of the solutions near either state is irregular but can last for more than a decade of simulated time (Fig. 5a). Compared to the interannual periods obtained by Hopf bifurcations, we shall refer to this type of variability as (inter)decadal or *ultra-low-frequency*. Berloff and McWilliams [1999] studied a two-layer QG model with a constant-in-time, symmetric double-gyre forcing. They also found that, at relatively low values of the lateral friction coefficient, the flow patterns hover for extended intervals near three states, each with a distinct total energy.

The ultra-low-frequency variability has been attributed to the interaction of meso-scale eddies [Berloff and McWilliams, 1999], to regime switches associated with transitions between different steady states [Primeau, 1998, 2002] and, most recently, to the existence of global bifurcations [Meacham, 2000; Chang *et al.*, 2001; Nadiga and Luce, 2001]. Chang *et al.* [2001] and Simonnet *et al.* [2003b] provide fairly convincing numerical evidence for the existence of a so-called homoclinic bifurcation in QG models. For high forcing, their upper-branch, high-energy time-dependent solutions are destabilized through this global bifurcation, and give rise to a lower-branch, low-energy state. Nadiga and Luce [2001] analyzed in detail such a global bifurcation in a 1.5-layer QG model and associated the

Fig. 5

transition to aperiodic behavior in it with the so-called Shilnikov [1965] phenomenon of successive homoclinic bifurcations [Ghil and Childress, 1987; Guckenheimer and Holmes, 1990].

To summarize, many of the idealized models used so far to study the low-frequency behavior of the wind-driven double-gyre circulation exhibit very similar bifurcation behavior. This behavior helps understand the complex dynamics in the high-forcing, low-dissipation regime that best describes the observed ocean circulation, insofar as basin-scale, subannual and interannual variability is concerned. The dynamical origin of the ultra-low-frequency, decadal and interdecadal variability, is still under dispute. This variability appears to be associated with alternations between two or three states that are characterized by different basin-scale energy levels and jet-penetration scales, but the mechanism of the transitions between these states requires further clarification.

2.5. External asymmetries

In this section we consider two kinds of asymmetries: (i) the forcing by a wind-stress field that leads to a single-gyre circulation; and (ii) the asymmetry due to the coastal geometry of the North Atlantic basin.

2.5.1. Forcing asymmetries.

We saw in Sec. 2.3.1 that, in a QG model, a purely zonal wind stress with a meridional profile that is symmetric about the mid-basin axis of a rectangular basin leads to a perfect pitchfork bifurcation. As soon as the wind stress has the slightest asymmetric component, this pitchfork bifurcation breaks up and the branches become disconnected [Jiang *et al.*, 1995]. As one proceeds towards a single-gyre situation, one of the two disconnected branches totally disappears [Jerley and Sheremet, 1995; Kamenkovich *et al.*, 1995].

Sheremet *et al.* [1997] plotted the bifurcation diagram for the single-gyre problem as the maximum nondimensional transport Q versus the Reynolds number Re (see Box 3). For small Re , the unique stable branch tends to the Munk-Sverdrup solution [Sverdrup, 1947; Munk, 1950]. Multiple equilibria appear through emergence of two back-to-back saddle-node bifurcations, as Re increases. Pedlosky [1996] refers to the high Q values and associated strong recirculation on the upper branch of this S-shaped bifurcation curve as “inertial runaway.”

Sheremet *et al.* [1997] found five classes of internal modes in single-gyre flows. The first class are the Rossby basin modes, of which several can exhibit positive growth rates for sufficiently large Re . Wall-trapped modes are associated with boundary-layer instability. There are two types of modes that are mainly confined to the inertial recirculation gyres, stationary recirculation modes and oscillatory recirculation-zone modes. A fifth class of modes arises from a resonant interaction between the recirculation gyre and certain Rossby basin modes. A number of eddies on the southern flank of the recirculation gyre are prominent in this mode’s spatial pattern. Chang *et al.* [2001] clarified the connection between this resonance mode of Sheremet *et al.* [1997] in the single-gyre problem and the gyre mode of Speich *et al.* [1995] in the double-gyre problem.

Berloff and Meacham [1997, 1998] studied in detail the time-dependent behavior of the single-gyre flows. The connection between this behavior and the bifurcation structures and instability modes discussed above is, however, not as complete as for the double-gyre problem. The connection between the oscillatory modes in the single- and double-gyre flows would also bear a more systematic investigation than the tentative parallels drawn so far.

2.5.2. Geometric asymmetries.

Dijkstra and Molemaker [1999] and Schmeits and Dijkstra [2000] performed numerical bifurcation studies for realistic basin geometry and wind-stress forcing. Dijkstra and Molemaker [1999] have shown in a β -plane shallow-water model that the perturbed pitchfork bifurcation found in the double-gyre flows within a rectangular basin remains robust, given a more realistic geometry. Schmeits and Dijkstra [2000] considered the North Atlantic basin over the domain (5° – 85° W, 10° – 65° N) within a barotropic shallow-water model on the sphere, with constant depth $D = 1000$ m. The bifurcation diagram obtained at a horizontal resolution of 0.5° is shown in Fig. 6a, by plotting the maximum dimensional northward transport versus the Ekman number $E = A_H/(2\Omega r_0^2)$.

Fig. 6

Figure 6a demonstrates that a more realistic continental geometry does not alter the existence of a perturbed pitchfork bifurcation. Two solution branches are found for $E < 2.2 \times 10^{-7}$, both of which are unstable. A solution on the lower branch is shown as a contour plot of layer-thickness anomalies for $E = 1.6 \times 10^{-7}$ in Fig. 6b. It displays the double-gyre circulation, typical for the North Atlantic Ocean, with a ‘deflected’ Gulf Stream which separates too far north compared to the observed. The southern recirculation in this solution is weak and, at this value of E , the transport is about 46 Sv, considerably smaller than observed (see Sec. 3.1).

The upper branch exists only for $E < 2.2 \times 10^{-7}$. The solution at $E = 1.6 \times 10^{-7}$ (Fig. 6c) shows a ‘separated’ Gulf Stream that actually seems to separate twice, once near Cape Hatteras and also off the Great Banks. The circulation patterns outside the western boundary current and the recirculation regions are very similar, so that the multiple equilibria are related to the different separation behavior of the Gulf Stream. On the upper

branch, the recirculation off Cape Hatteras is much more vigorous and the northward transport equals or exceeds the observed.

On the lower branch in Fig. 6a, a Hopf bifurcation occurs at $E = 2.5 \times 10^{-7}$ and is marked with H_1 . The linear oscillatory instability is shown at two phases, one-quarter period apart, in Figs. 6d,e. The maximum amplitude of the mode is located near the axis of the western boundary current and it propagates upstream. The perturbation has a period of 6 months and a wavelength of about 550 km; its cross-stream components cause the Gulf Stream to meander.

Schmeits and Dijkstra [2000] computed a regime diagram that separates steady from oscillatory behavior and has the layer thickness D as the second parameter. The spatial pattern of the neutral mode does not change much as D is varied over a range of about 100 m, but the period of the subannual oscillation increases from 6 to 11 months. This range of periods brackets the 9-month period in meandering intensity found by Lee and Cornillon [1995] in SST observations.

2.6. Relevance to the North Atlantic circulation

A hierarchy of equivalent-barotropic models show that multiple mean flows seem dynamically possible for the North Atlantic wind-driven circulation. The existence of multiple mean Gulf Stream paths can be traced back to its dynamic origin: a symmetry breaking pitchfork bifurcation within the equivalent-barotropic QG double-gyre flow in a rectangular basin. Numerical bifurcation methods have helped demonstrate the persistence of qualitative behavior across this hierarchy of models, from QG to shallow-water and from rectangular to realistic geometry. The two stable equilibria in both the QG and shallow-water models can be dubbed the ‘jet-up’ and ‘jet-down’ solutions. They deform into

solutions with different separation behavior of the Gulf Stream near the North American coast in shallow-water models with more realistic basin geometry.

One underlying optimistic idea in our approach is that stationary equilibria do play an important role in determining the time-mean state of the real system. The reasoning follows the one outlined by Ghil and Childress [1987] for a similar application of dynamical systems methods to large-scale atmospheric flows. Steady states may be unstable to one or a few modes; these define directions in state space along which trajectories diverge from the unstable steady state. But they are still stable in most other directions, along which trajectories are attracted towards the given steady state. In this way, multiple steady states act as “ghost equilibria” to guide the trajectory of a time-dependent model. If this is indeed the case, one may be able to find the signature of multiple equilibria in eddy-resolving ocean models and observations, as discussed already in Sec. 2.4 in the context of ultra-low-frequency variability.

Schmeits and Dijkstra [2001] detected transitions between two different Gulf Stream paths in output from a high-resolution simulation of the Parallel Ocean Climate Model (POCM; Stammer *et al.* [1994]). One quasi-steady state turned out to be very similar to the deflected Gulf Stream solution (Fig. 6b) in the equivalent-barotropic shallow-water model on the sphere, while the other one resembles to a large extent the same model’s separated Gulf Stream solution (Fig. 6c). The transitions occur on interannual time scales and the distinct signatures of the two Gulf Stream paths are visible in the deeper layers of the POCM temperature field. This indicates that the transition between the two patterns is a barotropically controlled phenomenon, as predicted by the simple- and intermediate-model studies (see Dijkstra and Katsman [1997], Ghil *et al.* [2002b], and Section 2.3.1

here). Thus, the multiple equilibria of the intermediate models seem to persist in a state-of-the-art GCM such as POCM. Bane and Dewar [1988] have also found bimodal behavior in the Gulf Stream path off South Carolina during the Gulf Stream Deflection and Meander Energetics Experiment (1981-1982): transitions between a weakly and a strongly deflected state seem to occur on a subannual time scale.

For the barotropic component of the North Atlantic circulation, the modes of variability that arise as oscillatory instabilities are easily identified across our hierarchy of the QG and shallow-water models. In the range of parameters studied, only two classes of modes contribute to the variability: the barotropic Rossby-basin modes and the gyre modes. Their time scale and even their spatial pattern depend only weakly on the continental geometry and details of the wind stress. An important reason for this robustness can be found in the rectangular geometry studies, where the gyre modes are strongly localized within the high-shear regions of the recirculation gyre; this feature changes but little across the hierarchy of models. The basin modes have a much broader footprint, but still seem to be affected only moderately by the changes in basic flow and detailed basin geometry. In the baroclinic case, other modes, associated with baroclinic instability of the current system, become important.

Applying dynamical systems theory to the temporal variability of the climate system requires a similarly optimistic assumption, to wit, that each mode of temporal variability can be traced back to a specific Hopf bifurcation; this bifurcation can then be studied in isolation and the physics of the mode can be clarified in detail. Subsequent modifications in a model that incorporates a more complete set of physical processes and spatial detail are then traced by studying time-dependent solutions of the latter model. The barotropic

basin mode, with its subannual time scale, is present throughout the whole model hierarchy and one thus one may be able to detect its signal in output from eddy-resolving models and observations.

Preliminary comparison of some of the models' interannual variability with observed spatio-temporal SST patterns in the North Atlantic [Moron *et al.*, 1998] is quite encouraging. The 7–8-year mode in the observations is strongest in the northwestern part of the subtropical gyre, with a weaker center of opposite polarity in the subpolar gyre and substantial weakening of features towards the east and the south. It thus seems to have noteworthy similarities with the interannual gyre mode [Simonnet *et al.*, 2003a, b].

Multi-channel SSA (M-SSA; Plaut and Vautard [1994]; Ghil *et al.* [2002a]) was applied to sea-surface height and SST observations in the Gulf Stream region to determine dominant variability patterns. Schmeits and Dijkstra [2000] isolated a propagating mode of variability with a time scale close to 9 months. This time scale corresponds to the dominant variability in the Gulf Stream's meandering intensity [Lee and Cornillon, 1995].

Simonnet *et al.* [2003b] performed a 100-year simulation of a 2.5-layer shallow-water model in a North-Atlantic-shaped domain and compared the results with the actual variability of the Gulf Stream axis, as inferred from the Cooperative Ocean-Atmosphere Data Set (COADS) (see Fig. 7). The meridional excursions of the jet axis along the 51°W meridian appear in Fig. 7a. The power spectrum of the interannual portion of this variability is plotted in Fig. 7b, while Fig. 7c shows an interannual power spectrum of model-simulation results. The two spectra are strikingly similar in structure: each exhibits four peaks between one and ten years in period, whose spacing in frequency and relative sizes are roughly the same. The longest period is about 7 years in both spectra,

Fig. 7

close to the 6 years obtained by Speich *et al.* [1995], as well as to the observed 7.7-year peak in Fig. 1b here (see also Moron *et al.* [1998]).

The main results of this section are summarized in Table 3. It appears that both the subannual mode in the observations, with a period of about 9 months, and the interannual one, with a period of about 7–8 years [Da Costa and Colin de Verdière, 2004] can be explained by the model-hierarchy results reviewed herein.

Table 3

3. THE THERMOHALINE CIRCULATION

The buoyancy fluxes at the ocean surface give rise to gradients in temperature and salinity, which produce in turn density gradients. These gradients are, overall, sharper in the vertical than in the horizontal and are associated, therefore, with an overturning or thermohaline circulation (THC). Since the Atlantic is the most active basin in the global ocean circulation, the sensitivity of its THC to perturbations and to changes in forcing is a topic of active research.

3.1. Observations

The downward annual-mean heat flux into the ocean (e.g., Oberhuber [1988]) indicates that, on average, there is net heat input near the equator and net heat loss at higher latitudes. In the North Atlantic and North Pacific, high losses to the atmosphere (exceeding 150 Wm^{-2}) occur near the western boundary currents and their eastward extensions.

The freshwater flux indicates high-precipitation areas near the equator that are associated with the Intertropical Convergence Zone, especially throughout the Tropical Indo-Pacific Ocean; the highest values (exceeding 200 mm/month) occur in the Western Tropical Pacific and the South Pacific Convergence Zone. In the North Atlantic and North

Pacific basins, the subtropical gyres show net excess of evaporation over precipitation, with values of 100 mm/month and more off the west coast of Africa, while the subpolar gyres show a net excess of precipitation. The zonally averaged profile of the freshwater flux does not exhibit any strong asymmetry with respect to the equator, although the data from different sources show substantial variations [Zaucker *et al.*, 1994].

The heat and freshwater fluxes together determine the surface buoyancy flux that acts to force the oceans' THC. There are also direct cryospheric influences through the presence of sea ice and icebergs. Because sea ice has a considerably lower salt content than the ocean water on which it grows, there is a net salt flux into the ocean. When icebergs melt, the surface of the ocean is enriched with fresh water, decreasing its salinity. There are other, more localized fluxes that may be important, such as river outflow, but these are not further considered here.

The transport of salt and heat by the THC is advection-dominated, since lateral mixing is small overall, while vertical mixing is, for the most part, restricted to the upper ocean and near rough topography. Because of the limited amount of mixing, the concept of individual *water masses*, which are separated from each other, has been introduced in classical oceanography [Sverdrup *et al.*, 1946]. Such a water mass is often characterized by its (potential) temperature and salinity at formation, although recent work has shown that probability density functions for related variables, such as tracer transit times, are in fact broader than previously thought [Holzer and Hall, 2000].

The North Atlantic Deepwater (NADW), mentioned in Section 1.2, forms in the subpolar North Atlantic and can be identified as the water having a potential temperature θ of about 3°C in a recently obtained north–south section [Talley, 1999] from the World

Ocean Circulation Experiment (WOCE) at 24°W (Fig. 8). The Antarctic Bottom Water (AABW) forms mainly in the Weddell Sea and enters the Atlantic from the south. It is even denser than NADW, having a potential temperature of about 0.5°C, and thus penetrates below the latter (Fig. 8). The outflow of NADW from the Atlantic is, in addition to the deep inflow of AABW, also compensated by surface inflow from the Indian Ocean and through the Drake Passage [Schmitz, 1995]. The layering of these water masses produces strong vertical stratification in the Atlantic.

The total meridional heat transport due to the ocean circulation is difficult to measure directly. It can, however, be inferred from estimates of the atmospheric transports and constraints on the global energy balance. It is thus estimated that the ocean and atmospheric circulation each carry about half of the total poleward heat transport. In the Atlantic, the meridional transport is northward over the whole basin due to a strongly asymmetric meridional overturning circulation; in situ hydrographic measurements yield 1.2 PW at 24°N [Hall and Bryden, 1982]. In the Pacific, the heat transport is believed to be mainly through wind-driven currents, with a local estimate of 0.8 PW at 24°N [Bryden *et al.*, 1991]. The heat transport in the Indian Ocean is mainly southward and estimated to be 0.4 PW at 30°S [Robbins and Toole, 1997; Ganachaud and Wunsch, 2000]. Held [2001] has provided interesting theoretical arguments for the partition between atmospheric and oceanic transport in low latitudes.

Estimates of freshwater transport through the ocean are even harder to obtain from direct observations. There is net precipitation in the tropical, middle and high-latitude regions and net evaporation in the subtropics. This leads to a net buoyancy flux at the ocean surface that is nearly symmetric about the equator with positive extrema at the

equator and negative ones at about 25°N. The ocean must transport fresh water into the evaporative regions and away from precipitation regions for compensation. Wijffels *et al.* [1992] present estimates of this freshwater transport and demonstrate the importance of the Bering Strait throughflow. The Pacific experiences net precipitation overall, with much of this gain occurring between 0 and 15 °N, the location of the Intertropical Convergence Zone. On the other hand, the Atlantic and Indian Ocean are evaporation-dominated basins. Over the whole North Atlantic, there is southward transport of freshwater with a maximum of about 1 Sv at 45°N [Schmitt *et al.*, 1989].

The THC varies on time scales of decades or longer, as far as we can tell from instrumental and paleoclimatic data [Martinson *et al.*, 1995]. For example, sediment core records in the North Atlantic indicate that changes in deepwater temperatures occurred during Dansgaard-Oeschger oscillations and were, in all likelihood, related to changes in NADW and AABW formation. Few continuous instrumental records with any spatial resolution and useful accuracy exist, however, on these time scales. The largest number of such records is available for the North Atlantic Ocean. These records include measurements of the overflow from the Nordic Seas [Dickson and Brown, 1994], convective activity [Schlösser *et al.*, 1991], repeated ship measurements over the same section [Bryden *et al.*, 1996], and ocean weather stations [Sy *et al.*, 1997; Joyce and Robbins, 1995].

There exist, however, fairly long SST data sets, such as COADS, from which near-surface patterns of variability on interannual to decadal time scales can be inferred; these patterns may be related to THC variability. Deser and Blackmon [1993] have used empirical orthogonal function (EOF) analysis [Preisendorfer, 1988] to determine the dominant spatial variability patterns of SST in the North Atlantic. The first EOF displays a basin-

scale SST pattern of essentially one sign; the strongest anomalies are equal to about 1°C and occur in the Gulf Stream region. The time series that represents the ‘amplitude’ of this pattern, i.e. the leading principal component, indicates that, in the first half of the 20th century, this region was colder than normal, whereas during the century’s second half it has been warmer.

Kushnir’s [1994] statistical analysis of SST and sea-level pressure data indicates that THC variations are involved in the North Atlantic’s interdecadal variability. The dominant pattern of variability he found is basin-wide, strongest in winter, and shows maxima in the vicinity of Iceland and the Labrador Sea. The high-amplitude SST variability in these areas has been linked to variations in convective activity. It is known that deep convection was interrupted in the Labrador Sea over the time interval 1968–1982 due to the presence of the so-called Great Salinity Anomaly [Dickson *et al.*, 1988]. A low-salinity patch of water travelled along a cyclonic path south of Greenland and finally ended up in the North Atlantic, influencing the velocity field along its way.

Moron *et al.*’s [1998] spatio-temporal analysis of the global SST record for the 20th century used M-SSA and showed that global warming in the early part of the century started in the subpolar North Atlantic. The same is true of the current cooling trend that started in the early 1970s and is now shared by most of the North Atlantic and much of the North Pacific; trends in this work were defined by subtracting interannual and interdecadal oscillatory modes.

The change in the ocean’s heat content over the upper 300 m, as compiled in Levitus *et al.* [2000], is plotted in Fig. 9 for the North, South, and whole Atlantic, over the last half-a-century. This plot clearly shows the warming trend of the upper ocean over

Fig. 9

the last century. For comparison, the seasonal cycle of upper-ocean heat content for the North Atlantic has an amplitude of about 5.6×10^{22} J [Levitus *et al.*, 2000], while the interdecadal range is of about 3.8×10^{22} J. The difference patterns in the North Atlantic’s heat content between the pentads 1988–1992 and 1970–74 for two reference depths (300 m and 3000 m; not shown) are strongly aligned with the Gulf Stream: the heat content decreases north of it and increases south of it.

The processes that control these changes on interdecadal time scales are poorly understood so far. To study possible modes of variation of the THC, we review a hierarchy of models.

3.2. Box models and their multiple equilibria

The North Atlantic experiences heat input in low latitudes and heat loss at high latitudes; this induces a poleward density gradient. On the other hand, there is substantial evaporation in low latitudes, which increases the salinity of the water there and hence its density. The surface freshwater flux and heat flux have opposite effects on the large-scale ocean circulation: what happens as the relative importance of the two surface fluxes varies?

Stommel [1961] proposed a minimal model that can be used to study this problem in its simplest form. Two vessels, called boxes, have volumes V_p and V_e and contain well-mixed water of temperature and salinity (T_e, S_e) and (T_p, S_p) ; the subscripts ‘*e*’ and ‘*p*’ indicate the equatorial and polar box, respectively. The boxes are connected at the surface by an overflow region and at the bottom by a capillary tube, to keep the volume in each box constant (Fig. 10a). The flow rate Ψ is directed from high to low pressure and is taken to be directly proportional to the density difference between the two boxes; a linear

Fig. 10

equation of state is also assumed. The exchange of properties does not depend on the sign of Ψ , because it only matters that properties from one box are transported to the other box; the pathway — either through the overflow, or through the capillary — is thus of no importance, because mass is conserved.

Exchange of heat and salt between each box and the atmosphere above is modeled through relaxation to a prescribed surface temperature and salinity (T^a, S^a). The freshwater flux is usually converted into an equivalent salt flux, of the opposite sign. Under appropriate scaling, the dimensionless equations become

$$\frac{dT}{dt} = \eta_1 - T(1 + |T - S|), \quad (8a)$$

$$\frac{dS}{dt} = \eta_2 - S(\eta_3 + |T - S|); \quad (8b)$$

here T and S monitor the equatorial-to-pole temperature and salinity difference, $\Psi = T - S$ is the flow rate, and t indicates time. The parameters η_1 and η_2 represent the strength of the thermal and freshwater forcing, respectively, and η_3 is the ratio of the thermal-versus-freshwater restoring time scales, as discussed below.

Starting from the initial state ($T = 0, S = 0$), the time evolution of a solution $T = T(t), S = S(t)$ of (8) is shown in Fig. 10b for the case $\eta_1 = 3.0, \eta_2 = 0.5$ and $\eta_3 = 0.3$. In this case, the freshwater forcing is relatively small and the flow evolves to a steady state with sinking in the north, called a *thermally-dominated* or TH state, since $\Psi = T - S > 0$. It turns out that, for these parameter values, the same steady state is reached for all initial states, i.e. the TH state is the unique stable equilibrium for this set of parameters.

We now proceed to investigate how this asymptotic behavior of the solutions changes as the parameters are changed. To this effect, we increase the salinity-flux forcing and plot in Fig. 10c three trajectories in the (T, S) plane for the case $\eta_2 = 1.0$, while η_1 and

η_3 have the same values as before. The trajectories starting at the initial states $(0, 0)$ and $(2.5, 2.5)$ approach a steady state with sinking in the polar box, similar to the one pictured in Fig. 10b. However, the trajectory starting at $(3.0, 3.0)$ approaches a steady state with sinking in the equatorial box, called a *salinity-dominated* or SA state, since $\Psi = T - S < 0$. In this case, there are multiple stable equilibria for the same forcing.

Thus TH and SA steady states can coexist in this model if the salinity flux is large enough. Is there a limiting value of η_2 at which these multiple equilibria appear? This question motivates us to look at the steady-state equations and solve directly for the equilibria as a function of the parameters.

We show typical results in Fig. 11a, where Ψ is plotted versus η_2 for $\eta_1 = 3.0$ and $\eta_3 = 0.3$. The two eigenvalues $\sigma_{1,2}$ of the Jacobian matrix of (8) control the stability of each steady state along the three branches and are both real throughout. We indicate the positive or negative sign of the two eigenvalues along each branch. For values of η_2 up to the point L_1 , only the TH solution is linearly stable, while for values beyond L_2 only the SA solution is stable. On the branch that connects the solutions at L_1 and L_2 , one of the eigenvalues is positive and hence this solution is unstable. Between the points L_1 and L_2 , the TH and SA solutions coexist and are both stable. For instance, when the point A (Fig. 11a) is taken as an initial state, the trajectory finally ends up at state B.

The saddle-node bifurcations L_1 and L_2 (see Box 2) represent exact bounds for the region of multiple equilibria, for the given values of η_1 and η_3 . When the position of these points is determined for other values of η_1 , at fixed η_3 , the area in the (η_1, η_2) parameter plane where both TH and SA solutions occur is bounded by two smooth curves (Fig. 11b). To the right of the L_1 -curve, the polar-sinking (TH) solution is unique, whereas to the

Fig. 11

left of the L_2 -curve, the equatorial-sinking (SA) solution is unique. Between the two curves, the TH and SA solutions coexist and are both stable. Such a plot is referred to as a *regime diagram*: it helps understand the difference between Figs. 10b and 10c. For $\eta_1 = 3.0$ and $\eta_2 = 0.5$, as in Fig. 10b, the system always tends to the unique stable TH solution. For the $\eta_1 = 3.0$ and $\eta_2 = 1.0$, the system is in the regime in which stable TH and SA states coexist and hence trajectories with different initial states may approach either steady state.

The multiple equilibria arise due to a positive feedback between the flow and the salt transport, called the salt-advection feedback [Walín, 1985; Welander, 1986; Marotzke *et al.*, 1988; Cessi and Young, 1992; Quon and Ghil, 1992; Thual and McWilliams, 1992; Vellinga, 1996; Dijkstra and Molemaker, 1997]. Figure 11c shows a zonally averaged overturning circulation that is thermally driven. The surface forcing salts and warms the low-latitude region, while it freshens and cools the high-latitude region. If the circulation strengthens, then more salt is transported poleward; this is indicated by the arrows labeled F_S in Fig. 11c. This enhanced salt transport will increase further the density in high latitudes and consequently amplify the original perturbation of the circulation, due to increased deep-water formation there. The strengthening of the circulation also transports more heat northward, as indicated by the arrows labeled F_T ; this will weaken the flow by lowering the density in high latitudes. Heat transport therefore provides a negative feedback on the circulation. Multiple equilibria occur when the positive feedback wins out.

In addition to the salt-advection feedback, the existence of multiple steady states in the THC also depends crucially on the different response times of ocean salinity, τ_S , and

temperature, τ_T , to changes in surface forcing. The atmosphere exerts quite a strong control on SST anomalies, but ocean water salinity does not affect the freshwater flux at all. In general, distinct surface boundary conditions for temperature and salinity are referred to as mixed boundary conditions [Haney, 1971; Welander, 1986; Tziperman *et al.*, 1994]. The extreme case is to prescribe surface temperature, on the one hand, and surface freshwater flux, on the other. In this case, the response time τ_T is zero, while τ_S is not. The parameter η_3 in (8b) is the ratio of τ_T and τ_S .

Welander [1986] and Thual and McWilliams [1992] have studied an extension of the Stommel [1961] box model to include two polar boxes, on either side of the equatorial one. When the forcing is symmetric with respect to the equator, the equations possess a reflection symmetry that makes north and south indistinguishable in the model. The presence of this symmetry has a striking influence on the structure of the steady solutions and their stability.

For small salt-forcing strength, a single symmetric solution exists; it is of TH type, with upwelling at the equator and sinking at both poles. This solution (not shown) can be viewed as being the sum of two TH solutions of the Stommel model that mirror each other. It is a two-cell solution, with one overturning cell in each hemisphere. When the salt forcing is large enough, a symmetry-breaking pitchfork bifurcation occurs (see Box 2). The TH solution becomes unstable and two asymmetric solutions — labelled NPP and SPP — appear. The NPP solution has a single, pole-to-pole overturning cell, with no equatorial upwelling nor downwelling: downwelling occurs in the northern box and upwelling in the southern box. The SPP solution is just the reflection of the NPP

solution in the equator, with downwelling in the southern and upwelling in the northern box.

Box models have also been used to illustrate a convective feedback that may be responsible for multiple equilibria [Welander, 1982; Lenderink and Haarsma, 1994]. Consider a box model with two vertically stacked boxes: one represents the surface ocean that exchanges heat and fresh water with the overlying atmosphere, the other box the deep ocean. Convective exchange between these boxes occurs if the surface water becomes denser than the deep water; the latter is assumed to possess constant temperature and salinity, as the deep-ocean box is much larger than the near-surface box.

Suppose, initially, that the upper ocean is less dense than the deep ocean and no convective exchange occurs, but the upper box is being cooled and freshened through atmospheric exchange. When the situation of colder and fresher water above warmer and saltier water becomes marginally stable, a finite-amplitude, positive-density perturbation in the upper box will induce convection, which mixes warmer and saltier water to the surface. The heat in the surface layer is quickly lost to the atmosphere but the surface salinity is increased and hence convection is maintained, leading to a convective state. Convective and non-convective states may thus coexist over a certain parameter range.

Within simple box models, two types of oscillatory phenomena can also be found. One is associated with propagation of salinity perturbations along the mean thermohaline flow and is referred to as a loop oscillation [Welander, 1986]. The other is associated with repeated transitions between convective and non-convective states. The most elementary box model which includes both types of oscillations is the four-box model originally used by Huang *et al.* [1992] and analyzed in greater detail by Tziperman *et al.* [1994]. This model

includes two deep-ocean boxes, two near-surface boxes and vertical as well as horizontal exchanges of heat and salt.

3.3. Two-dimensional (2-D) models and their relaxation oscillations

The next step in the modeling hierarchy, as described in Sec. 1.3 here, are models that focus on overturning flows in the meridional plane. In 2-D Boussinesq models [Cessi and Young, 1992; Quon and Ghil, 1992; Thual and McWilliams, 1992], rotation and wind-stress forcing are neglected *a priori* (see Box 4).

Box 4

THC solutions within the 2-D Boussinesq models were first obtained for the simplest case of isotropic eddy diffusivities ($R_{HV}^M = R_{HV}^T = 1$, see Box 4) and relatively large depth-to-width ratio A compared to the real ocean [Quon and Ghil, 1992; Thual and McWilliams, 1992]: $A \approx 0.1$ in the models vs. $A = 10^{-3}$ in the Atlantic, say. Since the vertical length scale of the flow is still considerably smaller than the horizontal scale, isotropic diffusivities imply that vertical diffusion is the dominant transport mechanism.

Quon and Ghil [1992] derived the freshwater flux F_S (see Box 4), from model steady states obtained under restoring conditions for both temperature and salinity. The parameter γ was used to measure the strength of this freshwater flux. Still, given equatorially symmetric forcing, a symmetric flow pattern is expected, i.e. the TH pattern, with upwelling near the equator and downwelling near either high-latitude end of the rectangular domain. Steady states were computed by forward integration and their symmetry measured by the difference ϕ_1 between the intensity of the overturning on either side of the equator. A two-parameter parabola was then least-squares fitted to the asymmetric steady states, as shown in Fig. 12a.

Fig. 12

Dijkstra and Molemaker [1997] recomputed the bifurcation diagram by more accurate continuation techniques and for slightly different lateral boundary conditions and their results are shown in Fig. 12b. The value of the meridional-plane streamfunction at the rectangle's center point, which is zero for equatorially symmetric solutions, is shown on the ordinate. The solution at the point labelled b is the thermally driven two-cell TH state, while the solutions at points c and d are single-cell, pole-to-pole solutions — SPP and NPP, respectively.

The agreement between the two bifurcation diagrams in Figs. 12a and 12b is excellent, given the differences in lateral boundary conditions: the point P in Fig. 12b has $\gamma = 0.36$, while $\gamma_0 = 0.40$ in Fig. 12a. In fact, Dijkstra and Molemaker [1997] used somewhat less constraining boundary conditions than Quon and Ghil [1992]. This is expected to shift the pitchfork bifurcation to slightly smaller values, as found in Fig. 12b. By varying the value of Ra , Quon and Ghil [1992] obtained a regime diagram shown here as Fig. 12c; the neutral-stability curve that separates the unique TH equilibria from the multiple, pairwise mirror-symmetric ones is the locus of the pitchfork bifurcations in the (γ, Ra) -plane.

Thual and McWilliams [1992] computed similar bifurcation diagrams and compared systematically these diagrams for box models and for the 2-D Boussinesq model. They found that the simplest “plumbing scheme” that yields the same bifurcation diagram for the ODE system governing a box model as for the (numerically discretized) PDE system in Box 3 has five boxes: one equatorial box and two pairs of polar boxes, near-surface and deep-ocean. There are six pipes that connect each polar surface box to the equatorial one, each deep-water box to the equatorial one, and the two boxes stacked at either pole with each other in the vertical.

Cessi and Young [1992] provided an important verification of the numerical results for the isotropic case in the limit of infinite Prandtl number (see Box 4), $Pr \rightarrow \infty$, and vanishing aspect ratio, $A \rightarrow 0$. An asymptotic expansion of the PDE equations in Box 4 in a very thin domain yields an ODE for the vertically averaged salinity \hat{S} :

$$\hat{S}'' + \mu_1^2 [\hat{S}'(\hat{S}' - T_S')] + \mu_2 F_S = \delta^2 \hat{S}'''' . \tag{9}$$

Here, μ_1 and μ_2 measure the strength of the thermal and freshwater forcing and the primes indicate differentiation with respect to y . The parameter δ allows for the presence of boundary layers with sharp gradients in the N-S direction. Cessi and Young [1992] obtained analytical results for $\delta \rightarrow 0$, but their solutions are not globally defined on the whole y -interval. Dijkstra and Molemaker [1997] computed numerical solutions for nonzero δ in the whole rectangular domain, verified the bifurcation diagrams, and showed that they approached Cessi and Young's [1992] analytical ones for $\delta \rightarrow 0$.

In reality, the aspect ratio is very small, $A = \mathcal{O}(10^{-3})$, but the ratio R_{HV} of vertical and horizontal diffusivities is very small, too. Quon and Ghil [1995] explored 2-D Boussinesq flows in a rectangular domain with small A and $R_{HV} \ll 1$. For a choice of $R_{HV}^M = R_{HV}^T = A = 0.01$, the model behavior was investigated for two different sets of surface boundary conditions. The pitchfork bifurcation from symmetric to asymmetric steady states in this case is similar to the diffusive case. Each branch of asymmetric steady states undergoes a Hopf bifurcation to oscillatory solutions with a period equivalent to thousands of years in dimensional time. In the oscillatory solutions, small-scale convective "chimneys" appear close to the polar wall of the stronger cell. For a broad range of parameters, the oscillations are strongly nonlinear, with a slow, diffusive warming phase and a sudden flush that re-establishes full-strength overturning.

Weijer *et al.* [1999] studied systematically the impact of lateral heat and salt fluxes on the Atlantic overturning. They showed that either a shift in the distribution of the intermediate and thermocline water, which together compensate for NADW export, or a change in their water-mass characteristics, might influence the Atlantic overturning's strength considerably. Dijkstra and Neelin [1999] considered the effects of asymmetry in the distribution of land masses. This leads to a surface freshwater flux that has slightly larger values in high northern than high southern latitudes, but also to an asymmetry in the area of ocean–atmosphere interaction and hence in the surface heat flux [Chen and Ghil, 1995].

These asymmetric effects introduce an imperfection into the pitchfork bifurcation diagram of the equatorially symmetric case. The branch of northern-sinking solutions is preserved when the N–S asymmetry of the freshwater flux is increased, while the branch of southern-sinking solutions eventually disappears. Hence, asymmetry of either air–sea interaction or freshwater flux with respect to the equator induce a preference for northern sinking, due mainly to larger salinification in the North Atlantic.

In the 2-D Boussinesq models above, the effects of wind-stress forcing and rotation were completely neglected. In some of them, moreover, solutions were obtained that contain regions with an unstable density stratification. The reason for such an unrealistic result is that many models of this type do not resolve the small scales at which the nonhydrostatic processes included in the Boussinesq approximation become important. We review next a class of 2-D, zonally averaged models in which the effects of rotation and wind are parameterized. In these ocean models, moreover, explicit procedures are

used to remove the static instabilities; these procedures are collectively referred to as “convective adjustment” [Marotzke, 1991].

When the 3-D primitive equations that govern ocean GCMs [Gill, 1982; Pedlosky, 1987, 1996; McWilliams, 1996] are averaged with respect to longitude, a closure has to be found for several variables, in particular for the zonal pressure difference, in terms of zonally averaged quantities alone [Marotzke *et al.*, 1988]. Wright and colleagues [Wright and Stocker, 1992; Wright *et al.*, 1998] drop the zonal momentum balance and propose a so-called ‘geostrophic’ closure, which postulates the existence of a linear relation between the zonal density difference across the basin and the meridional density gradient. Wright and Stocker [1992] have shown the usefulness of this closure by a comparison with 3-D model results. In a more rigorous analysis based on vorticity dynamics, Wright *et al.* [1995] have shown that a relation between the east–west density difference and the zonally averaged meridional density gradient does indeed exist. In principle, other 2-D models [Marotzke *et al.*, 1988; Sakai and Peltier, 1995; Vellinga, 1996] can be considered as special cases of zonally averaged models, by taking the zonal velocity and all zonal derivatives equal to zero.

Vellinga [1996] performed a bifurcation analysis for several types of zonally averaged models. The pitchfork bifurcation is quite robust in these models, although the TH solutions lose their stability for slightly different values of the strength of the salt-flux forcing. This qualitatively similar behavior in 2-D models that have completely different momentum balances suggests that the essentials of symmetry breaking of the thermally dominated THC do not reside in the dynamics, but in the transport equations for heat

and salt. To break the symmetry it suffices to have a strong enough meridional velocity response to a meridional density gradient.

For stronger overturning flows, the “convective adjustment” that replaces small-scale nonhydrostatic flow in low-resolution 2-D models [Wright and Stocker, 1992], as well as in most ocean GCMs [Cox, 1984; Rahmstorf, 1995a], can lead to the appearance of spurious saddle-node bifurcations. Vellinga [1998] investigated the origin of these artificial multiple steady states. They arise because of the possibility of “convective adjustment” at arbitrary grid points. This feature of several 2-D and 3-D models of the THC demonstrates their extreme sensitivity to finite-amplitude perturbations, since the convective-adjustment procedure only mixes heat and salt locally downward. This sensitivity can already be deduced from the simple Welander [1982] two-box model, where a finite-amplitude perturbation can induce a transition between a quiescent and a convective state, given only vertical transport; it is absent from 2-D Boussinesq models that resolve chimneys explicitly [Quon and Ghil, 1995].

3.4. Three-dimensional (3-D) models

To understand more fully the 3-D aspects of the THC, and eventually its interaction with the wind-driven circulation, more elaborate, 3-D models are necessary. These models include ocean GCMs; this term is typically reserved for 3-D models with fairly realistic bathymetry and equation of state. Until recently, though, spatial resolution has been fairly limited, even in such GCMs, to about $4^\circ \times 4^\circ$ degree horizontally and 12 levels.

Several types of ocean GCMs are reviewed by McWilliams [1996] and Chassignet *et al.* [2000]. The Modular Ocean Model (MOM) [Pacanowski, 1996] and the Parallel Ocean Program (POP; e.g. Smith *et al.* [2000]) are improved descendents of the original Bryan–

Cox model. The Large Scale Geostrophic (LSG) model was suggested by Hasselmann [1982] and subsequently developed, tested and used by Maier-Reimer *et al.* [1993]. The idea behind the LSG model is to filter out the fast phenomena that do not affect, to first order, changes in the ocean on large space and time scales. In Frictional Geostrophic Models (FGMs), the inertia terms and the local accelerations are neglected, while using a rigid-lid surface condition. In the momentum equations additional simplifications are usually made in the form of linear friction [Salmon, 1986; Colin de Verdière, 1988] and no details of basin geometry and bottom topography are included.

3.4.1. Multiple equilibria.

Bryan [1986] used the MOM model to address the issue of multiple equilibria in 3-D ocean models in a full-basin set-up. He obtained first the solution of a single-hemispheric, sectorial version of the model under restoring conditions, using observed salinity over the domain (0–60°E, 0–90°N). This solution and the corresponding surface forcing were reflected across the equator to provide a full-basin solution as an initial state (Fig. 13a). The freshwater flux of this state was diagnosed and used in subsequent runs for which mixed boundary conditions were prescribed.

Fig. 13

When a negative salinity anomaly of 1 psu is suddenly added poleward of 45°S, the deep convection in the Southern Hemisphere is interrupted. The residence time of water parcels in the surface layer increases and leads through the convective feedback to a collapse of the overturning circulation in the Southern Hemisphere; a pole-to-pole circulation is reached within 50 years (Fig. 13b), with sinking in high northern latitudes only. This collapse is referred to as the polar halocline catastrophe and is associated with the equatorward spreading of a tongue of low-salinity water.

Adding a positive salinity anomaly of 2 psu in the same region, poleward of 45°S , induces an intensification of the meridional overturning; this leads, through the advective feedback mechanism, to a southern-sinking solution in about 200 years (Fig. 13c). An initial state with a positive salinity anomaly of 2 psu in the northern subpolar region gave a northern-sinking solution (Fig. 13d), similar to that in Fig. 13b.

Klinger and Marotzke [1999] used a “poor man’s continuation method” to determine bifurcation diagrams of the 3-D double-hemispheric configuration by calculating steady states within the MOM model for many parameter values. In the equatorially symmetric case, the multiplicity of their model’s equilibria appears to arise through a subcritical pitchfork bifurcation. Weijer and Dijkstra [2001] used pseudo-arclength continuation to perform a bifurcation study of the double-hemispheric case. They showed that (i) there is a qualitative similarity between the steady-state structure in the 2-D and the 3-D case, given mixed boundary conditions; and (ii) the location of the pitchfork bifurcation point responsible for the multiple equilibria can be characterized by energy considerations alone. This characterization helps demonstrate that the physical mechanism of symmetry breaking is essentially the same in the 2-D and 3-D case.

Marotzke and Willebrand [1991] studied the global THC in an idealized configuration of the MOM model; in it, two similar ocean basins mimicked the Atlantic and Pacific Oceans. The two rectangular basins are connected at their southern end by a channel with specified transport that represents the Antarctic Circumpolar Current (ACC) and induces a prescribed north–south asymmetry. Given mixed-boundary conditions, four different types of equilibria were found: (i) a solution with northern sinking in both rectangular basins; (ii) a conveyor-belt circulation, with the THC in the “Pacific” basin

being driven by that in the “Atlantic”; (iii) an inverse-conveyor solution, with the roles of the “Pacific” and “Atlantic” interchanged; and (iv) a state with southern sinking for both ocean basins.

Weaver and Hughes [1994] used a similar MOM configuration but included a fully prognostic ACC-channel flow. Their numerical experiments were set up exactly as in Marotzke and Willebrand [1991] and three different solutions were found. For all three equilibria, the Pacific circulation is quite the same; it is only the Atlantic’s THC that is comparable to that observed, weaker or stronger. They found no northern sinking nor an inverse-conveyor solution, probably because of a more limited northward extension of their Pacific basin.

Rahmstorf [1995b] used a global version of the MOM model, with realistic continental outlines and bathymetry, to study the stability of the global THC. In his work, the circulation is driven by a prescribed freshwater flux and wind stress; instead of a prescribed surface-air temperature, a simple model of ocean–atmosphere interaction [Rahmstorf, 1995a] was used. The freshwater forcing was changed by adding slowly varying perturbations at different locations and the response of the overturning flow to these perturbations in forcing was monitored. Rahmstorf [2000] interpreted the response to a perturbation in the northern North Atlantic with an inflow of 0.05 Sv per 1000 years with the help of the diagram shown in Fig. 14. With increasing freshwater forcing, the strength of the overturning circulation decreases and at some point (indicated by S in the figure), the overturning collapses. When the freshwater input is reversed, hysteresis occurs and it takes a negative freshwater input to start the overturning again (shown by the light arrow labelled d in the figure).

Fig. 14

Manabe and Stouffer [1988] first used the coupled ocean–atmosphere model of NOAA’s Geophysical Fluid Dynamics Laboratory (GFDL) for climate studies. The global coupled model was further improved by Manabe and Stouffer [1993, 1995], who reported and analyzed long-time integrations of this model. While the spatial resolution used in the early climate studies was still quite low ($4^\circ \times 4^\circ$ degree horizontally), the model’s water mass formation and distribution was fairly realistic [England, 1992, 1993]. Those authors found two different equilibrium states; they differ considerably in the amount of northern overturning, which is about 12 Sv for one of the states, but nearly zero for the other. As expected, the two states also display a very substantial difference in surface temperature and salinity patterns, with the weak-overturning state having a smaller surface density in the North Atlantic. Tziperman [1997] showed that this coupled model has, in fact, a wide range of equilibria with weak THC; any of these equilibria may rapidly change, due to finite-amplitude perturbations, to either collapse entirely or undergo rapid oscillations.

In summary, the appearance of multiple equilibria is pervasive in models ranging from simple box-models to complex coupled ocean-atmosphere models. As we know already from Section 2, multiple equilibria are but the first step in describing and understanding the effects of nonlinearity on the ocean’s variability.

3.4.2. Temporal variability.

To understand in depth the variability of THC flows, 3-D model configurations that correspond to a single, more or less idealized basin, have been extensively analyzed using the MOM model [Marotzke, 1991; Weaver and Sarachik, 1991]. Weaver *et al.* [1993] found signatures of *decadal-to-interdecadal* variability in their simulations; its mechanism is associated with large changes in convective activity in the model’s Labrador Sea region,

which leads to changes in the meridional heat transport near the basin's western boundary [Weaver *et al.*, 1994]. This model variability is insensitive to the freshwater-flux and wind-stress forcing and seems to be caused by processes involving the surface heat flux, regional convection and the large-scale overturning circulation; the details, however, remain to be clarified.

Greatbatch and Zhang [1995] described a similar type of oscillation in an FGM; they found a slightly longer period of 50 years, vs. the 22-year periodicity found by Weaver *et al.* [1993, 1994]. Chen and Ghil [1995] analyzed in detail the physical mechanisms of variability in their 15-level MOM ocean model with rectangular-basin geometry. They showed that a robust interdecadal oscillation occurs when higher-density water is generated in high latitudes, either by cooling or by salinity increase. They emphasized that the net salt flux in the subpolar North Atlantic is positive, as brine rejection by sea-ice formation overcomes the freshening by precipitation. Huck and colleagues [Colin de Verdière and Huck, 1999; Huck *et al.*, 1999] showed that this oscillatory behavior occurs through an instability of the steady single-basin flow when the horizontal heat diffusivity is decreased. These authors attributed the propagation of the temperature anomalies to traveling baroclinic waves.

Te Raa and Dijkstra [2002] performed a systematic study of THC stability in a single basin. Two types of oscillatory modes can destabilize the steady buoyancy-driven flows in such a basin. One class of modes has an interdecadal time scale and the other has a centennial time scale; both modes are damped when restoring, rather than mixed boundary conditions are applied. Subject to prescribed surface buoyancy flux conditions, the interdecadal modes are destabilized through a Hopf bifurcation, as suggested by Chen

and Ghil's [1995] results, when the horizontal mixing of heat becomes small enough. Te Raa and Dijkstra [2002] showed that the destabilization mechanism is related to an out-of-phase response of the zonal and meridional overturning to propagating temperature anomalies (see also Colin de Verdière and Huck [1999]).

Chen and Ghil [1996] used a hybrid coupled model to clarify further whether the interdecadal climate oscillation that appears to be mainly driven by THC variability in the North Atlantic is of predominantly oceanic origin or truly involves both atmosphere and ocean as co-equal partners. As mentioned in Sec. 1.3, such models play an important role in bridging the gap between simple box and 2-D models, on the one hand, and fully coupled GCMs, on the other. The hybrid model of these authors couples a horizontally 2-D atmospheric energy-balance model (EBM) with the low-resolution ocean GCM already used by Chen and Ghil [1995] to model the North Atlantic in a simplified, rectangular geometry.

This hybrid model's regime diagram is shown in Fig. 15a. A steady state is stable for high values of the air-sea coupling parameter λ_{ao} or of the EBM's diffusion parameter d . Interdecadal oscillations with a period of 40–50 years are self-sustained and stable for low values of these two parameters. The transition from a stable equilibrium to a stable limit cycle, via Hopf bifurcation was computed by “poor-man's continuation”. The hybrid coupled model's self-sustained oscillations are characterized by a pair of vortices of opposite sign that grow and decay in quadrature with each other in the ocean's upper layers. The evolution of this pattern in SST anomalies is shown in Fig. 15b-e, where four stages of the oscillation, each 5.5 year apart, are plotted; they cover about one half of the oscillation's period, while the other half-period corresponds to an approximate inversion of

Fig. 15

the anomalies' sign. The centers of the anomalies follow each other anticlockwise through the northwestern quadrant of the model domain.

Delworth *et al.* [1993] focused on interdecadal variability within the global coupled GFDL model. Starting from a quasi-equilibrium state, determined as in Manabe and Stouffer [1988], the model was integrated for 600 'upper-ocean' years. In this model version, the 200-year mean of the overturning streamfunction attained about 18 Sv. The model variability was monitored by a THC index that equals the annual mean of the meridional overturning streamfunction's maximum value in the North Atlantic. Delworth *et al.* [1993] found pronounced variability in this THC index, with an average period of about 50 years; see Fig. 16a. The difference in annual-mean model SSTs between four decades of high THC index and four of low THC index is shown in Fig. 16b. This pattern has a dipole-like appearance, with maxima off the North American coast. It resembles the SST pattern obtained from observations [Kushnir, 1994] as the difference between relatively warm years (1970–1984) and relatively cold ones (1950–1964), which is plotted here in Fig. 16c (see also Fig. 3 of Moron *et al.* [1998]).

Fig. 16

Relations between the different atmospheric and oceanic fields and the heat and salt budgets point to the oscillation's being mainly of an oceanic origin: it appears to be driven by density anomalies in the sinking region of the subpolar North Atlantic, combined with smaller density anomalies of the opposite sign in the broad, rising region. Delworth and Greatbatch [2000] attributed this variability to a stable oscillatory THC mode, which is excited by noise in the GFDL model (see Griffies and Tziperman [1995]). Both the period and the spatio-temporal characteristics of Chen and Ghil's [1996] interdecadal oscillation are thus rather similar to those seen in Delworth *et al.*'s [1993] fully coupled

GCM with realistic geometry. They resemble, in turn, quite closely those found by Chen and Ghil [1995] in their purely oceanic, single-basin model, as well as the patterns of the interdecadal modes in the single-basin ocean models of Colin de Verdière and Huck [1999] and Te Raa and Dijkstra [2002].

The LSG model's variability was investigated by Mikolajewicz and Maier-Reimer [1990]. The model was spun up using restoring conditions on the surface salinity and temperature and momentum forcing by the annual-mean wind stress. The freshwater flux was derived from the situation after 3800 year of spin-up and the simulation was continued using mixed boundary conditions from that point on. The model's circulation is stable for this experimental set-up. Subsequently, a stochastic component was added to the freshwater flux and the response of the NADW outflow at 30°S monitored. Low-frequency variability is then present in the model and was attributed to the integration of the stochastic component in the surface forcing by the ocean [Hasselmann, 1976]. However, at a time scale of about 300 years, there is more energy in the spectrum than can be expected from pure low-pass filtering of noise. The salinity anomalies associated with this variability show a dipole pattern which is advected with the Atlantic's THC.

3.5. Relevance to the North Atlantic and global THC

We compare here the results from bifurcation studies of 2-D and 3-D models of the oceans' THC with those of more traditional GCM studies. The phenomenon of multiple equilibria found in GCMs appears to be either related to equatorial symmetry breaking or to saddle-node bifurcations.

The equatorially symmetric set-up is the clearest case: the emergence of asymmetric pole-to-pole solutions is due to symmetry breaking, which occurs across the entire hier-

archy of models [Rooth, 1982; Bryan, 1986; Welander, 1986; Quon and Ghil, 1992; Thual and McWilliams, 1992; Weijer and Dijkstra, 2001]. The associated physical mechanism is the salt-advection feedback; this mechanism only requires that there exist a meridional velocity response to a change in the meridional density profile, given a strong enough meridional salinity gradient. Imperfections of the equatorially symmetric situation, due to either asymmetric freshwater forcing or continental asymmetry, lead to disconnected branches of equilibria. These asymmetries may explain the multiple equilibria, or lack thereof, in more realistic situations [Weijer *et al.*, 1999; Dijkstra and Neelin, 2000].

Ganopolsky *et al.* [2001] carried out climate model simulations in which the ocean circulation is represented by a zonally averaged flow in each basin, in order to examine the mechanism of Dansgaard-Oeschger cycles. In their model, two stable steady states exist for the modern climate — one with high, the other with nearly zero meridional overturning — while in the glacial climate there is only one stable circulation pattern. A time-dependent variation in the freshwater flux forcing can, however, induce rapid transitions between this cold state and an unstable warm state. Hence, the loss of stability of the THC equilibrium, combined with variable surface fluxes, can lead to oscillations that resemble Dansgaard-Oeschger cycles.

Overturning mean flows in the oceans seem to be subject to several modes of oscillatory instability; see Table 4. These range from relaxation oscillations — characterized by millennial periodicities with long intervals of weak THC that alternate with sudden flushes — through centennial oscillations, which correspond to the loop advection of density anomalies, all the way to decadal and interdecadal oscillations. It is the latter that are of the greatest interest in distinguishing natural from anthropogenic variability on

Table 4

the time scale of human life [Martinson *et al.*, 1995; Ghil, 2001]. What role, if any, do the interdecadal oscillatory modes described in this section play in the ocean's observed interdecadal variability?

A similar question was discussed, with respect to the wind-driven circulation and interannual variability, in Section 2.6. The answer, again, can only be given by studying the spatio-temporal patterns and physical mechanisms of these interdecadal modes across a hierarchy of models and the various, albeit incomplete, observational data sets [Ghil and Robertson, 2000; Ghil, 2001]. Evidence is mounting that the 14–15 year and 25–27-year peaks in temperature spectra (see Ghil and Vautard [1991] and Fig. 1b here) are indeed due to THC modes, as conjectured in Plaut *et al.* [1995]. This evidence includes the similarity between the interdecadal mode of Chen and Ghil's [1996] simplified hybrid coupled model and that of Delworth *et al.*'s [1993] fully coupled global GCM, as well as that between the latter and the observational results of Kushnir [1994] and Moron *et al.* [1998].

It does not matter in this context whether these THC modes are due to damped or self-sustained instabilities, since the modes can always be excited by stochastic noise [Griffies and Tziperman, 1995; Rivin and Tziperman, 1997]. The forcing of the ocean by atmospheric variability has a wide range of time scales. High-frequency forcing may lead to low-frequency response in the coupled system, according to the scenario of Hasselmann [1976] and Mitchell [1976], while low-frequency forcing can lead to direct changes in the ocean circulation. The latter may be resonantly amplified by the presence of an oscillatory instability, even if this mode is damped, in the absence of atmospheric “noise.” Moreover, coupled modes of variability may also exist, where feedbacks between the ocean and

atmosphere act in concert to amplify perturbations [Latif and Barnett, 1994, 1996]. The ocean's interactions with sea ice may contribute to even richer types of variability [Yang and Neelin, 1993; Kravtsov and Ghil, 2004].

It thus appears that an understanding of elementary bifurcations does help explain the changes in the oceans' THC, on time scales of decades and longer. The results are, however, less conclusive than those in Section 2.

4. OUTLOOK

Until about two decades ago, the tools of analytical and numerical bifurcation theory could be applied only to 0-D THC models [Stommel, 1961; Rooth, 1982] or to 0-D and 1-D climate models [Held and Suarez, 1974; Ghil, 1976; North *et al.*, 1981]. We have illustrated in this review, by considering a few oceanic flow problems on different time scales, that the general theory can be combined with powerful numerical tools to study successive bifurcations across the hierarchy of climate models, all the way from 0-D global or box models (see above) to 2-D and 3-D models: atmospheric [Legras and Ghil, 1985; Strong *et al.*, 1995], oceanic [Quon and Ghil, 1992, 1995; Thual and McWilliams, 1992; Dijkstra and Molemaker, 1997], and coupled [Chen and Ghil, 1996; Te Raa and Dijkstra, 2003].

Each bifurcation is associated with a specific linear instability of a relatively simple climate state — oscillatory in the case of Hopf bifurcations and purely exponential in the case of saddle-node or pitchfork bifurcations. The nonlinear saturation of each instability leads to more complicated spatio-temporal patterns. Following the bifurcation tree, from one rung of the modeling hierarchy to the next, permits us, therefore, to study with

increasing detail and realism the basic physical mechanisms that lead to low-frequency variability of the ocean circulation.

Typically, the first one or two bifurcations will be captured fairly well by a lower-order or otherwise very simple model of the ocean circulation problem of interest. As the model's number of degrees of freedom or other aspects of its complexity increase, more complicated and realistic regimes of behavior will appear. These regimes can be reached by studying the additional bifurcations that intervene. The task of following bifurcations numerically off solution branches with greater and greater complexity becomes more and more challenging. Continuation methods [Keller, 1977; Seydel, 1994; Doedel and Tuckermann, 2000] are now applied to follow steady-state and periodic solution branches of more and more highly resolved atmospheric [Legras and Ghil, 1985; Strong *et al.*, 1995; Keppene *et al.*, 2000], 2-D oceanic [Speich *et al.*, 1995; Dijkstra and Molemaker, 1997; Simonnet *et al.*, 2003a, b], and 3-D oceanic [Te Raa and Dijkstra, 2002] models. Projected increase of computer power and developments in numerical algorithms should make it possible to apply such methods to currently available GCMs in the near future.

Results from GCMs — atmospheric, oceanic, and coupled — provide solutions to ocean circulation and climate dynamical problems that have the greatest spatio-temporal detail and, one hopes, the greatest degree of physical realism. These solutions provide, in turn, the best opportunity for evaluating our theories of low-frequency variability of the ocean circulation, developed by climbing the lower rungs of the modeling hierarchy, against the observational evidence, to the extent that the latter is available.

Such an evaluation, given the irregular character of the observed oceanic variability, needs to be informed by the ergodic theory of dynamical systems [Eckmann and Ruelle,

1985], which can describe this irregular behavior in a consistent way. The basic ideas of the latter theory have led, in the climate context, to the development of advanced statistical tools, such as clustering methods [Ghil and Robertson, 2002], as well as singular-spectrum analysis [Ghil and Vautard, 1991; Plaut and Vautard, 1994] and other advanced spectral methods [Ghil *et al.*, 2002a]. These tools have to be applied in parallel to the GCMs' simulations and to the relevant observational data sets.

Studying the observed and simulated ocean variability with the same sophisticated tools can help pinpoint the aspects of this variability that we have understood, and can therefore predict with confidence, and those that we have not. Fortunately, there are many more of the latter, and much work remains to be done. It is the authors' hope that the tools and points of view presented here will help to solve certain ocean-related climate-variability problems, as well as possibly suggest some new ones.

ACKNOWLEDGMENTS.

It is a pleasure to thank many colleagues who shared ideas and preprints with us. We are grateful to all our associates who worked with us on the low-frequency variability of the oceans: Y. Chao, K.-I. Chang, S. Drijfhout, S. Jiang, F.-F. Jin, F. Chen, Y. Feliks, K. Ide, M. Karaca, C. Katsman, C.-C. Lai, H. Le Treut, G. Loeper, J.C. McWilliams, M. J. Molemaker, J. Nauw, J. D. Neelin, H. Öksüzöglu, D. Paillard, Z. Pan, C. Quon, L. te Raa, W. de Ruijter, M. Schmeits, E. Simonnet, L. U. Sushama, R. Temam, P. van der Vaart, S. Wang, W. Weijer, A. Wirth, and F. W. Wubs. The paper benefited from careful reading and many constructive comments by P. DeMenocal, E. Tziperman and several anonymous reviewers. This work was supported by the Netherlands Organization for Scientific Research (NWO) under a NWO-PIONIER grant (HD) and by NSF grants ATM00-83121 and OCE02-221066 and DOE grant DE-FG02-01ER63251 (MG).

REFERENCES

- Arakawa, A. and Lamb, V. R. (1977). Computaional design of basic dynamical processes of the UCLA general circulation model. *Methods Comput. Phys.*, **17**, 173–265.
- Auer, S. J. (1987). Five-year climatological survey of the Gulf Stream system and its associated rings. *J. Geophys. Res.*, **92**, 11,709 – 11,726.
- Bane, J. M. and Dewar, W. K. (1988). Gulf Stream bimodality and variability downstream of the Charleston Bump. *J. Geophys. Res.*, **93**, 6695–6710.
- Barenblatt, G. L. (1987). *Dimensional Analysis*. Gordon and Breach, New York.
- Beckmann, A. C. W., Böning, C. W., Köberle, J., and Willebrand, J. (1994). Effects of increased horizontal resolution in a simulation of the North-Atlantic ocean. *J. Phys. Oceanogr.*, **24**, 326–344.
- Berloff, P. S. and McWilliams, J. C. (1999). Large-scale, low-frequency variability in wind-driven ocean gyres. *J. Phys. Oceanogr.*, **29**, 1925–1949.
- Berloff, P. S. and Meacham, S. P. (1997). The dynamics of an equivalent barotropic model of the wind-driven circulation. *J. Mar. Res.*, **55**, 407–451.
- Berloff, P. S. and Meacham, S. P. (1998). On the stability of the wind-driven circulation. *J. Mar. Res.*, **56**, 937–993.
- Bjerknes, J. P. (1969). Atmospheric teleconnections from the equatorial Pacific. *Monthly Weather Review*, **97**, 163–172.
- Boiseau, M., Ghil, M., and Juillet-Leclerc, A. (1999). Trends and interdecadal variability from South-Central Pacific coral records. *Geophys. Res. Lett.*, **26**, 2881–2884.
- Bond, G., Showers, W., Cheseby, M., Lotti, R., Almasi, P., deMenocal, P., Priori, P., Cullen, H., Hajdas, I., and Bonani, G. (1995). A pervasive millennial-scale cycle in the

North Atlantic Holocene and glacial climates. *Science*, **278**, 1257–1265.

Bradley, R. S. (1999). *Paleoclimatology: Reconstructing Climates of the Quaternary*.

Academic Press, New York, U.S.A.

Broecker, W. S. (1991). The great ocean conveyor. *Oceanography*, **4**, 79–89.

Broecker, W. S. and Van Donk, J. (1970). Insolation changes, ice volumes, and the $\delta^{18}O$ record in deep-sea cores. *Rev. Geophys. Space Phys.*, **8**, 169197.

Broecker, W. S., Peteet, D. M., and Rind, D. (1985). Does the ocean-atmosphere system have more than one stable mode of operation? *Nature*, **315**, 21–26.

Brugge, B. (1995). Near surface mean circulation and eddy kinetic energy in the central North Atlantic from drifter data. *J. Geophys. Res.*, **100**, 20,54320,554.

Bryan, F. O. (1986). High-latitude salinity effects and interhemispheric thermohaline circulations. *Nature*, **323**, 301–304.

Bryan, F. O., Böning, C. W., and Holland, W. R. (1995). On the midlatitude circulation in a high-resolution model of the North Atlantic. *J. Phys. Oceanogr.*, **25**, 289–305.

Bryan, K., Manabe, S., and Pacanowski, R. C. (1974). A global ocean-atmosphere climate model. Part II. The oceanic circulation. *J. Phys. Oceanogr.*, **5**, 30–46.

Bryden, H. L., Roemmich, D., and Church, J. (1991). Heat transport across 24°N in the Pacific. *Deep-Sea Research*, **38**, 297–324.

Bryden, H. L., Griffiths, M. J., Lavin, A. M., Millard, R. C., Parilla, G., and Smethie, W. M. (1996). Decadal changes in water mass characteristics at 24°N in the subtropical North Atlantic Ocean. *J. Climate*, **9**, 3162–3186.

Cane, M. A. and Zebiak, S. E. (1985). A theory for El Niño and the Southern Oscillation. *Science*, **228**, 1084–1087.

- Cessi, P. and Ierley, G. R. (1995). Symmetry-breaking multiple equilibria in quasi-geostrophic, wind-driven flows. *J. Phys. Oceanogr.*, **25**, 1196–1205.
- Cessi, P. and Young, W. R. (1992). Multiple equilibria in two-dimensional thermohaline circulation. *J. Fluid Mech.*, **241**, 291–309.
- Chang, K.-I., Ghil, M., Ide, K., and Lai, C.-C. A. (2001). Transition to aperiodic variability in a wind-driven double-gyre circulation model. *J. Phys. Oceanogr.*, **31**, 1260–1286.
- Chao, Y., Gangopadhyay, A., Bryan, F. O., and Holland, W. R. (1996). Modeling the Gulf Stream system: How far from reality? *Geophys. Res. Letters*, **23**, 3155–3158.
- Charney, J. and DeVore, J. (1979). Multiple flow equilibria in the atmosphere and blocking. *J. Atmos. Sci.*, **36**, 1205–1216.
- Chassignet, E. P. and Bleck, R. (1993). The influence of layer outcropping on the separation of boundary currents. Part I: The wind-driven experiments. *J. Phys. Oceanogr.*, **23**, 1485–1507.
- Chassignet, E. P., Arango, H., Dietrich, D., Ezer, T., Ghil, M., Haidvogel, D. B., Ma, C.-C., Mehra, A., Paiva, A. M., and Sirkes, Z. (2000). DAMEE-NAB: The base experiments. *Dyn. Atmos. Oceans*, **32**, 155–183.
- Chelton, D. B. and Schlax, M. (1996). Global observations of oceanic Rossby waves. *Science*, **272**, 234–238.
- Chen, F. and Ghil, M. (1995). Interdecadal variability of the thermohaline circulation and high-latitude surface fluxes. *J. Phys. Oceanogr.*, **22**, 161–167.
- Chen, F. and Ghil, M. (1996). Interdecadal variability in a hybrid coupled ocean-atmosphere model. *J. Phys. Oceanogr.*, **26**, 1561–1578.
- Colin de Verdière, A. (1988). Buoyancy driven planetary flows. *J. Mar. Res.*, **46**, 215–265.

Colin de Verdière, A. and Huck, T. (1999). Baroclinic instability: an oceanic wavemaker for interdecadal variability. *J. Phys. Oceanogr.*, **29**, 893–910.

Cox, M. (1984). A primitive equation, three-dimensional model of the ocean. Technical Report 1, GFDL Ocean Group.

Cox, M. (1987). An eddy-resolving model of the ventilated thermocline: time-dependence. *J. Phys. Oceanogr.*, **17**, 1044–1056.

Da Costa, E. D. and Colin de Verdière, A. C. (2004). The 7.7 year North Atlantic oscillation. *Quart. J. Roy. Meteor. Soc.*, **128**.

Daley, R. (1991). *Atmospheric Data Analysis*. Cambridge Univ. Press.

Delworth, T. L. and Greatbatch, R. G. (2000). Multidecadal thermohaline circulation variability driven by atmospheric surface flux forcing. *J. Climate*, **13**, 1481–1495.

Delworth, T. L. and Mann, M. E. (2000). Observed and simulated multidecadal variability in the Northern Hemisphere. *Clim. Dyn.*, **16**, 661–676.

Delworth, T. L., Manabe, S., and Stouffer, R. J. (1993). Interdecadal variations of the thermohaline circulation in a coupled ocean-atmosphere model. *J. Climate*, **6**, 1993–2011.

Dengg, J., Beckmann, A., and Gerdes, R. (1996). The Gulf Stream separation problem. In W. A. Kraus, editor, *The Warmwatersphere of the North Atlantic Ocean*, pages 253–290. Borntraeger.

Deser, C. and Blackmon, M. L. (1993). Surface climate variations over the North Atlantic ocean during winter: 1900–1989. *J. Climate*, **6**, 1743–1753.

Dickson, R. and Brown, J. (1994). The production of North Atlantic Deep Water. *J. Geophys. Res.*, **99**, 12,319–12,341.

- Dickson, R. R., Meincke, J., Malmberg, S., and Lee, A. (1988). The “Great Salinity Anomaly” in the northern North Atlantic 1968-1982. *Prog. Oceanogr.*, **20**, 103–151.
- Dijkstra, H. A. (2000). *Nonlinear Physical Oceanography: A Dynamical Systems Approach to the Large Scale Ocean Circulation and El Niño*. Kluwer Academic Publishers, Dordrecht, the Netherlands.
- Dijkstra, H. A. and Burgers, G. (2002). Fluid Mechanics of El Niño variability. *Annual Review of Fluid Mechanics*, **34**, 531–558.
- Dijkstra, H. A. and Katsman, C. A. (1997). Temporal variability of the wind-driven quasi-geostrophic double gyre ocean circulation: Basic bifurcation diagrams. *Geophys. Astrophys. Fluid Dyn.*, **85**, 195–232.
- Dijkstra, H. A. and Molemaker, M. J. (1997). Symmetry breaking and overturning oscillations in thermohaline-driven flows. *J. Fluid Mech.*, **331**, 195–232.
- Dijkstra, H. A. and Molemaker, M. J. (1999). Imperfections of the North-Atlantic wind-driven ocean circulation: Continental geometry and wind stress shape. *J. Mar. Res.*, **57**, 1–28.
- Dijkstra, H. A. and Neelin, J. D. (1999). Imperfections of the thermohaline circulation: Multiple equilibria and flux-correction. *J. Climate*, **12**, 1382–1392.
- Dijkstra, H. A. and Neelin, J. D. (2000). Imperfections of the thermohaline circulation: Latitudinal asymmetry versus asymmetric freshwater flux. *J. Climate*, **13**, 366–382.
- Dijkstra, H. A., Öksüzöglu, H., Wubs, F. W., and Botta, E. F. F. (2001). A fully implicit model of the three-dimensional thermohaline ocean circulation. *J. Comput. Phys.*, **173**, 685–715.

- Doedel, E. J. and Tuckermann, L. S. (2000). *Numerical Methods for Bifurcation Problems and Large-Scale Dynamical Systems*. Springer-Verlag, New York.
- Dommenget, D. and Latif, M. (2000). Interannual to decadal variability in the Tropical Atlantic. *J. Climate*, **13**, 777–792.
- Duplessy, J.-C. and Shackleton, N. J. (1985). Response of global deep-water circulation to earth's climatic change 135,000-107,000 years ago. *Nature*, **316**, 500–507.
- Eady, E. T. (1949). Long waves and cyclone waves. *Tellus*, **1**, 33–52.
- Eckmann, J. P. and Ruelle, D. (1985). Ergodic theory of chaos and strange attractors. *Rev. Mod. Phys.*, **57**, 617–656.
- England, M. H. (1992). On the formation of Antarctic intermediate and bottom water in ocean general circulation models. *J. Phys. Oceanogr.*, **22**, 918–926.
- England, M. H. (1993). Representing the global-scale water masses in ocean general circulations models. *J. Phys. Oceanogr.*, **23**, 1523–1552.
- Feliks, Y. and Ghil, M. (1996). Mixed barotropic-baroclinic eddies growing on an eastward midlatitude jet. *Geophys. Astrophys. Fluid Dyn.*, **82**, 137–171.
- Flierl, G. (1978). Models of vertical structure and calibration of two-layer models. *Dyn. Atmos. Oceans*, **2**, 341–381.
- Frankignoul, C. and Hasselmann, K. (1977). Stochastic climate models. II: Application to sea-surface temperature anomalies and thermocline variability. *Tellus*, **29**, 289–305.
- Fu, L.-L. and Cheney, R. E. (1995). Application of satellite altimetry to ocean circulation studies: 1987–1994. *Rev. Geophysics*, **33**.
- Fu, L.-L. and Smith, R. D. (1996). Global ocean circulation from satellite altimetry and high-resolution computer simulation. *Bull. Amer. Meteorol. Soc.*, **77**, 2625–2636.

- Ganachaud, A. and Wunsch, C. (2000). Improved estimates of global ocean circulation, heat transport and mixing from hydrographic data. *Nature*, **408**, 453–457.
- Gangopadhyay, A., Cornillon, P., and Watts, D. (1992). A test of the Parsons-Veronis hypothesis on the separation of the Gulf Stream. *J. Phys. Oceanogr.*, **22**, 1286–1301.
- Ganopolsky, A., Rahmstorf, S., Petoukhov, V., and Claussen, M. (2001). Rapid changes of glacial climate simulated in a coupled climate model. *Nature*, **409**, 153–158.
- Gaspar, P. and Wunsch, C. (1989). Estimates from altimeter data of barotropic Rossby waves in the northwestern Atlantic Ocean. *J. Phys. Oceanogr.*, **19**, 1821–1844.
- Gerdes, R. and Köberle, C. (1995). On the influence of DSOW in a numerical model of the North Atlantic general circulation. *J. Phys. Oceanogr.*, **25**, 2624–2642.
- Ghil, M. (1976). Climate stability for a Sellers-type model. *J. Atmos. Sci.*, **33**, 3–20.
- Ghil, M. (2001). Hilbert problems for the geosciences in the 21st century. *Nonlin. Proc. Geophys.*, **8**, 211222.
- Ghil, M. (2002). Natural climate variability. In T. E. Munn, M. MacCracken, and J. Perry, editors, *Encyclopedia of Global Environmental Change, Vol. 1*, pages 544–549. J. Wiley and Sons, Chichester/New York.
- Ghil, M. and Childress, S. (1987). *Topics in Geophysical Fluid Dynamics: Atmospheric Dynamics, Dynamo Theory, and Climate Dynamics*. Springer-Verlag, Berlin/Heidelberg/New York.
- Ghil, M. and Malanotte-Rizzoli, P. (1991). Data assimilation in meteorology and oceanography. *Adv. Geophys.*, **33**, 141–266.
- Ghil, M. and Robertson, A. W. (2000). Solving problems with GCMs: General circulation models and their role in the climate modeling hierarchy. In D. A. Randall, editor,

General Circulation Model Development: Past, Present and Future, pages 285–325.

Academic Press, New York.

Ghil, M. and Robertson, A. W. (2002). "Waves" vs. "particles" in the atmosphere's phase space: A pathway to long-range forecasting? *Proc. Natl. Acad. Sci.*, **99**, (Suppl. 1), 2493–2500.

Ghil, M. and Vautard, R. (1991). Interdecadal oscillations and the warming trend in global temperature time series. *Nature*, **350**, 324–327.

Ghil, M., Kimoto, M., and Neelin, J. D. (1991). Nonlinear dynamics and predictability in the atmospheric sciences. *Rev. Geophys., Supplement (U.S. Nat'l Rept. to Int'l Union of Geodesy and Geophys. 1987–1990)*, **29**, 4655.

Ghil, M., Ide, K., Bennett, A. F., Courtier, P., Kimoto, M., and Sato, N. E. (1997). *Data Assimilation in Meteorology and Oceanography: Theory and Practice*. Meteorological Society of Japan and Universal Academy Press, Tokyo, Japan.

Ghil, M., Allen, M. R., Dettinger, M. D., Ide, K., Kondrashov, D., Mann, M. E., Robertson, A. W., Saunders, A., Tian, Y., Varadi, F., and Yiou, P. (2002a). Advanced spectral methods for climatic time series. *Rev. Geophys.*, **40**, 3.1–3.41. 10.1029/2000GR000092.

Ghil, M., Feliks, Y., and Sushama, L. (2002b). Baroclinic and barotropic aspects of the wind-driven ocean circulation. *Physica D*. in press.

Ghil, M., Liu, J.-G., Wang, C., and Wang, S. (2004). Boundary-layer separation and adverse pressure gradient for 2-D viscous incompressible flow. *Physica D*, **197**, 149–173.

Gildor, H. and Tziperman, E. (2001). A sea ice climate switch mechanism for the 100-kyr glacial cycles. *J. Geophys. Res.*, **106**, 9117–9133.

- Gill, A. E. (1982). *Atmosphere-Ocean Dynamics*. Academic Press, New York, U.S.A.
- Gordon, A. L. (1986). Interocean exchange of thermocline water. *J. Geophys. Res.*, **91**, 5037–5046.
- Greatbatch, R. J. and Zhang, S. (1995). An interdecadal oscillation in an idealized ocean basin forced by constant heat flux. *J. Climate*, **8**, 82–91.
- Griffies, S. M. and Tziperman, E. (1995). A linear thermohaline oscillator driven by stochastic atmospheric forcing. *J. Climate*, **8**, 2440–2453.
- Guckenheimer, J. and Holmes, P. (1990). *Nonlinear Oscillations, Dynamical Systems and Bifurcations of Vector Fields, 2e edition*. Springer-Verlag, Berlin/Heidelberg.
- Haidvogel, D. B., McWilliams, J. C., and Gent, P. R. (1992). Boundary current separation in a quasi-geostrophic eddy-resolving ocean circulation model. *J. Phys. Oceanogr.*, **22**, 882–902.
- Haines, K. (1994). Low-frequency variability in atmospheric middle latitudes. *Surveys in Geophysics*, **15**, 1.
- Hall, M. and Bryden, H. (1982). Direct estimates of ocean heat transport. *Deep-Sea Research*, **29**, 339–359.
- Haney, R. L. (1971). Surface thermal boundary conditions for ocean circulation models. *J. Phys. Oceanogr.*, **4**, 241–248.
- Hasselmann, K. (1976). Stochastic climate models. I: Theory. *Tellus*, **28**, 473–485.
- Hasselmann, K. (1982). An ocean model for climate variability studies. *Progress in Oceanography*, **11**, 69–92.
- Hays, J. D., Imbrie, J., and Shackleton, N. J. (1976). Variations in the Earth's orbit: Pacemaker of the ice ages. *Science*, **194**, 1121.

- Heinrich, H. (1988). Origin and Consequences of Cyclic Ice Rafting in the Northeast Atlantic Ocean during the Past 130,000 Years. *Quaternary Research*, **29**, 142–152.
- Held, I. M. (2001). The partitioning of the poleward energy transport between the tropical ocean and atmosphere. *J. Atmos. Sci.*, **58**, 943–948.
- Held, I. M. and Suarez, M. J. (1974). Simple albedo feedback models of the ice caps. *Tellus*, **26**, 613–629.
- Hogg, N. G., Pickart, R. S., Hendry, R. M., and Smethie, W. J. (1986). The northern recirculation gyre of the Gulf Stream. *Deep-Sea Research*, **33**, 1139–1165.
- Holland, W. R. and Bryan, F. O. (1994). Modelling the wind and thermohaline circulation in the North-Atlantic Ocean. In P. Malanotte-Rizzoli and A. Robinson, editors, *Ocean Processes in Climate Dynamics: Global and Mediterranean Examples*, pages 35–156. Kluwer Academic, Netherlands.
- Holzer, M. and Hall, T. M. (2000). Transit-time and tracer-age distributions in geophysical flows. *J. Atmos. Sci.*, **57**, 3539–3558.
- Huang, R. (1993). Real freshwater fluxes as a natural boundary condition for the salinity balance and thermohaline circulation forced by evaporation and precipitation. *J. Phys. Oceanogr.*, **23**, 2428–2446.
- Huang, R. X., Luyten, J. R., and Stommel, H. M. (1992). Multiple equilibrium states in combined thermal and saline circulation. *J. Phys. Oceanogr.*, **22**, 231–246.
- Huck, T., Colin de Verdière, A., and Weaver, A. J. (1999). Interdecadal Variability of the Thermohaline Circulation in Box-Ocean Models Forced by Fixed Surface Fluxes. *J. Phys. Oceanogr.*, **29**, 865892.

- Ichikawa, H. and Beardsley, R. C. (1993). Temporal and spatial variability of volume transport of the Kuroshio in the East China Sea. *Deep-Sea Research*, **40**, 583–605.
- Ierley, G. R. and Sheremet, V. A. (1995). Multiple solutions and advection-dominated flows in the wind-driven circulation. I: Slip. *J. Mar. Res.*, **53**, 703–737.
- Imbrie, J. and Imbrie, K. P. (1986). *Ice Ages: Solving the Mystery*. 2nd Edn., Harvard Univ. Press, Cambridge, Mass.
- Jiang, S., Jin, F.-F., and Ghil, M. (1993). The nonlinear behavior of western boundary currents in a wind-driven, double-gyre, shallow-water model. In *Ninth Conf. Atmos. and Oceanic Waves and Stability (San Antonio, TX)*, pages 64–67, Boston, Mass. American Meteorological Society.
- Jiang, S., Jin, F.-F., and Ghil, M. (1995). Multiple equilibria and aperiodic solutions in a wind-driven double-gyre, shallow-water model. *J. Phys. Oceanogr.*, **25**, 764–786.
- Johns, W. E., Shay, T. J., Bane, J. M., and Watts, D. R. (1995). Gulf Stream structure, transport and recirculation near 68°W. *J. Geophys. Res.*, **100**, 817–838.
- Jouzel, J., Barkov, N. I., Barnola, J. M., Bender, M., Chappellaz, J., Genthon, C., Kotlyakov, V. M., Lipenkov, V., Lorius, C., Petit, J. R., Raynaud, D., Raisbeck, G., Ritz, C., Sowers, T., Stievenard, M., Yiou, F., and Yiou, P. (1991). Extending the Vostok ice-core record of paleoclimate to the penultimate glacial period. *Nature*, **364**, 407–412.
- Joyce, T. M. and Robbins, P. (1995). The long-term hydrographic record at Bermuda. *J. Climate*, **9**, 3122–3131.
- Kamenkovich, V. M., Sheremet, V. A., Pastushkov, A. R., and Belotserkovsky, S. O. (1995). Analysis of barotropic model of the subtropical gyre in the ocean for finite

Reynolds number. *J. Mar. Res.*, **53**, 959–994.

Karaca, M. and Müller, D. (1989). Simulation of sea surface temperatures with surface heat fluxes from an atmospheric circulation model. *Tellus*, **41A**, 32–47.

Karaca, M., Wirth, A., and Ghil, M. (1999). A box model for the paleoceanography of the Black Sea. *Geophys. Res. Letters*, **26**, 497–500.

Keir, R. S. (1988). On the late Pleistocene ocean geochemistry and circulation. *Paleoceanography*, **3**, 413–446.

Keller, H. B. (1977). Numerical solution of bifurcation and nonlinear eigenvalue problems. In P. H. Rabinowitz, editor, *Applications of Bifurcation Theory*. Academic Press, New York, U.S.A.

Keppene, C., Markus, S., Kimoto, M., and Ghil, M. (2000). Intraseasonal variability in a two-layer model and observations. *J. Atmos. Sci.*, **57**, 1010–1028.

Klinger, B. A. and Marotzke, J. (1999). Behavior of double-hemispheric thermohaline flows in a single basin. *J. Phys. Oceanogr.*, **29**, 382–399.

Kraus, E. and Turner, J. S. (1967). A one-dimensional model of the seasonal thermocline. *Tellus*, **19**, 98–105.

Kravtsov, S. and Ghil, M. (2004). Interdecadal variability in a hybrid coupled ocean-atmosphere-sea-ice model. *J. Phys. Oceanogr.* accepted.

Kushnir, Y. (1994). Interdecadal variations in North Atlantic sea surface temperature and associated atmospheric conditions. *J. Phys. Oceanogr.*, **7**, 141–157.

Latif, M. and Barnett, T. P. (1994). Causes of decadal climate variability over the North Pacific and North America. *Science*, **266**, 634–637.

- Latif, M. and Barnett, T. P. (1996). Decadal climate variability over the north pacific and north america: Dynamics and predictability. *J. Climate*, **9**, 2407-2423.
- Le Traon, P. Y., Nadal, F., and Ducet, N. (1998). An improved mapping method of multi-satellite altimeter data. *J. Atmos. Oceanic Technol.*, **15**, 522-534.
- LeBlond, P. H. and Mysak, L. A. (1978). *Waves in the Ocean*. Elsevier, Amsterdam, 602 pp.
- Lee, D. and Cornillon, P. (1995). Temporal variation of meandering intensity and domain-wide lateral oscillations of the Gulf Stream. *J. Geophys. Res.*, **100**, 13,603-13,613.
- Legras, B. and Ghil, M. (1985). Persistent anomalies, blocking, and variations in atmospheric predictability. *J. Atmos. Sci.*, **42**, 433-471.
- Lenderink, G. and Haarsma, H. (1994). Variability and multiple equilibria of the thermohaline circulation associated with deep-water formation. *J. Phys. Oceanogr.*, **24**, 1480-1493.
- Levitus, S., Antonov, J., Boyer, T., and Stephens, C. (2000). Warming of the world ocean. *Science*, **287**, 2225-2229.
- Lorenz, E. N. (1963a). Deterministic nonperiodic flow. *J. Atmos. Sci.*, **20**, 130-141.
- Lorenz, E. N. (1963b). The mechanics of vacillation. *J. Atmos. Sci.*, **20**, 448-464.
- MacDonald, A. M. and Wunsch, C. (1996). An estimate of global ocean circulation and heat fluxes. *Nature*, **382**, 436-439.
- Maier-Reimer, E., Mikolajewicz, U., and Hasselman, K. (1993). Mean circulation of the Hamburg LSG OGCM and its sensitivity to the thermohaline surface forcing. *J. Phys. Oceanogr.*, **23**, 731-757.

- Manabe, S. and Stouffer, R. J. (1988). Two stable equilibria of a coupled ocean-atmosphere model. *J. Climate*, **1**, 841–866.
- Manabe, S. and Stouffer, R. J. (1993). Century-scale effects of increased CO₂ on the ocean-atmosphere system. *Nature*, **364**, 215–220.
- Manabe, S. and Stouffer, R. J. (1995). Simulation of abrupt climate change induced by freshwater input into the North Atlantic Ocean. *Nature*, **378**, 165–167.
- Mann, M. E., Bradley, R. S., and Hughes, M. K. (1998). Global-scale temperature patterns and climate forcing over the past six centuries. *Nature*, **392**, 779–787.
- Marotzke, J. (1991). Influence of convective adjustment on the stability of the thermohaline circulation. *J. Phys. Oceanogr.*, **21**, 903–907.
- Marotzke, J. and Willebrand, P. (1991). Multiple equilibria of the global thermohaline circulation. *J. Phys. Oceanogr.*, **21**, 1372–1385.
- Marotzke, J., Welander, P., and Willebrand, J. (1988). Instability and multiple steady states in a meridional-plane model of thermohaline circulation. *Tellus*, **40**, 162–172.
- Martinson, D. G., Bryan, K., Ghil, M., Hall, M. M., Karl, T. R., Sarachik, E. S., Sorooshian, S., and Talley, L. D. (1995). *Natural Climate Variability on Decade-to-Century Time Scales*. National Academy Press, Washington, DC, U.S.A.
- McCalpin, J. D. and Haidvogel, D. B. (1996). Phenomenology of the low-frequency variability in a reduced gravity quasi-geostrophic double-gyre model. *J. Phys. Oceanogr.*, **26**, 739–752.
- McWilliams, J. C. (1996). Modeling the ocean general circulation. *Ann. Rev. Fluid Mechanics*, **28**, 215–248.

- Meacham, S. P. (2000). Low frequency variability of the wind-driven circulation. *J. Phys. Oceanogr.*, **30**, 269–293.
- Mikolajewicz, U. and Maier-Reimer, E. (1990). Internal secular variability in an ocean general circulation model. *Clim. Dyn.*, **4**, 145–156.
- Mitchell, J. M. (1976). An overview of climate variability and its causal mechanisms. *Quatern. Res.*, **6**, 481–493.
- Mizuno, S. and White, W. B. (1993). Annual and interannual variability in the Kuroshio Current System. *J. Phys. Oceanogr.*, **13**, 1847–1867.
- Molteni, F. M. (2002). Weather regimes and multiple equilibria. In J. R. Holton, editor, *Encyclopedia of Atmospheric Sciences*, pages 2577–2586. Academic Press.
- Moron, V., Vautard, R., and Ghil, M. (1998). Trends, interdecadal and interannual oscillations in global sea-surface temperature. *Clim. Dyn.*, **14**, 545–569.
- Munk, W. (1950). On the wind-driven ocean circulation. *J. Meteorol.*, **7**, 79–93.
- Nadiga, B. T. and Luce, B. (2001). Global bifurcation of Shilnikov type in a double-gyre model. *J. Phys. Oceanogr.*, **31**, 2669–2690.
- Neelin, J. D., Latif, M., and Jin, F.-F. (1994). Dynamics of coupled ocean-atmosphere models: The tropical problem. *Ann. Rev. Fluid Mech.*, **26**, 617–659.
- Neelin, J. D., Battisti, D. S., Hirst, A. C., Jin, F.-F., Wakata, Y., Yamagata, T., and Zebiak, S. E. (1998). ENSO Theory. *J. Geophys. Res.*, **103**, 14,261–14,290.
- New, A. L., Bleck, R., Jia, Y., Marsh, M., Huddleston, M., and Barnard, S. (1995). An isopycnic model study of the North Atlantic. I: Model experiment and water mass formation. *J. Phys. Oceanogr.*, **25**, 2667–2699.

- Niiler, P. P. and Richardson, W. S. (1973). Seasonal variability of the Florida Current. *J. Mar. Res.*, **31**, 144–167.
- North, G. (1975). Analytical solution to a simple climate model with diffusive heat transport. *J. Atmos. Sci.*, **32**, 1301–1307.
- North, G. R., Cahalan, R. F., and Coakley, J. A. (1981). Energy balance climate models. *Rev. Geophys. Space Phys.*, **19**, 19–121.
- North, G. R., Mengel, J. G., and Short, D. A. (1983). Simple energy-balance model resolving the seasons and the continents – application to the astronomical theory of the ice ages. *J. Geophys. Res.*, **88**, 6576–6586.
- Oberhuber, J. M. (1988). *The Budget of Heat, Buoyancy and Turbulent Kinetic Energy at the Surface of the Global Ocean*. Max Planck Institute für Meteorologie Hamburg report nr. 15, Hamburg, Germany.
- Pacanowski, R. C. (1996). MOM 2 Documentation, User’s Guide and Reference Manual. *GFDL Tech. Report*, **3.1**.
- Paillard, D., Ghil, M., and Le Treut, H. (1993). Dissolved organic matter and the glacial-interglacial pCO₂ problem. *Global Biogeochem. Cycles*, **7**, 901–914.
- Pedlosky, J. (1987). *Geophysical Fluid Dynamics. 2nd Edn.* Springer-Verlag, New York.
- Pedlosky, J. (1996). *Ocean Circulation Theory*. Springer, New York.
- Philander, S. G. H. (1990). *El Niño and the Southern Oscillation*. Academic Press, New York.
- Plaut, G. and Vautard, R. (1994). Spells of low-frequency oscillations and weather regimes in the northern hemisphere. *J. Atmos. Sci.*, **51**, 210–236.

- Plaut, G., Ghil, M., and Vautard, R. (1995). Interannual and interdecadal variability in 335 years of Central England Temperature. *Science*, **268**, 710–713.
- Preisendorfer, R. W. (1988). *Principal Component Analysis in Meteorology and Oceanography*. Elsevier, Amsterdam, The Netherlands.
- Primeau, F. W. (1998). *Multiple Equilibria and Low-Frequency Variability of Wind-Driven Ocean Models*. Ph.D. thesis, M.I.T. and Woods Hole, Boston, MA, U.S.A.
- Primeau, F. W. (2002). Multiple equilibria and low-frequency variability of the wind-driven ocean circulation. *J. Phys. Oceanogr.*, **32**, 2236–2256.
- Quon, C. and Ghil, M. (1992). Multiple equilibria in thermohaline convection due to salt-flux boundary conditions. *J. Fluid Mech.*, **245**, 449–484.
- Quon, C. and Ghil, M. (1995). Multiple equilibria and stable oscillations in thermohaline convection at small aspect ratio. *J. Fluid Mech.*, **291**, 33–56.
- Rahmstorf, S. (1995a). Bifurcations of the Atlantic thermohaline circulation in response to changes in the hydrological cycle. *Nature*, **378**, 145–149.
- Rahmstorf, S. (1995b). Multiple convection patterns and thermohaline flow in an idealized OGCM. *J. Climate*, **8**, 3028–3039.
- Rahmstorf, S. (2000). The thermohaline circulation: a system with dangerous thresholds? *Climatic Change*, **46**, 247–256.
- Richardson, P. (1980). Benjamin Franklin and Timothy Folger’s first printed chart of the Gulf Stream. *Science*, **207**, 643–645.
- Rivin, I. and Tziperman, E. (1997). Linear versus self-sustained interdecadal thermohaline variability in a coupled box model. *J. Phys. Oceanogr.*, **27**, 1216–1232.

- Robbins, P. E. and Toole, J. M. (1997). The dissolved silica budget as a constraint on the meridional overturning circulation of the Indian Ocean. *Deep-Sea Research*, **44**, 879–906.
- Robinson, A. R. E. (1983). *Eddies in Marine Science*. Springer-Verlag, New York, U.S.A., 609 pp.
- Rooth, C. (1982). Hydrology and ocean circulation. *Progress in Oceanography*, **11**, 131–149.
- Sakai, K. and Peltier, W. R. (1995). A simple model of the Atlantic thermohaline circulation: Internal and forced variability with paleoclimatological implications. *J. Geophys. Res.*, **100**, 13,455 – 13,479.
- Salmon, R. (1986). A simplified linear ocean circulation theory. *J. Mar. Res.*, **44**, 695–711.
- Sarmiento, J. L. and Toggweiler, J. R. (1984). A new model for the role of the oceans in determining atmospheric CO₂. *Nature*, **308**, 621–624.
- Schlichting, H. (1968). *Boundary layer theory, 5th edition*. Mc-Graw-Hill, New York.
- Schlösser, P., Bonisch, G., Rhein, M., and Bayer, R. (1991). Reduction of deep water formation in the Greenland Sea during the 1980s: evidence from tracer data. *Science*, **251**, 1054–1056.
- Schmeits, M. J. and Dijkstra, H. A. (2000). On the physics of the 9 months variability in the Gulf Stream region: combining data and dynamical systems analysis. *J. Phys. Oceanogr.*, **30**, 1967–1987.
- Schmeits, M. J. and Dijkstra, H. A. (2001). Bimodality of the Kuroshio and the Gulf Stream. *J. Phys. Oceanogr.*, **31**, 2971–2985.

- Schmitt, R. W., Bogden, P., and Dorman, C. (1989). Evaporation minus precipitation and density fluxes for the North Atlantic. *J. Phys. Oceanogr.*, **19**, 1208–1221.
- Schmitz, W. J. (1995). On the interbasin-scale thermohaline circulation. *Rev. Geophys.*, **33**, 151–173.
- Schneider, S. H. and Dickinson, R. E. (1974). Climate modelling. *Rev. Geophys. Space Phys.*, **25**, 447–493.
- Schott, F. and Molinari, R. L. (1996). The western boundary circulation of the subtropical warm watersphere. In W. Krauss, editor, *The Warmwatersphere of the North Atlantic Ocean*, pages 229–252. Borntraeger, Berlin-Stuttgart, Germany.
- Seager, R., Battisti, D. S., Yin, J., Gordon, N., Naik, N., Clement, A. C., and Cane, M. A. (2001). Is the Gulf Stream responsible for Europe’s mild winters? *Quart. J. Roy. Meteor. Soc.*, **128**, 2563 – 2586.
- Semtner, A. J. and Chervin, R. M. (1992). Ocean general circulation from a global eddy-resolving model. *J. Geophys. Res.*, **97**, 5493–5550.
- Seydel, R. (1994). *Practical Bifurcation and Stability Analysis: From Equilibrium to Chaos*. Springer-Verlag, New York, U.S.A.
- Sheremet, V. A., Ierley, G. R., and Kamenkovich, V. M. (1997). Eigenanalysis of the two-dimensional wind-driven ocean circulation problem. *J. Mar. Res.*, **55**, 57–92.
- Shilnikov, L. P. (1965). A case of the existence of a denumerable set of periodic motions. *Sov. Math. Dokl.*, **6**, 163–166.
- Simonnet, E. and Dijkstra, H. A. (2002). Spontaneous generation of low-frequency modes of variability in the wind-driven ocean circulation. *J. Phys. Oceanogr.*, **32**, 1747–1762.

- Simonnet, E., Ghil, M., Ide, K., Temam, R., and Wang, S. (2003a). Low-frequency variability in shallow-water models of the wind-driven ocean circulation. Part I: Steady-state solutions. *J. Phys. Oceanogr.*, **33**, 712–728.
- Simonnet, E., Ghil, M., Ide, K., Temam, R., and Wang, S. (2003b). Low-frequency variability in shallow-water models of the wind-driven ocean circulation. Part II: Time dependent solutions. *J. Phys. Oceanogr.*, **33**, 729–752.
- Smale, S. (1995). Differentiable dynamical systems. *Bull. Amer. Math. Soc.*, **73**, 747–817.
- Smith, R. D., Maltrud, M. E., Bryan, F. O., and Hecht, M. W. (2000). Numerical simulation of the North Atlantic Ocean at $\frac{1}{10}^\circ$. *J. Phys. Oceanogr.*, **30**, 1532–1561.
- Speich, S., Dijkstra, H. A., and Ghil, M. (1995). Successive bifurcations of a shallow-water model with applications to the wind driven circulation. *Nonlin. Proc. Geophys.*, **2**, 241–268.
- Stammer, D. R., Tokmakian, R., Semtner, A., and Wunsch, C. (1994). How well does a $\frac{1}{4}^\circ$ global circulation model simulate large-scale oceanic observations? *J. Geophys. Res.*, **101**, 25,779–25,811.
- Stommel, H. (1948). The westward intensification of wind-driven ocean currents. *Trans. Amer. Geophysical Union*, **29**, 202–206.
- Stommel, H. (1951). An elementary explanation of why ocean currents are strongest in the west. *Bull. Amer. Meteorol. Soc.*, **32**, 21–23.
- Stommel, H. (1961). Thermohaline convection with two stable regimes of flow. *Tellus*, **2**, 244–230.
- Strong, C., Jin, F.-F., and Ghil, M. (1995). Intraseasonal oscillations in a barotropic model with annual cycle, and their predictability. *J. Atmos. Sci.*, **52**, 2627–2642.

- Sverdrup, H. U. (1947). Wind-driven currents in a baroclinic ocean with application to the equatorial current in the eastern Pacific. *Proc. Natl. Acad. Sci. Wash.*, **33**, 318–326.
- Sverdrup, H. U., Johnson, M. W., and Fleming, R. H. (1946). *The oceans: their physics, chemistry and general biology*. Prentice Hall.
- Sy, A., Rhein, M., Lazier, J. N. R., Koltermann, K. P., Meincke, J., Putzka, A., and Bersch, M. (1997). Surprisingly rapid spreading of newly formed intermediate waters across the North Atlantic Ocean. *Nature*, **388**, 563–567.
- Talley, L. D. (1999). Some aspects of ocean heat transport by the shallow, intermediate and deep overturning circulations. In P. Clark, R. S. Webb, and L. D. Keigwin, editors, *Mechanisms of Global Climate Change*. AGU, Washington, DC, U.S.A.
- Tansley, C. E. and Marshall, D. P. (2001). An Implicit Formula for Boundary Current Separation. *J. Phys. Oceanogr.*, **31**, 1633–1638.
- Te Raa, L. A. and Dijkstra, H. A. (2002). Instability of the thermohaline ocean circulation on interdecadal time scales. *J. Phys. Oceanogr.*, **32**, 138–160.
- Te Raa, L. A. and Dijkstra, H. A. (2003). Sensitivity of North Atlantic multidecadal variability to freshwater flux forcing. *J. Climate*, **32**, 138–160.
- Thual, O. and McWilliams, J. C. (1992). The catastrophe structure of thermohaline convection in a two-dimensional fluid model and a comparison with low-order box models. *Geophys. Astrophys. Fluid Dyn.*, **64**, 67–95.
- Tziperman, E. (1997). Inherently unstable climate behavior due to weak thermohaline ocean circulation. *Nature*, **386**, 592–595.
- Tziperman, E., Toggweiler, J. R., Feliks, Y., and Bryan, K. (1994). Instability of the thermohaline circulation with respect to mixed boundary conditions: Is it really a

problem for realistic models? *J. Phys. Oceanogr.*, **24**, 217–232.

Vazquez, J., Zlotnicki, V., and Fu, L.-L. (1990). Sea level variabilities in the Gulf Stream between Cape Hatteras and 50°W: A Geosat study. *J. Geophys. Res.*, **95(C10)**, 17957–17964.

Vellinga, M. (1996). Instability of two-dimensional thermohaline circulation. *J. Phys. Oceanogr.*, **26**, 305–319.

Vellinga, M. (1998). Multiple equilibria of the thermohaline circulation as a side effect of convective adjustment. *J. Phys. Oceanogr.*, **28**, 305–319.

Veronis, G. (1963). An analysis of the wind-driven ocean circulation with a limited number of Fourier components. *J. Atmos. Sci.*, **20**, 577–593.

Veronis, G. (1966). Wind-driven ocean circulation. II: Numerical solution of the nonlinear problem. *Deep-Sea Research*, **13**, 31–55.

Walín, G. (1985). The thermohaline circulation and the control of ice ages. *Paleogeogr. Paleoclim. Paleoecol.*, **50**, 323–332.

Wang, L. and Kobalinsky, C. (1995). Low-frequency variability in regions of the Kuroshio Extension and the Gulf Stream. *J. Geophys. Res.*, **100**, 18,313–18,331.

Weaver, A. J. and Hughes, T. M. (1994). Rapid interglacial climate fluctuations driven by North Atlantic ocean circulation. *Nature*, **367**, 447–450.

Weaver, A. J. and Sarachik, E. S. (1991). The role of mixed boundary conditions in numerical models of the ocean's climate. *J. Phys. Oceanogr.*, **21**, 1470–1493.

Weaver, A. J., Sarachik, E. S., and Marotzke, J. (1991). Freshwater flux forcing of decadal and interdecadal oceanic variability. *Nature*, **353**, 836–838.

- Weaver, A. J., Marotzke, J., Cummings, P. F., and Sarachik, E. S. (1993). Stability and variability of the thermohaline circulation. *J. Phys. Oceanogr.*, **23**, 39–60.
- Weaver, A. J., Aura, S., and Myers, P. G. (1994). Interdecadal variability in an idealized model of the North Atlantic. *J. Geophys. Res.*, **99**, 12,423 – 12,441.
- Weijer, W. and Dijkstra, H. A. (2001). Bifurcations of the three-dimensional thermohaline circulation: the double hemispheric case. *J. Mar. Res.*, **59**, 599–631.
- Weijer, W., De Ruijter, W. P. M., Dijkstra, H. A., and Van Leeuwen, P. J. (1999). Impact of interbasin exchange on the Atlantic overturning circulation. *J. Phys. Oceanogr.*, **29**, 2266–2284.
- Welander, P. (1982). A simple heat-salt oscillator. *Dyn. Atmos. Oceans*, **6**, 233–242.
- Welander, P. (1986). Thermohaline effects in the ocean circulation and related simple models. In J. Willebrand and D. L. T. Anderson, editors, *Large-Scale Transport Processes in Oceans and Atmosphere*, pages 163–200. D. Reidel.
- Wijffels, S. E., Schmitt, R. W., Bryden, H. L., and Stigebrandt, A. (1992). Transport of fresh water by the ocean. *J. Phys. Oceanogr.*, **22**, 155–163.
- WOCE (2001). *Ocean Circulation and Climate: Observing and Modeling the Global Ocean Ocean [Siedler, G. and Church, J. and Gould, J. (eds)]*. Academic Press, San Diego, USA.
- Wright, D. G. and Stocker, T. F. (1992). Sensitivities of a zonally averaged global ocean circulation model. *J. Geophys. Res.*, **97**, 12707–12730.
- Wright, D. G., Vreugdenhil, C. B., and Hughes, T. M. (1995). Vorticity dynamics and zonally averaged ocean models. *J. Phys. Oceanogr.*, **25**, 2141–2154.

Wright, D. G., Stocker, T., and Mercer, D. (1998). Closures used in zonally averaged ocean models. *J. Phys. Oceanogr.*, **28**, 791–804.

Wunsch, C. (1996). *The Ocean Circulation Inverse Problem*. Cambridge University Press, Cambridge, U.K.

Wyrtki, K., Magaard, L., and Hagger, J. (1971). Eddy energy in the oceans. *J. Geophys. Res.*, **81**, 26412646.

Yang, J. and Neelin, J. D. (1993). Sea-ice interaction with the thermohaline circulation. *Geophys. Res. Letters*, **20**, 217–220.

Zaucker, F., Stocker, T. F., and Broecker, W. S. (1994). Atmospheric freshwater fluxes and their effect on the global thermohaline circulation. *J. Geophys. Res.*, **99**, 12,443–12,457.

Figure 1. (a) An ‘artist’s rendering’ of the composite power spectrum of climate variability showing the amount of variance in each frequency range (from Ghil [2002]). (b) Spectrum of the Central England Temperature time series from 1650 to the present (from Plaut et al. [1995]). Each peak in the spectrum is tentatively attributed to a physical mechanism; see original reference for details.

Figure 2. Sketch of the global ocean circulation as a “conveyor belt.” Dark shaded paths indicate flow in the surface ocean, light shaded paths flow in the deep ocean. Numbers indicate volume transport in Sverdrup; $1 \text{ Sv} = 10^6 \text{ m}^3 \text{ s}^{-1}$ (based on Schmitz [1995] but taken from Bradley [1999]).

Figure 3. Composite, multipass image of the average sea-surface temperature field in May 1996 within the Gulf Stream region. The infrared data used to obtain this picture were obtained from high-resolution (0.5° horizontally) observations from the Advanced Very High Resolution Radiometer (AVHRR, see <http://fermi.jhuapl.edu/avhrr/index.html>). In a multipass image, the ‘warmest’ pixel is selected from each pass, three days apart.

Figure 4. (a) Bifurcation diagram for the solutions found in an 1.5-layer shallow-water model by forward time integration. The meridional position of the confluence point (see panels b and c) is plotted on the ordinate, in km away from the symmetry axis; on the abscissa a nondimensional measure α_τ of the wind-stress strength is shown. Markers indicate bifurcation points, with a solid circle for the saddle-node bifurcation and a solid triangle for either Hopf bifurcation. Heavy solid and dashed lines indicate steady states, stable and unstable, respectively. Light solid and dashed lines give the range of variability for the periodic and aperiodic solutions, respectively. (b, c) Patterns of the thickness field $h = h(x, y)$ of the upper, active layer’s thickness for the two stable steady-state solutions at $\alpha_\tau = 0.9$. Thicknesses $h > D = 500 \text{ m}$ are solid, those with $h < D$ are dashed; contour interval is 5 m. The position of the confluence point is indicated in both panels. The nondimensional friction coefficient is $\alpha_A = 1.3$ in all three panels (from Jiang et al. [1995]). (d) Sketch of the wind-stress forcing for the idealized double-gyre problem.

Figure 5. (a) Typical variation of the kinetic energy of the double-gyre flow in a large basin for the high-forcing or low-dissipation regime. (b) Typical patterns of the streamfunction for the high-energy state (left panel) and the low-energy state (right panel); from McCalpin and Haidvogel [1996].

Figure 6. (a) Bifurcation diagram for a barotropic shallow-water model of the North Atlantic with the Ekman number as control parameter. The nondimensional Ekman number, $E = A_H / (2\Omega r_0^2)$, where Ω and r_0 are the angular frequency and radius of the Earth, respectively, is plotted on the abscissa, while the maximum northward volume transport is plotted on the ordinate. Solid (dotted) branches indicate stable (unstable) steady states, as usual, whereas the Hopf bifurcation points are indicated by solid triangles. (b,c) Contour plots of the layer-thickness anomaly for two coexisting unstable solutions at $E = 1.6 \times 10^{-7}$; the contour levels are scaled with respect to the maximum value of the field; only a small part of the domain, ($85^\circ \text{ W} - 45^\circ \text{ W}$, $24^\circ \text{ N} - 51^\circ \text{ N}$), is shown: (b) ‘deflected’ Gulf Stream; and (c) ‘separated’ Gulf Stream. (d,e) Spatial pattern of the linear oscillatory mode at H_1 in panel (a); layer-thickness anomalies for (d) the real and (e) the imaginary part (from Schmeits and Dijkstra [2000]).

Figure 7. (a) Time evolution of the mean-monthly meridional displacement of the position of the SST isotherm $T = 15^\circ\text{C}$ away from the latitude 41°N at 50°W , January 1960–December 1997. The SST field has been spatially interpolated by cubic splines in the interval 30°N – 60°N in order to compute the deviation from its mean-latitude position; the data are derived from the COADS data set. Both the raw data (light solid) and data-adaptively low-pass filtered signal (heavy solid) are shown; the latter is based on singular-spectrum analysis (SSA) with a 16-year window, which retains the 8 modes with lowest frequencies, after filtering out the annual and subannual signals. (b) Maximum-entropy spectrum of the low-pass filtered time series shown in panel (a), given in log-linear coordinates. The order of the maximum-entropy method (MEM) is 40; only the powers of ten are indicated on the ordinate. (c) Results from a 100-year simulation with a 2.5-layer shallow-water model within a basin that approximates the North Atlantic in size and shape, using an idealized wind stress. Maximum entropy spectrum of the subpolar-gyre kinetic energy. The SSA window length is 20 years, the number of modes retained is 12, and the MEM order is 40; same coordinates and labeling as in panel (b) (from Simonnet et al. [2004]).

Figure 8. Potential temperature (θ) section at 24°W in the Atlantic; NADW is characterized by $\theta \approx 3^\circ\text{C}$, while AABW is characterized by $\theta \approx 0.5^\circ\text{C}$ (from Talley [1999]).

Figure 9. Time series of ocean heat content (10^{22}J) in the upper 300 m of the Atlantic for the half-century 1948–1998. (from Levitus et al. [2000]).

Figure 10. (a) Sketch of the two-box model set-up of Stommel [1961]. Two reservoirs contain well-mixed water and are connected through an overflow and a capillary tube. The circulation is driven by density gradients between the boxes; these are due to heat and salinity fluxes at the surface. The direction of flow between boxes corresponds to a thermally dominated solution, with $\Psi > 0$ and implied sinking in the polar and rising in the equatorial box. (b) Evolution of $T(t)$ and $S(t)$ for a solution with zero initial data, $T(0) = S(0) = 0$; $\eta_1 = 3.0$, $\eta_2 = 0.5$ and $\eta_3 = 0.3$. (c) Trajectories in the (T, S) plane for three different initial states (labeled by diamonds) that can lead to two different steady states (labeled by crosses); here $\eta_2 = 1.0$, while $\eta_1 = 3.0$, $\eta_3 = 0.3$, as in panel (b).

Figure 11. (a) Bifurcation diagram for the flow Ψ versus the salinity flux η_2 , with fixed $\eta_1 = 3.0$ and $\eta_3 = 0.3$. The labels TH, SA indicate the thermally driven and salinity driven solutions. (b) Regime diagram, showing the locus of the saddle-node bifurcations L_1 and L_2 of panel (a) in the (η_1, η_2) parameter plane, for $\eta_3 = 0.3$. (c) Sketch of the physics of the salt-advection feedback. The mean circulation is indicated by the normal-pointed arrows. The upper-ocean temperature and salinity fields can be inferred from the surface forcing of heat and freshwater. A perturbation which strengthens the circulation leads to a poleward salt transport (F_S), which causes an amplification (open-headed arrows); it also leads to increased heat transport (F_T), which damps the original perturbation (closed-headed arrows).

Figure 12. Bifurcation and regime diagrams for a 2-D Boussinesq model of the thermohaline circulation (THC). (a) Approximate pitchfork bifurcation diagram obtained by a “poor-man’s continuation method”; the closed circles indicate steady-state solutions obtained by forward integration (from Quon and Ghil [1992]). (b) Accurate pitchfork bifurcation diagram obtained by pseudo-arclength continuation. The points H indicate subsequent Hopf bifurcations (from Dijkstra and Molemaker [1997]). Note that the scale on the abscissa and the variable used on the ordinate are not the same in panels (a) and (b). (c) Approximate regime diagram. Full symbols (circles and squares) represent asymmetric solutions and the smooth curve separates these from the symmetric ones (open symbols; from Quon and Ghil [1992]).

Figure 13. *Steady states obtained in an ocean GCM limited to an idealized 60° -wide sectorial configuration, subject to mixed boundary conditions; zonal averages of the velocity field are plotted as a meridional-plane streamfunction field. (a) Reference state obtained with equatorially symmetric, restoring boundary conditions. (b) Circulation obtained after adding a negative salinity perturbation of 1 psu south of 45° S. (c) Circulation after adding a positive salinity perturbation of 2 psu south of 45° S. (d) Circulation after adding a positive salinity perturbation of 2 psu north of 45° N (from Bryan [1986]).*

Figure 14. *Model response to transient forcing, presented as a schematic bifurcation diagram. The amount of NADW in the solution is plotted vs. the amplitude of the perturbation in freshwater forcing. This schematic diagram is obtained by indirect reasoning applied to results of time-dependent numerical experiments with a particular spatial pattern and rate-of-change in time of the forcing perturbation for a global ocean GCM (from Rahmstorf [2000]); see the original reference for the heuristic interpretation of the solid and dotted segments, various types of arrows, and other symbols.*

Figure 15. *(a) Regime for a hybrid coupled model. The parameters d and λ_{oa} are the atmospheric EBM's thermal diffusivity and the proportionality constant for the air-sea heat flux, respectively. Solid circles in both diagrams indicate numerically computed steady states, open circles indicate periodic solutions (from Chen and Ghil [1996]). (b-e) Interdecadal oscillation in the hybrid coupled model. SST anomaly patterns shown at intervals of about 5.5 years to cover roughly half a period of the 44-year oscillation*

Figure 16. *Interdecadal variability in the GFDL coupled ocean-atmosphere model (from Delworth et al. [1993]). (a) Time series of annual-mean THC index over 200 years of integration. (b) SST pattern obtained as the difference of four model-simulated decades of high-THC-index states and four model simulated low-THC-index states. (c) Pattern of interdecadal SST anomalies obtained as the difference between two 15-year long intervals: the relatively warm interval 1950–1964 and the relatively cold interval 1970–1984 (last panel from Kushnir [1994]).*

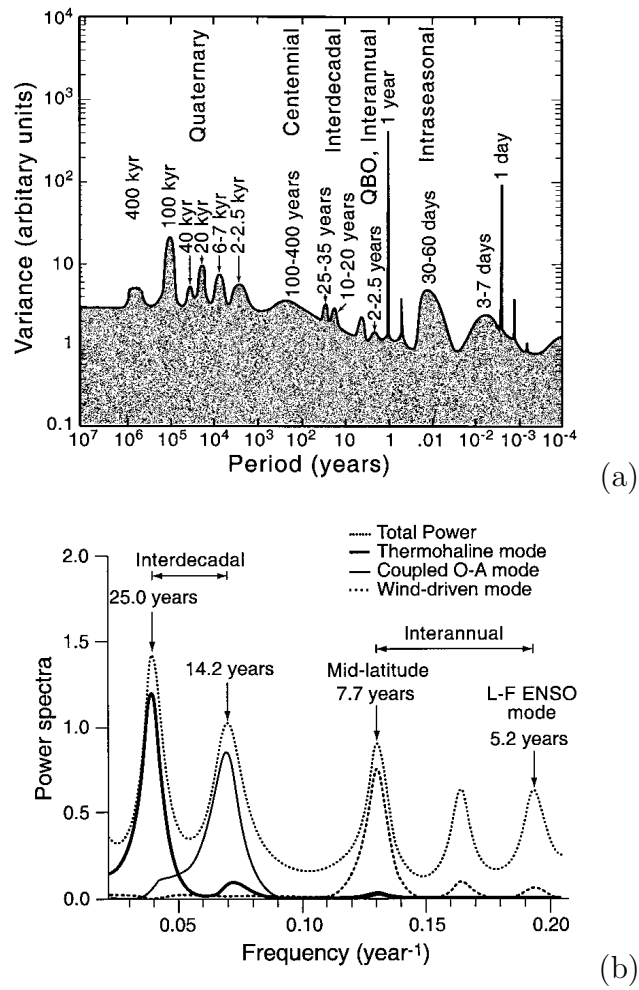


Figure 1. (a) An ‘artist’s rendering’ of the composite power spectrum of climate variability showing the amount of variance in each frequency range (from Ghil [2002]). (b) Spectrum of the Central England Temperature time series from 1650 to the present (from Plaut et al. [1995]). Each peak in the spectrum is tentatively attributed to a physical mechanism; see original reference for details.

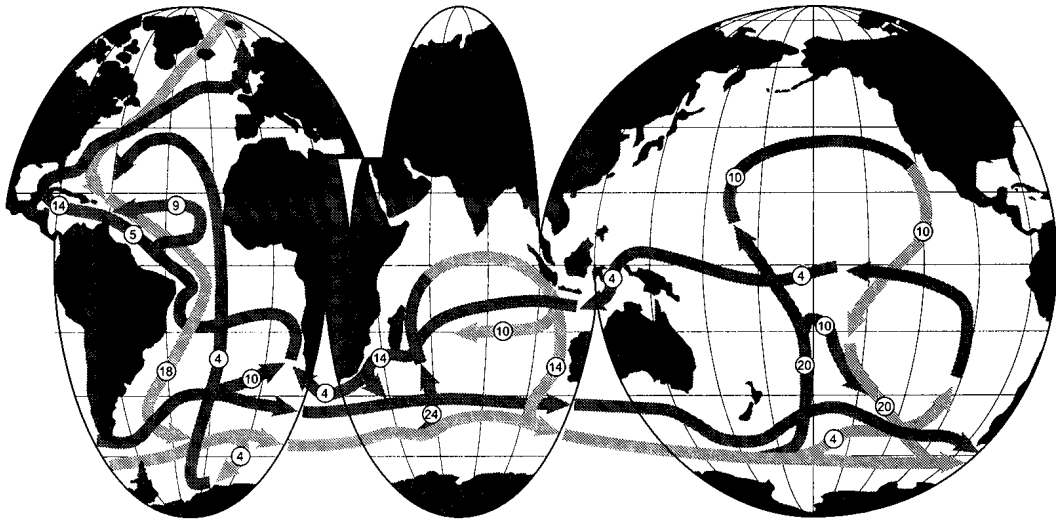


Figure 2. Sketch of the global ocean circulation as a “conveyor belt.” Dark shaded paths indicate flow in the surface ocean, light shaded paths flow in the deep ocean. Numbers indicate volume transport in Sverdrup; $1 \text{ Sv} = 10^6 \text{ m}^3 \text{ s}^{-1}$ (based on Schmitz [1995] but taken from Bradley [1999]).

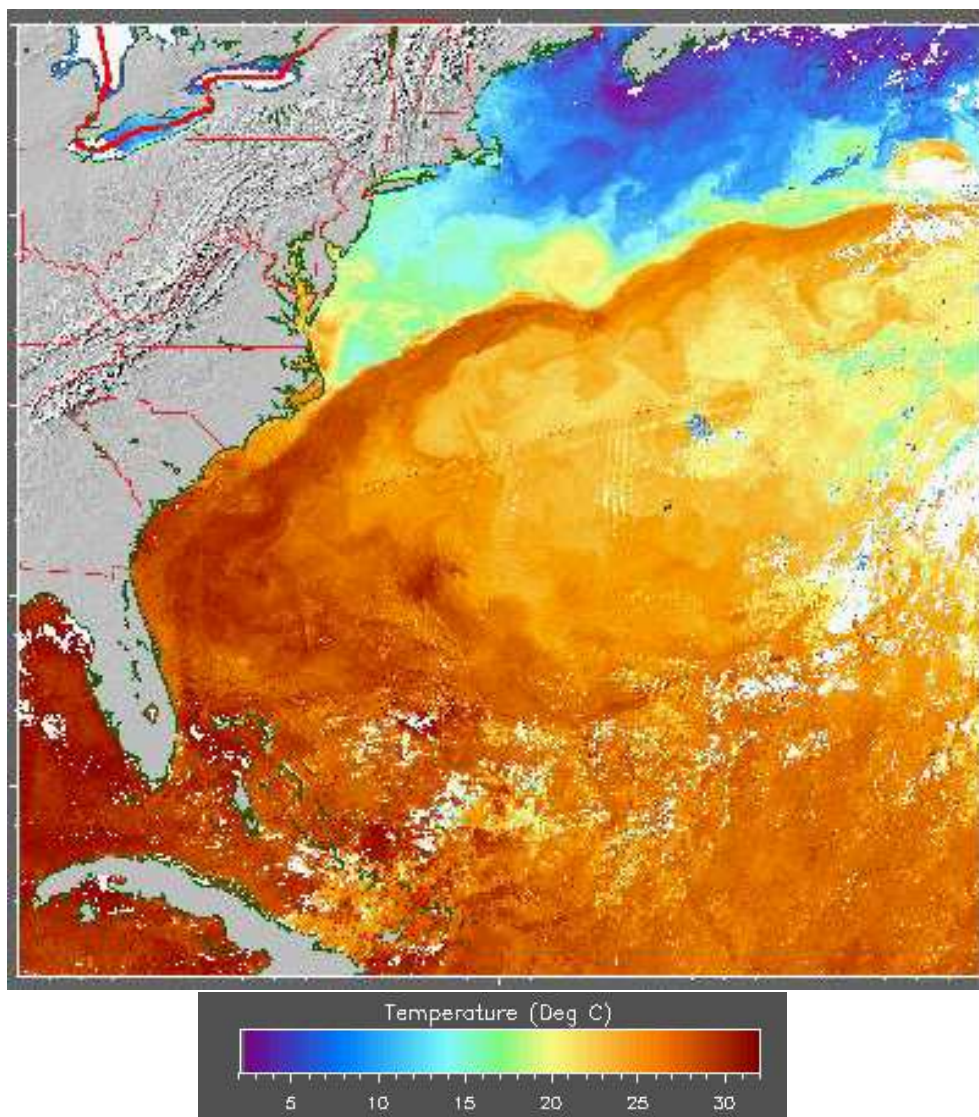


Figure 3. *Composite, multipass image of the average sea-surface temperature field in May 1996 within the Gulf Stream region. The infrared data used to obtain this picture were obtained from high-resolution (0.5° horizontally) observations from the Advanced Very High Resolution Radiometer (AVHRR, see <http://fermi.jhuapl.edu/avhrr/index.html>). In a multipass image, the ‘warmest’ pixel is selected from each pass, three days apart.*

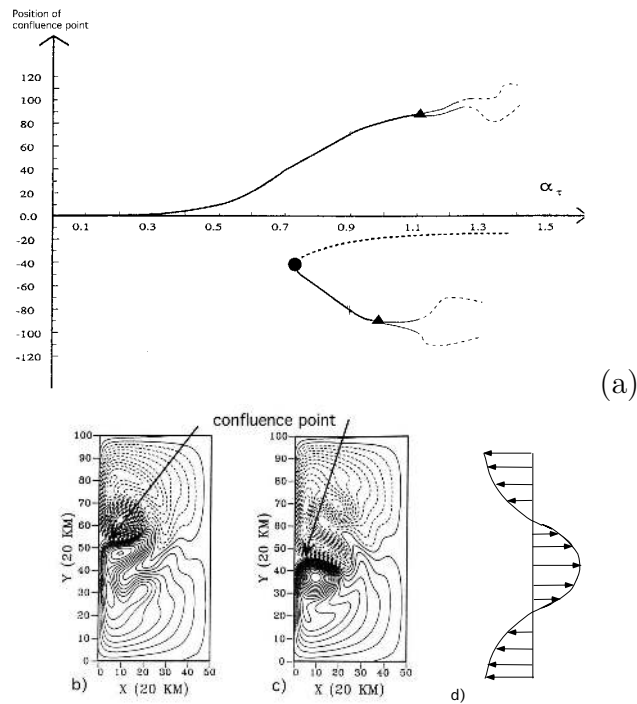


Figure 4. (a) Bifurcation diagram for the solutions found in an 1.5-layer shallow-water model by forward time integration. The meridional position of the confluence point (see panels b and c) is plotted on the ordinate, in km away from the symmetry axis; on the abscissa a nondimensional measure α_τ of the wind-stress strength is shown. Markers indicate bifurcation points, with a solid circle for the saddle-node bifurcation and a solid triangle for either Hopf bifurcation. Heavy solid and dashed lines indicate steady states, stable and unstable, respectively. Light solid and dashed lines give the range of variability for the periodic and aperiodic solutions, respectively. (b, c) Patterns of the thickness field $h = h(x, y)$ of the upper, active layer's thickness for the two stable steady-state solutions at $\alpha_\tau = 0.9$. Thicknesses $h > D = 500$ m are solid, those with $h < D$ are dashed; contour interval is 5 m. The position of the confluence point is indicated in both panels. The nondimensional friction coefficient is $\alpha_A = 1.3$ in all three panels (from Jiang et al. [1995]). (d) Sketch of the wind-stress forcing for the idealized double-gyre problem.

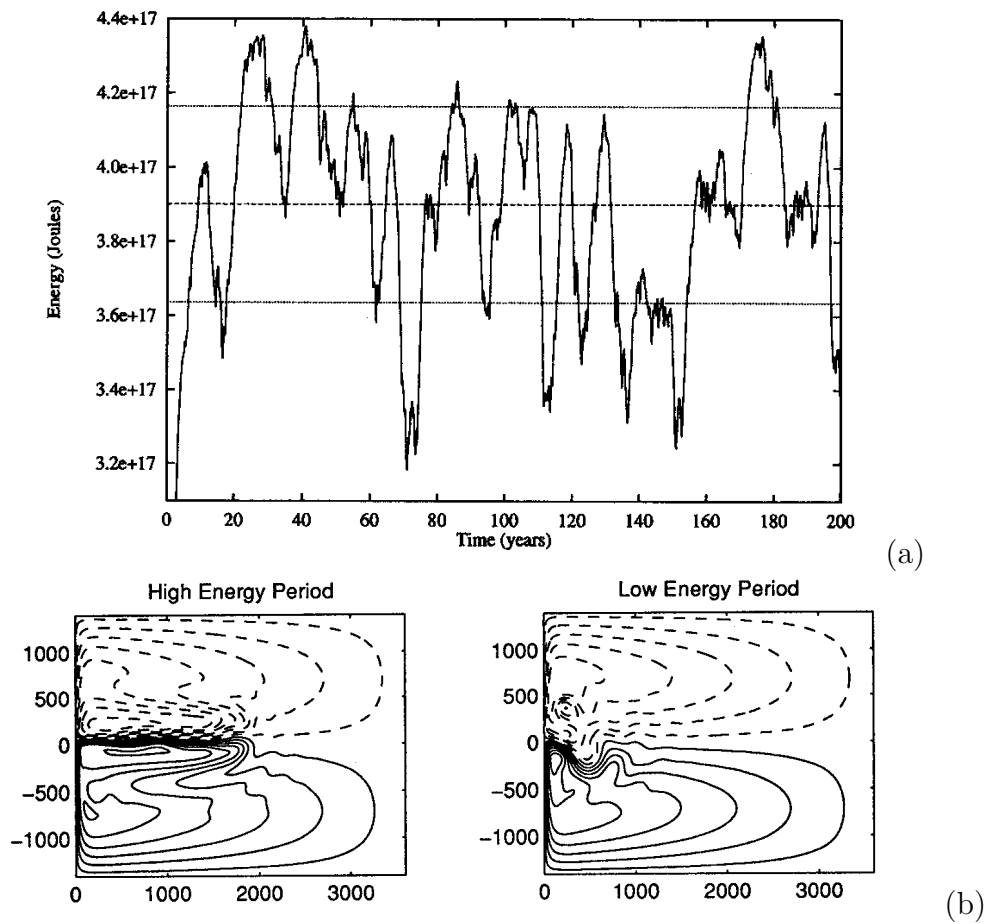


Figure 5. (a) Typical variation of the kinetic energy of the double-gyre flow in a large basin for the high-forcing or low-dissipation regime. (b) Typical patterns of the streamfunction for the high-energy state (left panel) and the low-energy state (right panel); from McCalpin and Haidvogel [1996].

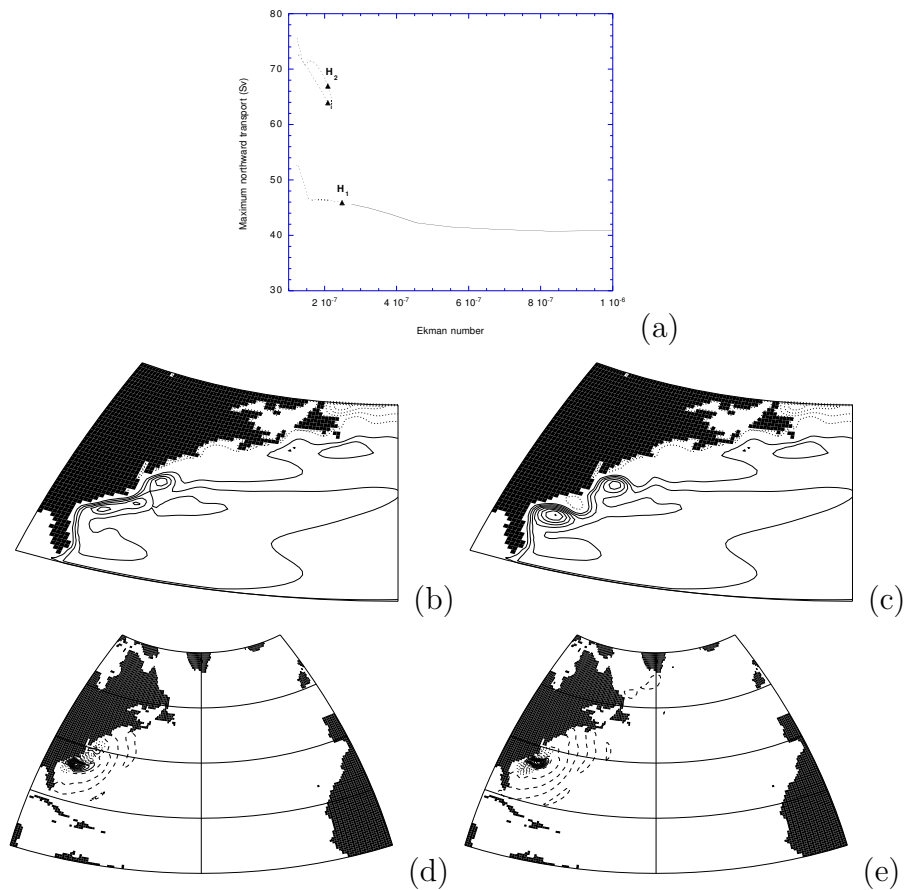


Figure 6. (a) Bifurcation diagram for a barotropic shallow-water model of the North Atlantic with the Ekman number as control parameter. The nondimensional Ekman number, $E = A_H / (2\Omega r_0^2)$, where Ω and r_0 are the angular frequency and radius of the Earth, respectively, is plotted on the abscissa, while the maximum northward volume transport is plotted on the ordinate. Solid (dotted) branches indicate stable (unstable) steady states, as usual, whereas the Hopf bifurcation points are indicated by solid triangles. (b,c) Contour plots of the layer-thickness anomaly for two coexisting unstable solutions at $E = 1.6 \times 10^{-7}$; the contour levels are scaled with respect to the maximum value of the field; only a small part of the domain, ($85^\circ W$ – $45^\circ W$, $24^\circ N$ – $51^\circ N$), is shown: (b) ‘deflected’ Gulf Stream; and (c) ‘separated’ Gulf Stream. (d,e) Spatial pattern of the linear oscillatory mode at H_1 in panel (a); layer-thickness anomalies for (d) the real and (e) the imaginary part (from Schmeits and Dijkstra [2000]).

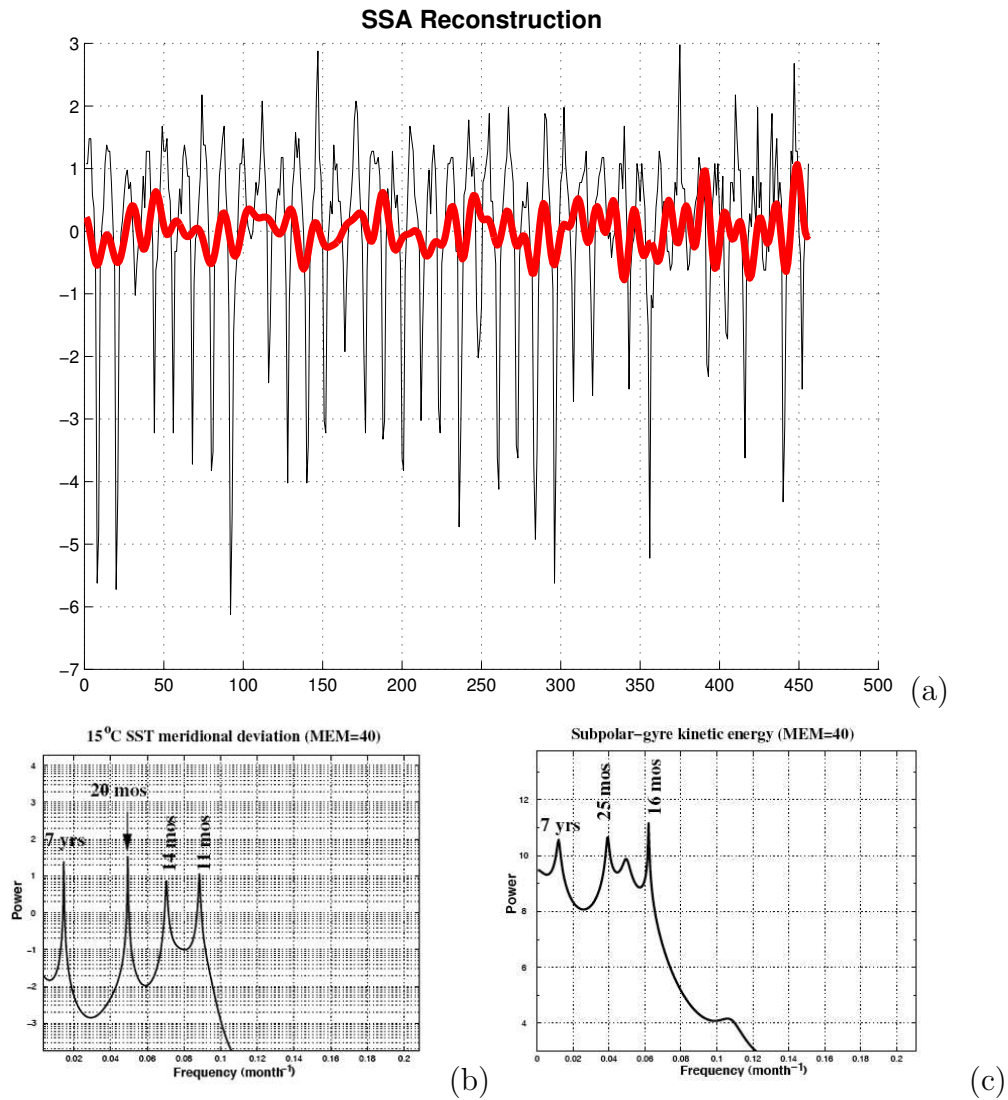


Figure 7. (a) Time evolution of the mean-monthly meridional displacement of the position of the SST isotherm $T = 15^\circ\text{C}$ away from the latitude 41°N at 50°W , January 1960–December 1997. The SST field has been spatially interpolated by cubic splines in the interval 30°N – 60°N in order to compute the deviation from its mean-latitude position; the data are derived from the COADS data set. Both the raw data (light solid) and data-adaptively low-pass filtered signal (heavy solid) are shown; the latter is based on singular-spectrum analysis (SSA) with a 16-year window, which retains the 8 modes with lowest frequencies, after filtering out the annual and subannual signals. (b) Maximum-entropy spectrum of the low-pass filtered time series shown in panel (a), given in log-linear coordinates. The order of the maximum-entropy method (MEM) is 40; only the powers of ten are indicated on the ordinate. (c) Results from a 100-year simulation with a 2.5-layer shallow-water model within a basin that approximates the North Atlantic in size and shape, using an idealized wind stress. Maximum entropy spectrum of the subpolar-gyre kinetic energy. The SSA window length is 20 years, the number of modes retained is 12, and the MEM order is 40; same coordinates and labeling as in panel (b) (from Simonnet et al. [2004]).

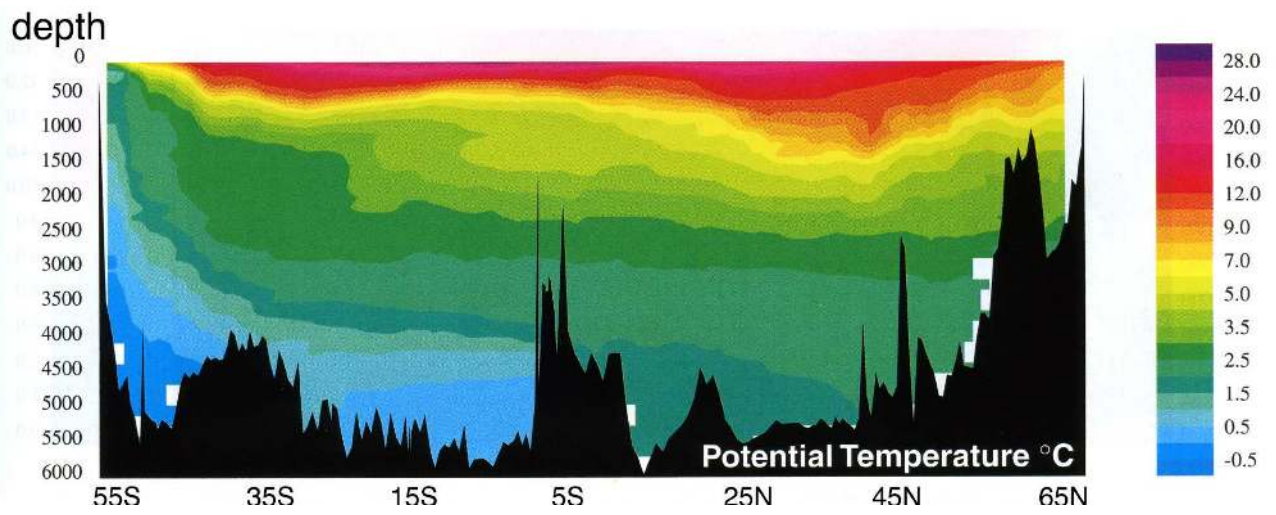


Figure 8. Potential temperature (θ) section at 24° W in the Atlantic; NADW is characterized by $\theta \approx 3^\circ$ C, while AABW is characterized by $\theta \approx 0.5^\circ$ C (from Talley [1999]).

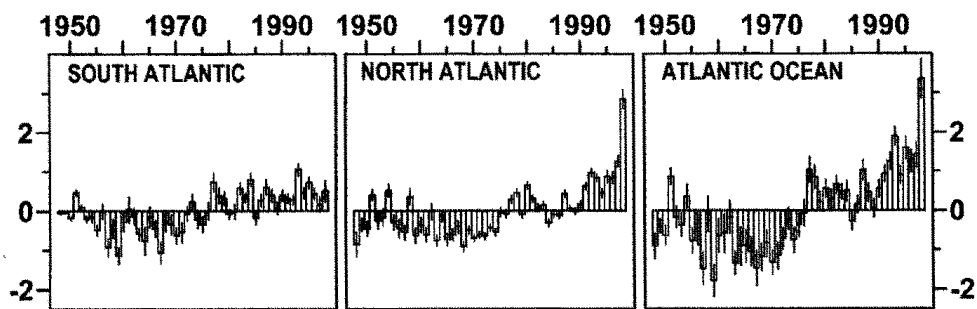


Figure 9. Time series of ocean heat content (10^{22} J) in the upper 300 m of the Atlantic for the half-century 1948–1998 (from Levitus et al. [2000]).

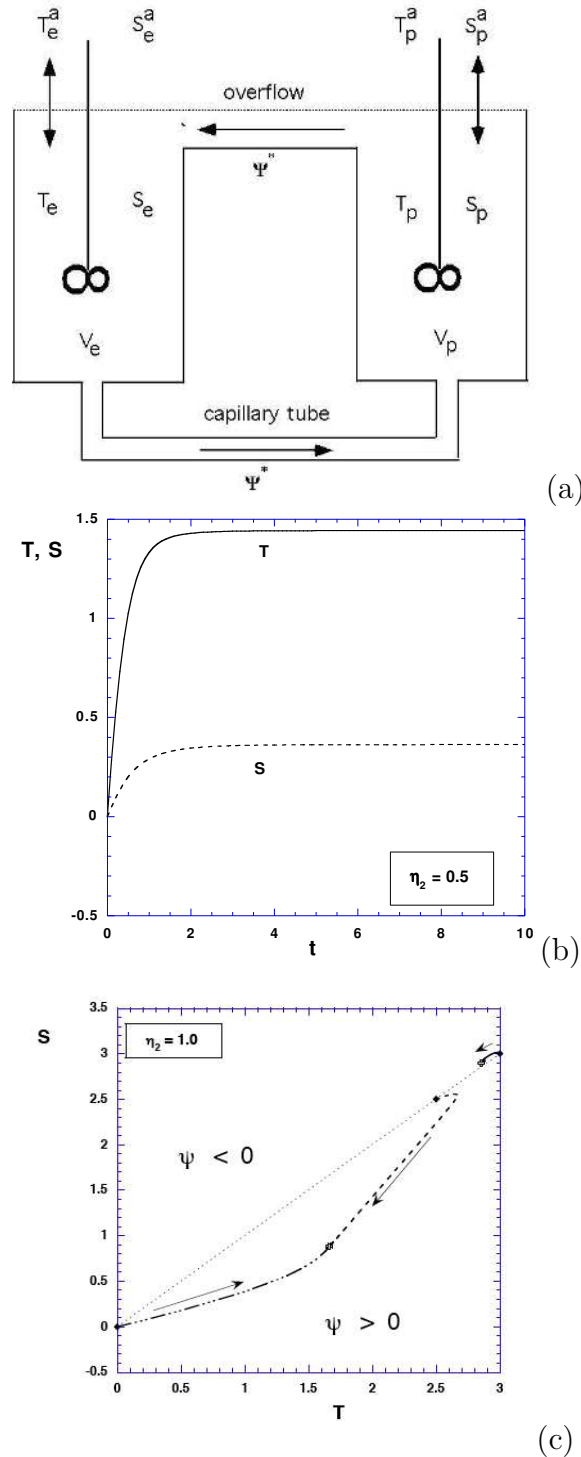


Figure 10. (a) Sketch of the two-box model set-up of Stommel [1961]. Two reservoirs contain well-mixed water and are connected through an overflow and a capillary tube. The circulation is driven by density gradients between the boxes; these are due to heat and salinity fluxes at the surface. The direction of flow between boxes corresponds to a thermally dominated solution, with $\Psi > 0$ and implied sinking in the polar and rising in the equatorial box. (b) Evolution of $T(t)$ and $S(t)$ for a solution with zero initial data, $T(0) = S(0) = 0$; $\eta_1 = 3.0$, $\eta_2 = 0.5$ and $\eta_3 = 0.3$. (c) Trajectories in the (T, S) plane for three different initial states (labeled by diamonds) that can lead to two different steady states (labeled by crosses); here $\eta_2 = 1.0$, while $\eta_1 = 3.0$, $\eta_3 = 0.3$, as in panel (b).

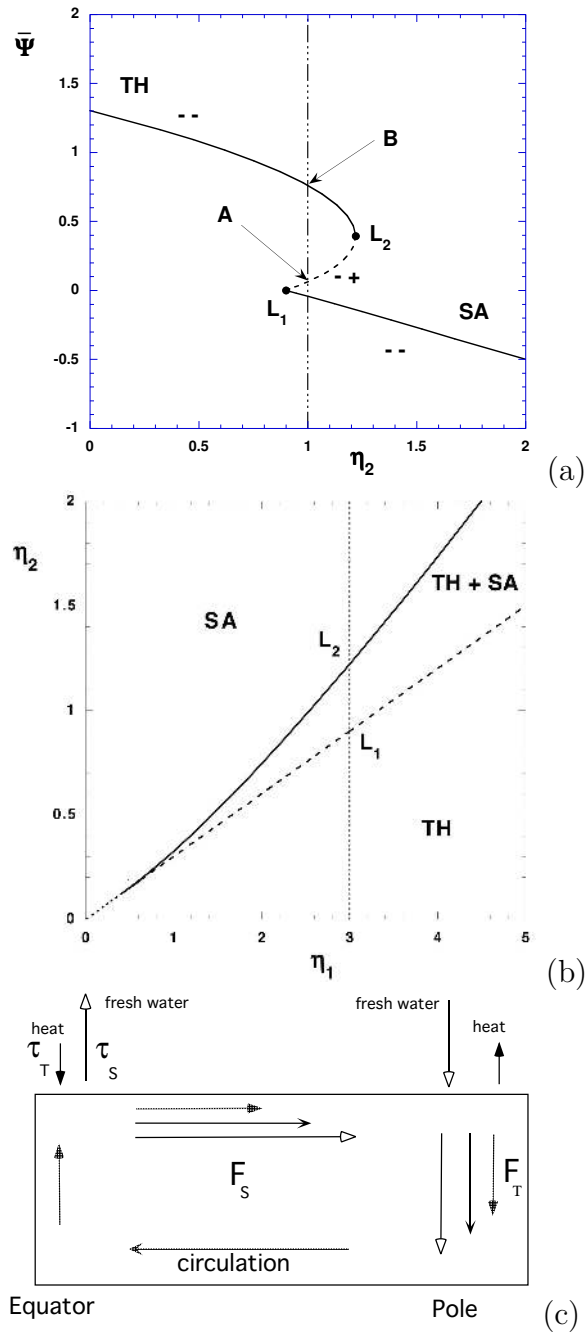


Figure 11. (a) Bifurcation diagram for the flow Ψ versus the salinity flux η_2 , with fixed $\eta_1 = 3.0$ and $\eta_3 = 0.3$. The labels TH, SA indicate the thermally driven and salinity driven solutions. (b) Regime diagram, showing the locus of the saddle-node bifurcations L_1 and L_2 of panel (a) in the (η_1, η_2) parameter plane, for $\eta_3 = 0.3$. (c) Sketch of the physics of the salt-advection feedback. The mean circulation is indicated by the normal-pointed arrows. The upper-ocean temperature and salinity fields can be inferred from the surface forcing of heat and freshwater. A perturbation which strengthens the circulation leads to a poleward salt transport (F_S), which causes an amplification (open-headed arrows); it also leads to increased heat transport (F_T), which damps the original perturbation (closed-headed arrows).

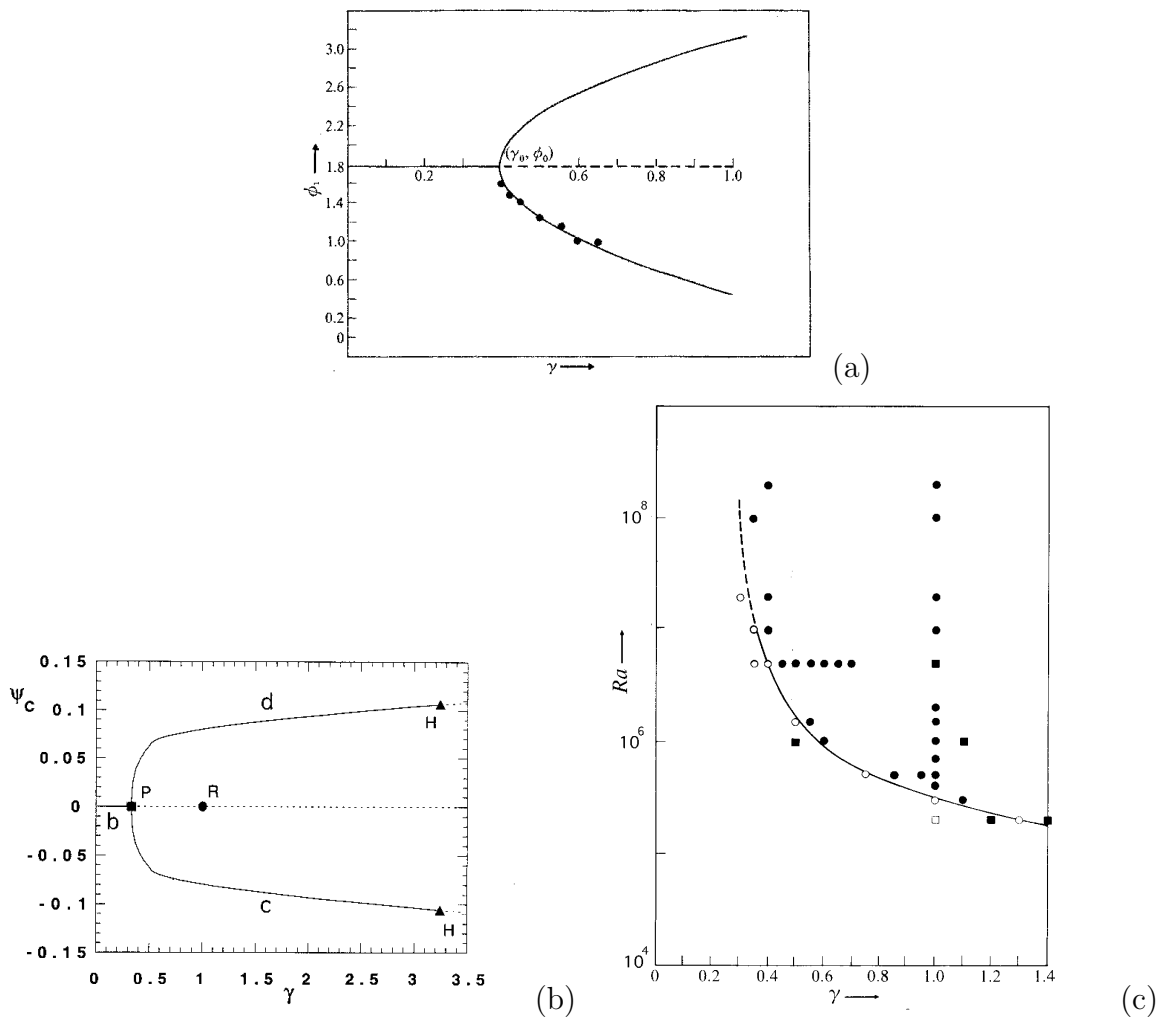


Figure 12. Bifurcation and regime diagrams for a 2-D Boussinesq model of the thermohaline circulation (THC). (a) Approximate pitchfork bifurcation diagram obtained by a “poor-man’s continuation method”; the closed circles indicate steady-state solutions obtained by forward integration (from Quon and Ghil [1992]). (b) Accurate pitchfork bifurcation diagram obtained by pseudo-arclength continuation. The points H indicate subsequent Hopf bifurcations (from Dijkstra and Molemaker [1997]). Note that the scale on the abscissa and the variable used on the ordinate are not the same in panels (a) and (b). (c) Approximate regime diagram. Full symbols (circles and squares) represent asymmetric solutions and the smooth curve separates these from the symmetric ones (open symbols; from Quon and Ghil [1992]).

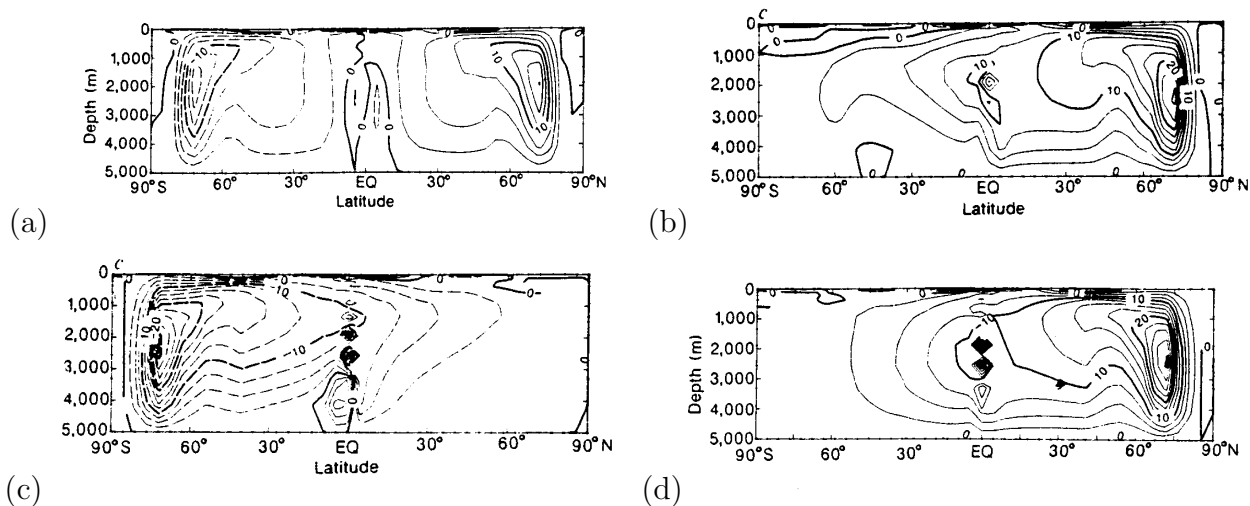


Figure 13. *Steady states obtained in an ocean GCM limited to an idealized 60°-wide sectorial configuration, subject to mixed boundary conditions; zonal averages of the velocity field are plotted as a meridional-plane streamfunction field. (a) Reference state obtained with equatorially symmetric, restoring boundary conditions. (b) Circulation obtained after adding a negative salinity perturbation of 1 psu south of 45° S. (c) Circulation after adding a positive salinity perturbation of 2 psu south of 45° S. (d) Circulation after adding a positive salinity perturbation of 2 psu north of 45° N (from Bryan [1986]).*

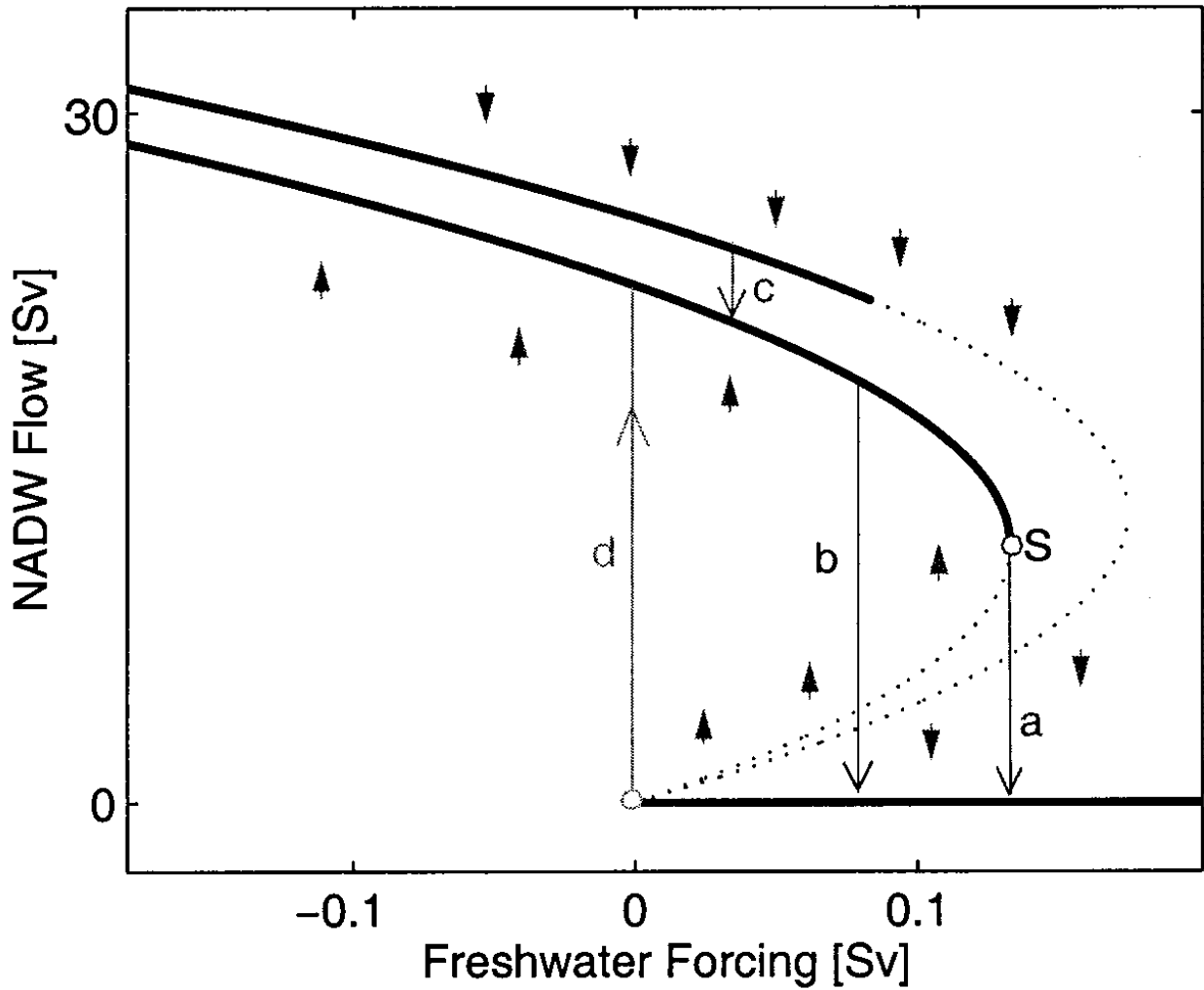


Figure 14. Model response to transient forcing, presented as a schematic bifurcation diagram. The amount of NADW in the solution is plotted vs. the amplitude of the perturbation in freshwater forcing. This schematic diagram is obtained by indirect reasoning applied to results of time-dependent numerical experiments with a particular spatial pattern and rate-of-change in time of the forcing perturbation for a global ocean GCM (from Rahmstorf [2000]); see the original reference for the heuristic interpretation of the solid and dotted segments, various types of arrows, and other symbols.

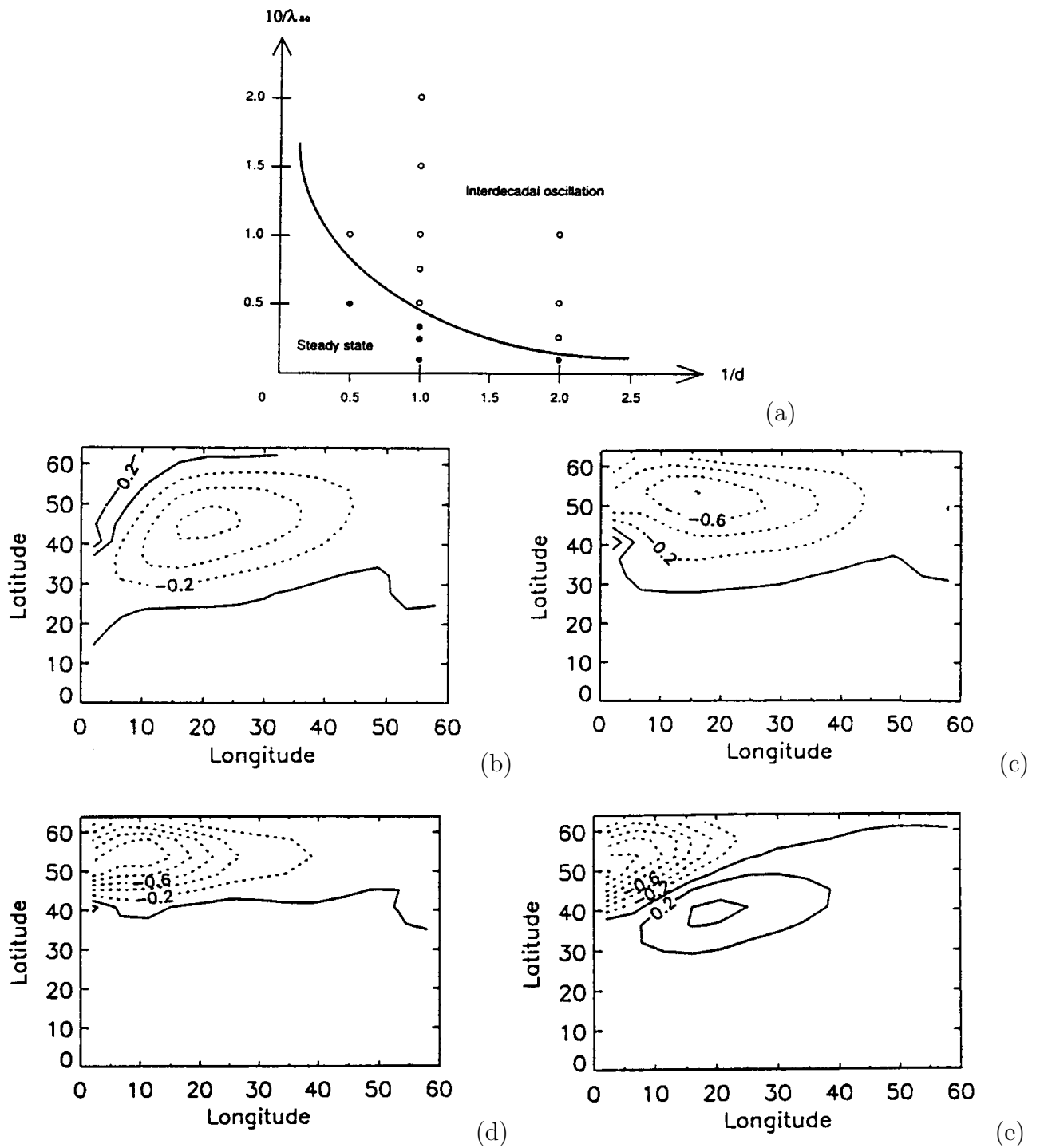


Figure 15. (a) Regime for a hybrid coupled model. The parameters d and λ_{0a} are the atmospheric EBM's thermal diffusivity and the proportionality constant for the air-sea heat flux, respectively. Solid circles in both diagrams indicate numerically computed steady states, open circles indicate periodic solutions (from Chen and Ghil [1996]). (b-e) Interdecadal oscillation in the hybrid coupled model. SST anomaly patterns shown at intervals of about 5.5 years to cover roughly half a period of the 44-year oscillation

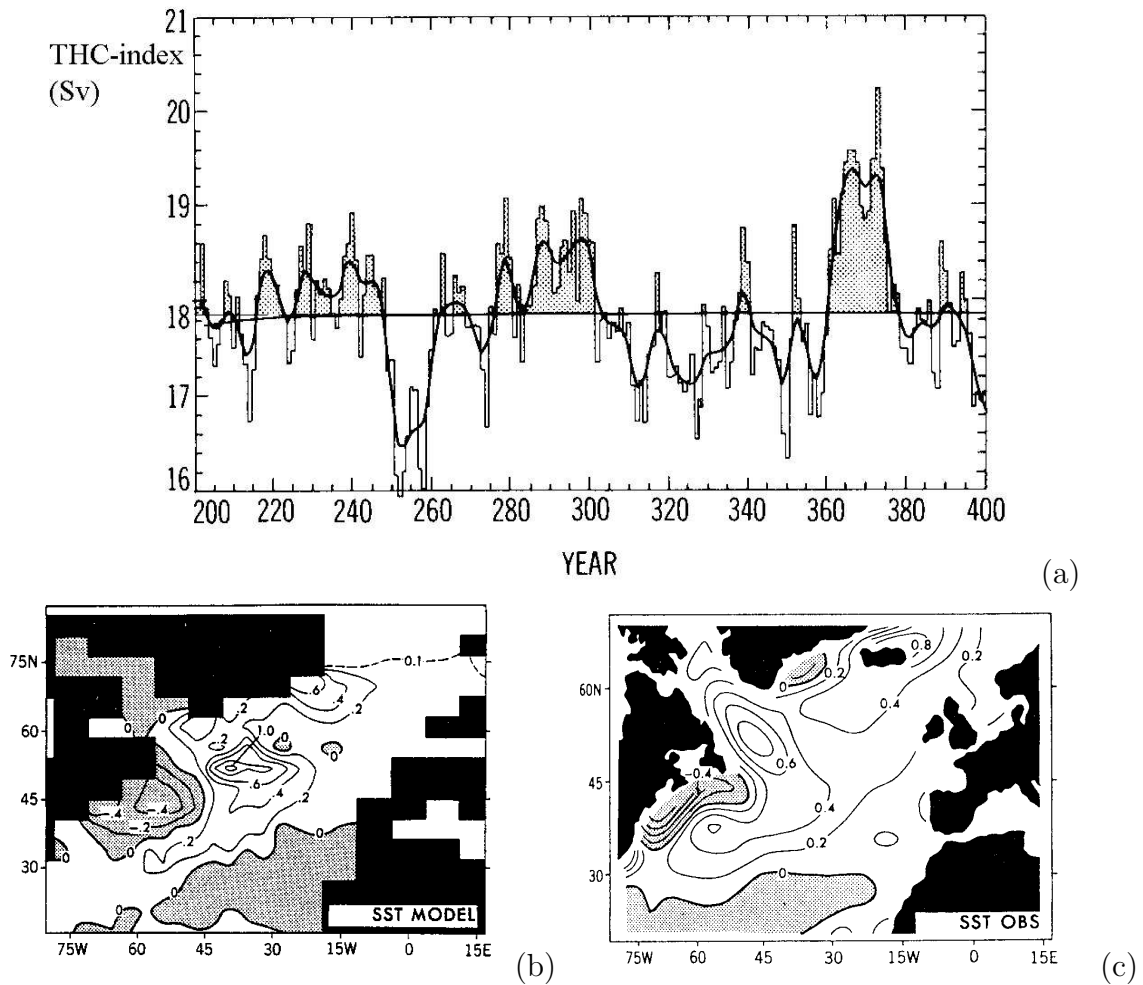


Figure 16. Interdecadal variability in the GFDL coupled ocean-atmosphere model (from Delworth et al. [1993]). (a) Time series of annual-mean THC index over 200 years of integration. (b) SST pattern obtained as the difference of four model-simulated decades of high-THC-index states and four model simulated low-THC-index states. (c) Pattern of interdecadal SST anomalies obtained as the difference between two 15-year long intervals: the relatively warm interval 1950-1964 and the relatively cold interval 1970-1984 (last panel from Kushnir [1994]).

TABLE 1. *Glossary of principal symbols*

Symbol	Definition	Section
A_H, A_V	lateral and vertical friction coefficient	Box 3
$A = H/L$	aspect ratio	Box 4
D	equilibrium layer depth	Box 3
$E = A_H/(2\Omega r_0^2)$	Ekman number	2.5
f, f_0	Coriolis parameter (at latitude θ_0)	2.3
\mathbf{f}, \mathbf{p}	vector field, parameter vector	1.4
F_0	freshwater forcing coefficient	Box 4
F_S, T_S	pattern of freshwater and temperature forcing	Box 4
$g, g' = g\Delta\rho/\rho_0$	gravitational acceleration, reduced gravity	Box 3
h	upper layer thickness	2.3
H	depth of the ocean basin	2.3
K_H, K_V	lateral and vertical diffusion coefficient	Box 4
L	basin length	2.3
$Pr = A_H/K_H$	Prandtl number	Box 4
Q	dimensionless wind-driven transport	2.5
r_0	radius of the Earth	2.3
R	bottom friction	Box 3
$Ra = (g\alpha_T\Delta TL^3)/(A_H K_H)$	Rayleigh number	Box 4
$Re = (\delta_I/\delta_M)^{1/3}$	Reynolds number	Box 3
$R_{HV}^M = A_V/A_H$	ratio of friction parameters	Box 4
$R_{HV}^T = K_V/K_H$	ratio of diffusivities	Box 4
S, T	salinity and temperature	3.2
\mathcal{R}^n	n -dimensional space of real numbers	1.4
(u, v, w)	velocity vector	Box 3
$(U, V) = (uh, vh)$	horizontal transport vector	Box 3
\mathbf{x}	state vector	1.4
α_T, α_S	thermal and saline expansion coefficient	Box 4
β	meridional variation of Coriolis parameter	Box 3
$\gamma = F_0 H/K_V$	dimensionless measure of freshwater flux strength	Box 4
Γ	trajectory in phase space	1.4
δ	regularization parameter	3.3
δ_I, δ_M	western boundary layer thicknesses	Box 3
$\Delta T, \Delta S$	characteristic temperature and salinity difference	Box 4
ϵ	Rossby number	Box 3
η_1, η_2, η_3	dimensionless parameters in box model	3.2
$\Phi(t)$	time periodic perturbation structure	2.3
Ψ	meridional overturning	3.2
λ	single parameter	1.4
$\bar{\lambda} = \alpha_T\Delta T/(\alpha_S\Delta S)$	buoyancy ratio	Box 4
μ_1, μ_2	dimensionless parameters	3.3
$\omega, S(\omega)$	frequency of oscillation, spectral power	1.1
Ω	angular frequency of the Earth	Box 3
$\rho_0, \Delta\rho$	background density, density difference	Box 3
$\sigma = \sigma_r + i\sigma_i$	complex growth factor, eigenvalue	1.4
τ^x, τ^y	zonal and meridional wind stress	Box 3

TABLE 2. *Glossary of acronyms*

Symbol	Definition	Section
0-D	Zero-dimensional	1.3
1-D	One-dimensional	1.3
2-D	Two-dimensional	1.3
3-D	Three-dimensional	1.3
AABW	Antarctic Bottom Water	3.1
ACC	Antarctic Circumpolar Current	3.4
COADS	Cooperative Ocean-Atmosphere Data Set	2.6
EBM	Energy balance model	3.4
EOF	Empirical orthogonal function	3.1
ENSO	El Niño/Southern Oscillation	1.1
GCM	General circulation model	1.3
GFDL	Geophysical Fluid Dynamics Laboratory	3.4
LSG	Large-Scale Geostrophic model	3.4
MOM	Modular Ocean Model	3.4
M-SSA	Multi-channel Singular-spectrum analysis	2.6
NADW	North Atlantic Deep Water	1.2
NPP	Northern sinking pole-to-pole flow	3.2
ODE	Ordinary differential equation	1.4
PDE	Partial differential equation	1.4
PGM	Planetary Geostrophic Model	3.4
POCM	Parallel Ocean Climate Model	2.6
POP	Parallel Ocean Program	3.4
QG	Quasi-geostrophic	2.3
SA	Salinity driven flow	3.2
SPP	Southern sinking pole-to-pole flow	3.2
SSA	Singular-spectrum analysis	2.3
SST	Sea-surface temperature	1.1
TH	Thermally driven flow	3.2
THC	Thermohaline circulation	3.1
WOCE	World Ocean Circulation Experiment	3.1

TABLE 3. *Oscillations in the oceans' wind-driven circulation: time scales and mechanisms.*

Time scale	Phenomena	Mechanism	Reference
Subannual	Rosby basin mode	Instability due to horizontal shear	<i>Pedlosky</i> [1987]
	Baroclinic mode	Instability due to vertical shear	<i>Pedlosky</i> [1987]
Interannual	Barotropic gyre mode	Symmetry breaking barotropic shear instability	<i>Jiang et al.</i> [1995], <i>Speich et al.</i> [1995], <i>Simonnet and Dijkstra</i> [2002]
Decadal	Baroclinic gyre mode	Symmetry breaking baroclinic shear instability	<i>Nauw and Dijkstra</i> [2001] <i>Ghil et al.</i> [2002b]

TABLE 4. *Oscillations in the oceans' thermohaline circulation (THC): time scales and mechanisms. (after Ghil [1994]).*

Time scale	Phenomena	Mechanism	Reference
Decadal	Local migration of surface anomalies due to surface cooling	Localized surface-density anomalies due to surface coupling	<i>Chen and Ghil</i> [1995]
	Advection of density anomalies at midlatitudes	Gyre advection	<i>Weaver et al.</i> [1991]
Interdecadal	Westward propagation of temperature anomalies	Generalized baroclinic instability	<i>Colin de Verdière and Huck</i> [1999], <i>Delworth et al.</i> [1993],
	Advection of density anomalies and convection changes	Combined gyre and overturning advection	<i>Delworth and Greatbatch</i> [2000], <i>TeRaa and Dijkstra</i> [2002]
Centennial	Loop-type, meridional circulation	Conveyor-belt advection of density anomalies	<i>Mikolajewicz and Maier-Reimer</i> [1990], <i>Winton and Sarachik</i> [1993]
Millennial	Flushes and superimposed decadal fluctuations	Bottom-water warming	<i>Chen and Ghil</i> [1995], <i>Weaver et al.</i> [1993]

Box 1: Intended audience and corresponding reading routes

The material covered by this review has attracted increasing interest from a broad audience. This audience includes, of course, oceanographers but also atmospheric and other geoscientists, climate change researchers, as well as fluid dynamicists and applied mathematicians. The purpose of the review is, therefore, to satisfy the curiosity of and provide a research tool to this broad audience, to the extent possible within the space allowed.

Obviously, some parts of the material will be more familiar to certain readers than to others. Much of Sections 1.2, 2.1, 2.2, and 3.1 can be skipped by all oceanographers, as well as by many of the other geoscientists. Likewise, Box 2, on elementary bifurcation theory, will be well known to all applied mathematicians and to many interested fluid dynamicists and geoscientists, but not to all.

The methods of bifurcation theory are applied in Section 2 to the wind-driven circulation and in Section 3 to the thermohaline circulation. These two sections are fairly self-contained. An outlook on the future of this approach in oceanographic and climate studies concludes the paper. Therefore, depending on the readers' interest and background, they can skip either Section 2 or 3 in proceeding from Section 1 to Section 4. The principal results of Section 2 appear in Table 3, at the end of that section, and those of Section 3 in the corresponding Table 4.

Box 2: Elementary bifurcations

The simplest, most robust and oft-encountered bifurcations occur when a single parameter, say λ , is varied. The type of bifurcation depends on how the eigenvalues σ of the Jacobian matrix \mathbf{J} in (5) cross the imaginary axis. Since \mathbf{J} has real coefficients, it is either a real eigenvalue or a complex conjugate pair of eigenvalues that crosses this axis.

A single zero eigenvalue

The first example is that of the *saddle-node bifurcation*, also called limit point or turning point. The simplest dynamical system in which this bifurcation occurs has

$$f(x, \lambda) = \lambda - x^2. \quad (\text{B-1})$$

Fixed points $\bar{x} = \pm\sqrt{\lambda}$ exist when $\lambda > 0$ and no solutions exist for $\lambda < 0$. The stability of these states is determined by the sign of the unique eigenvalue $\sigma = -2\bar{x}$ of the Jacobian matrix. Hence the solution $\bar{x} = \sqrt{\lambda}$ is stable, while the solution $\bar{x} = -\sqrt{\lambda}$ is unstable. The saddle-node bifurcation is characterized by a sudden appearance or disappearance of solutions in the parameter space. Well-known examples in atmospheric and climate dynamics include energy-balance models [Ghil, 1976; North *et al.*, 1983] and the Charney and DeVore [1979] model of bistability of blocked and zonal flows.

A second important example, a so-called *pitchfork bifurcation*, arises in the presence of mirror symmetry; such a symmetry can be written in general as $\mathbf{f}(-\mathbf{x}) = -\mathbf{f}(\mathbf{x})$. The simplest system in which this bifurcation occurs has

$$f(x, \lambda) = \lambda x - x^3. \quad (\text{B-2})$$

For $\lambda < 0$, there is only one steady solution (or fixed point) $\bar{x} = 0$, but for $\lambda > 0$, three fixed points exist: $\bar{x} = 0$ and $\bar{x} = \pm\sqrt{\lambda}$. Hence, the number of fixed points changes from one to three as λ crosses zero. Since $J = \lambda - 3\bar{x}^2$, $\sigma = \lambda$ for $\bar{x} = 0$ and hence $\bar{x} = 0$ is stable for $\lambda < 0$ but unstable for $\lambda > 0$. The two additional fixed points that exist for $\lambda > 0$ have $\sigma = -2\lambda$, so that these are both stable (Fig. B-1a). This bifurcation is actually called a supercritical pitchfork bifurcation, since the two mirror-symmetrical nonzero solutions exist for $\lambda > 0$. For the system $f(x, \lambda) = \lambda x + x^3$, three solutions coexist for negative λ and a subcritical pitchfork bifurcation occurs. The latter type arises, for example, in the Lorenz [1963a] system.

What happens when the mirror symmetry of $f(x, \lambda)$ in the bifurcation equation (B-2) is slightly perturbed: does the solution structure change and if so, can one determine *a priori* how? Slight perturbations from the symmetry can be represented as as

$$f(x, \lambda) = \epsilon + \lambda x - x^3 \tag{B-3}$$

for some (small) ϵ . When $\epsilon = 0$, a pitchfork bifurcation occurs at $(\bar{x} = 0, \lambda = 0)$, but for $\epsilon \neq 0$, the pitchfork bifurcation is no longer present because the reflection symmetry is broken: $f(-x, \lambda) \neq -f(x, \lambda)$. The bifurcation diagram for $\epsilon \neq 0$ is referred to as an imperfect pitchfork bifurcation. Such a diagram has a connected branch, which is present over the entire parameter range, and a disconnected branch, which exhibits a saddle-node bifurcation (see Fig. B-1b for $\epsilon > 0$).

A single complex conjugate pair of eigenvalues

In the saddle-node and pitchfork bifurcations, the number of fixed points changes as a parameter is varied. We now consider a bifurcation in which the character of the unique solution changes, from steady to oscillatory. The simplest example of this type of bifurcation, called *Hopf bifurcation*, is given by

$$\begin{aligned}\frac{dx}{dt} &= \lambda x - \omega y - x(x^2 + y^2), \\ \frac{dy}{dt} &= \lambda y + \omega x - y(x^2 + y^2).\end{aligned}\tag{B-4}$$

It can be easily checked that, at $\lambda = 0$, the Jacobian matrix \mathbf{J} associated with the trivial solution $\bar{x} = \bar{y} = 0$ has a complex conjugate pair of eigenvalues $\sigma = \pm i\omega$.

Transformation of (B-4) to polar coordinates $x = r \cos \theta$, $y = r \sin \theta$ yields the more transparent form

$$\begin{aligned}\frac{dr}{dt} &= \lambda r - r^3, \\ \frac{d\theta}{dt} &= \omega.\end{aligned}\tag{B-5}$$

Comparing (B-5) with (B-2), it can be seen that a pitchfork bifurcation occurs at $\lambda = 0$ in the (r, λ) plane. For $\lambda < 0$, only one stable fixed point, $\bar{r} = 0$, exists; it corresponds to a steady solution of the original equations. For $\lambda > 0$, however, the nontrivial stable fixed points given by $r = \pm\sqrt{\lambda}$ now represent a periodic solution of the original equations, with a period of $2\pi/\omega$. Hence, a transition from steady to periodic behavior occurs as λ crosses zero.

The emergence of the periodic orbit can be seen explicitly by computing trajectories of the equations (B-4) for a subcritical value of $\lambda = -0.1$ and a supercritical value of $\lambda = 0.1$. In the subcritical case (Fig. B-2a), the trajectory spirals in and finally ends up at the stable fixed point $(0, 0)$. In the supercritical case (Fig. B-2b), however, it spirals onto the periodic orbit with $\bar{r} = 1.0/\sqrt{10}$ that arises through the Hopf bifurcation.

A trajectory starting at $(0, 0.1)$ is also plotted as the dashed curve in Fig. B-2b and demonstrates that the origin has become an unstable fixed point; this trajectory spirals out to approach asymptotically the periodic orbit from within.

The stable periodic orbits that arise by a Hopf bifurcation are called *limit cycles*. They represent the nonlinear saturation of a linear oscillatory instability. Well known examples of Hopf bifurcations in atmospheric dynamics include baroclinic instability [Lorenz, 1963b; Pedlosky, 1987] and oscillatory topographic instability [Legras and Ghil, 1985; Ghil and Vautard, 1991].

Box 3: The 1.5-layer shallow-water model

Consider a rectangular ocean basin of dimensions $L \times 2L$ on a midlatitude β -plane with Coriolis parameter $f = f_0 + \beta_0 y$; x and y are east- and northward pointing Cartesian coordinates. An active layer of mean depth D with density ρ_0 is situated above a slightly heavier layer that has a density $\rho_0 + \Delta\rho$ and is supposed to be motionless. The interface between the two layers is conceptually identified with the permanent thermocline; it is able to deform and the reduced gravity g' that acts on the upper layer is given by $g' = g\Delta\rho/\rho_0$. Such a shallow-water model is commonly referred to as a *1.5-layer model*.

The flow is driven by a wind stress $\tau(x, y) = \tau_0(\tau^x, \tau^y)$ with amplitude τ_0 , assumed to be constant in time, and spatial pattern (τ^x, τ^y) . Lateral friction, with coefficient A_H , and bottom friction, with coefficient R , are the only dissipative mechanisms. The stratification, i.e., the vertical structure of the density and flow fields, as well as the description of subgrid-scale mixing processes are thus highly simplified.

The velocities in the east- and northward directions are denoted by $\mathbf{v} = (u, v)$ and $h = h(x, y, t)$ is the thickness of the upper layer, which takes the equilibrium value D in the absence of forcing. The upper-layer mass flux vector \mathbf{V} is given by $\mathbf{V} = (U, V) = (hu, hv)$ and the equations describing the flow are [Jiang *et al.*, 1995]

$$\begin{aligned} \frac{\partial U}{\partial t} + \nabla \cdot (\mathbf{v}U) - fV &= -g'h\frac{\partial h}{\partial x} + A_H\nabla^2 U - RU + \alpha_\tau \frac{\tau_0\tau^x}{\rho_0}, \\ \frac{\partial V}{\partial t} + \nabla \cdot (\mathbf{v}V) + fU &= -g'h\frac{\partial h}{\partial y} + A_H\nabla^2 V - RV + \alpha_\tau \frac{\tau_0\tau^y}{\rho_0}, \\ \frac{\partial h}{\partial t} &= -\frac{\partial U}{\partial x} - \frac{\partial V}{\partial y}. \end{aligned} \tag{B-6}$$

No-slip conditions are specified on the boundary and an idealized wind stress, given by

$$\tau^x(y) = -\cos\left(\frac{k\pi y}{2L}\right), \quad \tau^y = 0 \quad ; \quad 0 \leq y \leq 2L, \quad (\text{B-7})$$

forces the circulation within the basin. The double-gyre forcing ($k = 2$) is chosen as explained above, whereas single-gyre studies have used $k = 1$. The double-gyre forcing, as well as the boundary conditions, have mirror symmetry about the mid-axis of the basin, located at $y = L$.

To help understand the bifurcation behavior of the shallow-water model, Jiang *et al.* [1995] introduced a highly truncated QG model, with only two modes:

$$\begin{aligned} \frac{dA}{dt} - \mu AB + \nu A &= \eta_1 \\ \frac{dB}{dt} + \mu A^2 + \nu B &= \eta_2. \end{aligned} \quad (\text{B-8})$$

Here A and B are the symmetric and antisymmetric component of the flow, while μ and ν are positive constants, with μ proportional to the Rossby number and ν proportional to the characteristic width of the western boundary layer. The wind-stress forcing is represented by its antisymmetric and symmetric parts, η_1 and η_2 .

In fact, there are two distinct boundary-layer thicknesses, the Munk thickness $\delta_M = (A_H/\beta_0)^{1/3}$ and the inertial boundary layer thickness $\delta_I = (\bar{U}/\beta_0)^{1/2}$; here \bar{U} is a characteristic depth-averaged horizontal velocity. Two important nondimensional numbers that characterize the flow are the Rossby number $\epsilon = \bar{U}/(f_0L)$ and the Reynolds number $Re = (\delta_I/\delta_M)^3$.

Box 4 : The 2D-Boussinesq equations

The simplest 2-D model employs a Cartesian coordinate system, with meridional coordinate $0 \leq y \leq L$ and vertical coordinate $0 \leq z \leq H$, where H and L are the depth of the fluid and the meridional extent of the basin, respectively. For 2-D flow fields, which do not depend on the zonal coordinate, the equations governing the meridional velocity v , vertical velocity w , pressure p , density ρ , temperature T , and salinity S are

$$\begin{aligned} \frac{\partial u}{\partial t} + v \frac{\partial u}{\partial y} + w \frac{\partial u}{\partial z} + \frac{1}{\rho_0} \frac{\partial p}{\partial y} &= A_H \frac{\partial^2 v}{\partial y^2} + A_V \frac{\partial^2 v}{\partial z^2}, \\ \frac{\partial w}{\partial t} + v \frac{\partial w}{\partial y} + w \frac{\partial w}{\partial z} + \frac{1}{\rho_0} \frac{\partial p}{\partial z} + \frac{\rho}{\rho_0} g &= A_H \frac{\partial^2 w}{\partial y^2} + A_V \frac{\partial^2 w}{\partial z^2}, \\ 0 &= \frac{\partial v}{\partial y} + \frac{\partial w}{\partial z}, \\ \frac{\partial T}{\partial t} + v \frac{\partial T}{\partial y} + w \frac{\partial T}{\partial z} &= K_H \frac{\partial^2 T}{\partial y^2} + K_V \frac{\partial^2 T}{\partial z^2}, \\ \frac{\partial S}{\partial t} + v \frac{\partial S}{\partial y} + w \frac{\partial S}{\partial z} &= K_H \frac{\partial^2 S}{\partial y^2} + K_V \frac{\partial^2 S}{\partial z^2}. \end{aligned} \tag{B-9}$$

The simplest equation of state is a linear dependence of density on temperature and salinity, i.e., $\rho = \rho_0[1 - \alpha_T(T - T_0) + \alpha_S(S - S_0)]$, while the Boussinesq approximation for thermosolutal convection allows the density to vary only in the buoyancy term of (B-9). Here $A_{H/V}$ and $K_{H/V}$ are the diffusivities of momentum and of heat and salt, respectively. Since we are interested in a thin layer, $H/L \ll 1$, we consider eddy diffusivities that may take very different values in the vertical and horizontal directions [Quon and Ghil, 1995]. The rectangular flow domain is typically assumed to be symmetric about the equator.

The boundary conditions for temperature and salinity at the ocean surface $z = H$ become, in the limit of restoring temperature conditions and prescribed freshwater flux,

$$T(y, H) = T_S(y)\Delta T,$$

$$K_V \frac{\partial S}{\partial z}(y, H) = F_0 F_S(y), \tag{B-10}$$

where both T_S and F_S are prescribed dimensionless functions and ΔT is a typical meridional temperature difference. The freshwater flux has again been converted into an equivalent salt flux [Huang, 1993]. Salinity and heat fluxes are assumed to be zero at the bottom and lateral boundaries and free-slip conditions are applied at all boundaries.

When these equations are nondimensionalized, a number of parameters appear that depend on the type of scaling. For example, scales L_* , K_H/L_* , $\rho_0 K_H A_H/H^2$, ΔT and ΔS for length, velocity, pressure, temperature and salinity can be used, with ΔS being a characteristic meridional salinity difference. In this case, the Prandtl number Pr , the thermal Rayleigh number Ra , the buoyancy ratio $\bar{\lambda}$, the aspect ratio A , the salt flux strength γ , the ratios of vertical and horizontal diffusivities for momentum R_{HV}^M and for heat and salt R_{HV}^T appear. These nondimensional parameters are defined as

$$Pr = \frac{A_H}{K_H} \quad , \quad Ra = \frac{g\alpha_T\Delta TL_*^3}{A_H K_H} \quad , \quad A = \frac{H}{L_*} \quad , \quad \gamma = \frac{F_0 H}{K_V}$$

$$R_{HV}^M = \frac{A_V}{A_H} \quad , \quad R_{HV}^T = \frac{K_V}{K_H} \quad , \quad \bar{\lambda} = \frac{\alpha_S \Delta S}{\alpha_T \Delta T}.$$

The system of dimensionless equations thus contains seven parameters. However, if the salinity is rescaled with $\bar{\lambda}$, only six of the original seven parameters remain. Usually, the product $\gamma\bar{\lambda}$ is taken as the parameter that measures the strength of the freshwater flux. The scale invariance of physical laws permits one to determine rigorously the number of independent parameters in a fluid-dynamical problem. This result is often called Buckingham's Π -theorem [Barenblatt, 1987; Ghil *et al.*, 2002b] and its application to the 2-D THC does yield the number six above.

Figure B-1. (a) Bifurcation diagram of the pitchfork bifurcation in the system $f(x, \lambda) = \lambda x - x^3$. Solid lines indicate stable solutions, and dashed lines unstable ones; the bifurcation points are marked by solid circles and solid squares. (b) perturbed pitchfork bifurcation diagrams for the system $f(x, \lambda) = \epsilon + \lambda x - x^3$ for $\epsilon = 0.1$.

Figure B-2. Trajectories of the reduced equations (B-4) for the Hopf bifurcation: (a) before the bifurcation at $\lambda = 0$ ($\lambda = -0.1$); and (b) after the bifurcation ($\lambda = 0.1$). The secondary parameter value is $\omega = 1.0$ and both panels show a trajectory that starts at the point $(0, 2)$; in (b) an additional trajectory starting at $(0, 0.1)$ is shown as the dashed curve. Arrows indicate the tangent at that point, in the direction of evolution along the given curve.

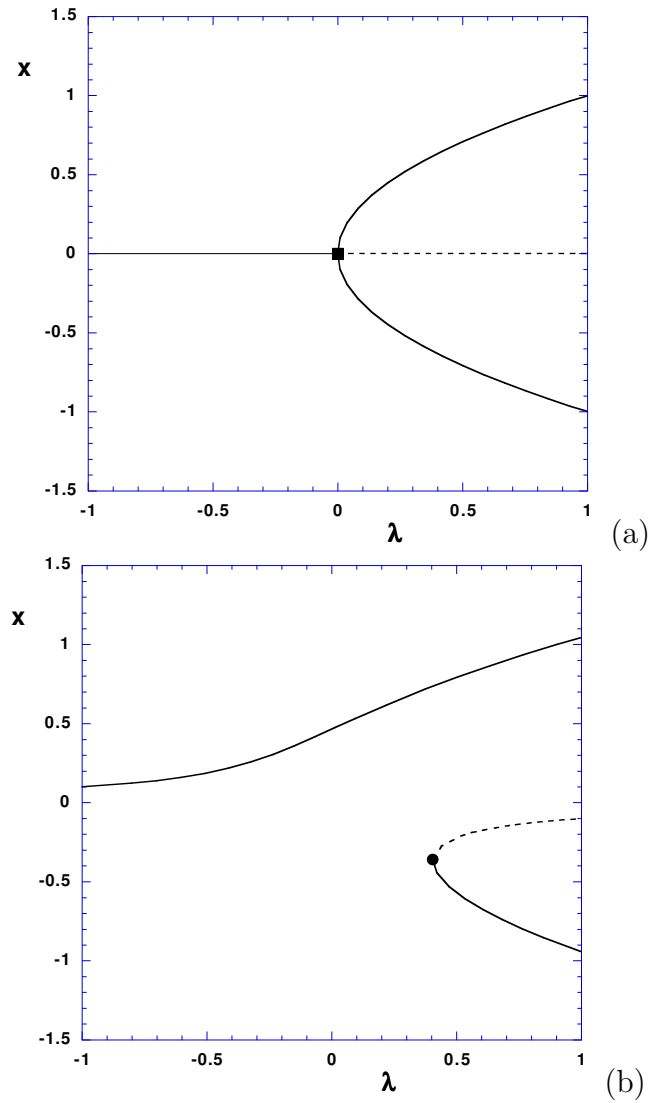


Figure B-1. (a) Bifurcation diagram of the pitchfork bifurcation in the system $f(x, \lambda) = \lambda x - x^3$. Solid lines indicate stable solutions, and dashed lines unstable ones; the bifurcation points are marked by solid circles and solid squares. (b) perturbed pitchfork bifurcation diagrams for the system $f(x, \lambda) = \epsilon + \lambda x - x^3$ for $\epsilon = 0.1$.

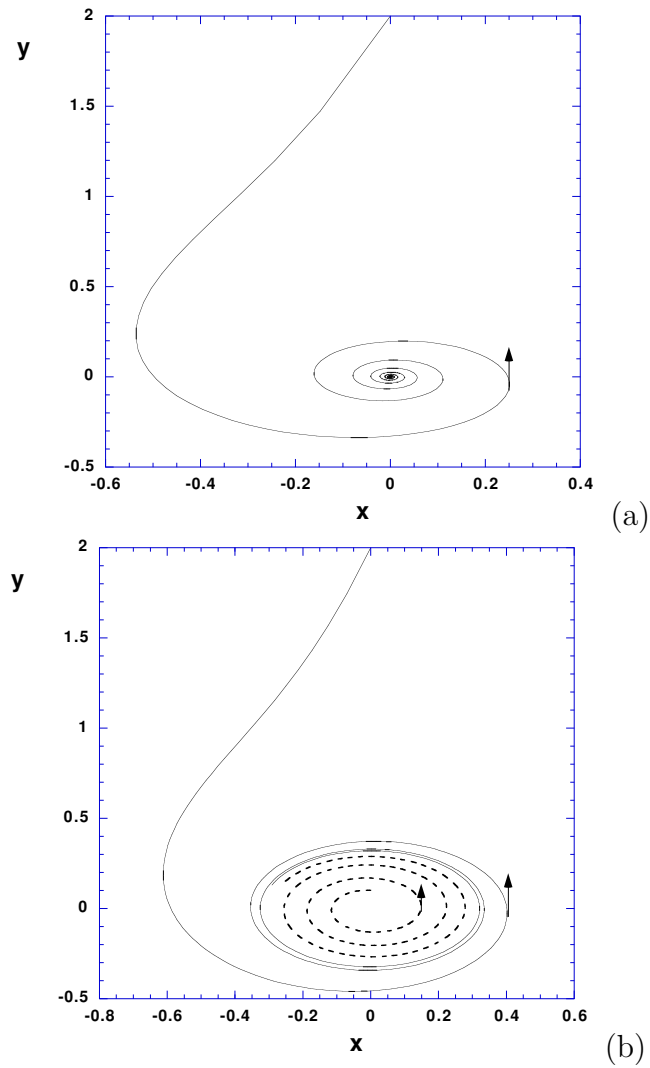


Figure B-2. Trajectories of the reduced equations (B-4) for the Hopf bifurcation: (a) before the bifurcation at $\lambda = 0$ ($\lambda = -0.1$); and (b) after the bifurcation ($\lambda = 0.1$). The secondary parameter value is $\omega = 1.0$ and both panels show a trajectory that starts at the point $(0, 2)$; in (b) an additional trajectory starting at $(0, 0.1)$ is shown as the dashed curve. Arrows indicate the tangent at that point, in the direction of evolution along the given curve.